Institut für Strömungsmechanik
und Elektronisches Rechnen im Bauwesen
der Leibniz Universität Hannover

Bericht Nr. 74/2008

Gesa Ziefle

Modeling aspects of coupled hydraulic–mechanical processes in clay material

ISSN 0177 — 9028

Institut für Strömungsmechanik
und Elektronisches Rechnen im Bauwesen
Leibniz Universität Hannover
Appelstraße 9A, D – 30167 Hannover

Tel.: +49 – 511 – 762-3568
Fax.: +49 – 511 – 762-3777
URL: http://www.hydromech.uni-hannover.de

Von der Fakultät für Bauingenieurwesen und Geodäsie der Leibniz Universität Hannover zur Erlangung des Grades Doktor – Ingenieurin genehmigte Dissertation.

Referent:	Prof. Dr.-Ing. Werner Zielke
Korreferenten:	Prof. Dr. rer. nat. Gerhard Starke
	Prof. Dr.-Ing. Martin Achmus

Tag der Promotion: 25. Februar 2008

Abstract

The presented thesis focuses on coupled hydraulic-mechanical processes in clay materials. In the framework of high–level radioactive waste disposal clay materials are of special interest in the near as well as in the far field. On the one side they are utilized e.g. as a part of engineered barrier systems composed of bentonite–sand–mixtures. On the other side, claystone is discussed to be a potential host rock for final repositories.

The work at hand uses the existing finite element program RockFlow to investigate possible migration processes in clay materials. That code contains classical hydraulic-mechanical couplings like the incorporation of stress-induced strains in the mass balance of the fluid as well as the application of Terzaghi' s effective stresses and the saturation dependent parameters in the non linear material formulation. Based on this, extensions of the existing code are presented in this work. They focus on the development of concepts and algorithms concerning clay related processes.

Clay materials imply effects like swelling and shrinkage. In addition to classical mechanical deformations the swelling and shrinkage affect the porosity and furthermore the permeability of the material. As the clay material usually comprises very low porosities, already a reduction of the pore space due to geometric linear deformations lead to non linear material behavior if the solid grains are assumed to be incompressible. Consequently, a non linear elastic compressibility model that pictures the behavior due to compaction converging to the compression point is presented and implemented. The incorporation of initial stresses as well as initially reduced porosities is facilitated in the model due to a differentiation between initial and stress free porosity. Furthermore, clay materials imply pressure sensitive, strain–hardening plastic behavior. An elasto–plastic material model of the Cam–Clay type is incorporated in the finite element formulation. Finally, the applicability of the code is presented due to various examples and the impact of the presented mechanical extensions on the hydraulic process is investigated.

Keywords: finite elements, coupled hydraulic–mechanical processes, clay materials, elasto–plasticity of the Cam–Clay type, non linear elastic compressibility, strain dependent porosity, strain dependent permeability, swelling and shrinkage

Zusammenfassung

Diese vorliegende Schrift beschäftigt sich mit hydraulisch–mechanisch gekoppelten Prozessen in Tonmaterialien. Im Bereich der Endlagerung hochradioaktiver Abfälle sind Tonmaterialien sowohl im Nah- als auch im Fernbereich von besonderer Bedeutung. Im Nahbereich können sie zur Optimierung des technischen Barrieresystems verwendet werden, das z.B. aus Bentonit–Sand–Gemischen bestehen kann. Im Fernfeld wird Tonstein als potentielles Wirtsgestein zur Lagerung in geologisch großen Tiefen diskutiert.

Zur Untersuchung von Migrationsprozessen in Tonmaterialien wird in dieser Arbeit das Programm RockFlow benutzt, das auf der Methode der finiten Elemente basiert. In diesem Programm sind die klassischen hydraulisch–mechanischen Kopplungsmechanismen wie die Einbeziehung der Dehnungen in die Massenbilanz, Terzaghi' s effektive Spannungen sowie sättigungsabhängige Materialparameter berücksichtigt. Darauf basierend werden Weiterentwicklungen des Programms RockFlow hinsichtlich von Konzepten und Algorithmen zur Behandlung tonspezifischer Prozesse vorgestellt.

Tonmaterialien beinhalten Effekte wie Quellen und Schrumpfen. In Kombination mit den klassischen mechanischen Deformationen beeinflussen diese die Porositäten und weiterhin die Permeabilitäten des Materials. Zusätzlich besitzen Tonmaterialien in der Regel sehr geringe Porositäten. Folglich kann schon eine geringfügige Komprimierung des Materials, die üblicherweise der geometrisch linearen Theorie zugeordnet werden kann, zu nichtlinearem Materialverhalten führen, wenn die einzelnen Körner als inkompressibel angenommen werden. Ein nichtlineares elastisches Materialmodell, das das Kompaktionsverhalten von Material bis zum Kompressionspunkt abbildet, wird in dieser Arbeit vorgestellt. Mit Hilfe der Unterscheidung zwischen anfänglichen und spannungsfreien Porositäten ermöglicht dieses Modell die Berücksichtigung von Anfangszuständen. Ein weiterer wichtiger Aspekt der Modellierung ist elastoplastisches Materialverhalten. Tone zeigen Verfestigungs– sowie Entfestigungsverhalten und reagieren auch auf rein hydrostatische Belastungen mit plastischen Dehnungen. Diese Eigenschaften werden mit Hilfe eines plastischen Modells vom Typ der Cam–Clay Modelle abgebildet. Schließlich wird die Anwendbarkeit des entwickelten Programms anhand verschiedener Beispiele gezeigt und die Einflüsse der genannten mechanischen Prozesse auf den hydraulischen Prozess untersucht.

Schlagworte: Finite Elemente, gekoppelte hydraulisch–mechanische Prozesse, tonhaltige Materialien, Elasto–plastizität im Rahmen der Cam–Clay Modelle, nichtlineare elastische Kompressibilität, dehnungsabhängige Porosität, dehnungsabhängige Permeabilität, Quellen und Schrumpfen

Vorwort

Die vorliegende Dissertation ist im Rahmen meiner Tätigkeit am Institut für Strömungsmechanik und Elektronisches Rechnen im Bauwesen (ISEB) an der Leibniz Universität Hannover entstanden. Hier war ich in den Jahren 2002 bis 2008 als wissenschaftliche Mitarbeiterin tätig. Weiterhin wurde ich von der Deutschen Forschungsgemeinschaft (DFG) im Rahmen eines Stipendiums im Graduiertenkolleg 615 „Interaktion von Modellbildung, Numerik und Software–Konzepten für technisch–wissenschaftliche Problemstellungen“ unterstützt.

Bedanken möchte ich mich zunächst bei Herrn Prof. W. Zielke für die Übernahme des Referats und die dauerhafte Unterstützung, die dazu beigetragen hat, dass ich das Ziel meiner Arbeit nicht aus den Augen verloren habe. Auch den Korreferenten Herrn Prof. G. Starke und Herrn Prof. M. Achmus sei für die Hinterfragung meiner Arbeit insbesondere bezüglich des mathematischen Hintergrundes und des Anwendungsbezuges herzlich gedankt. Weiterhin möchte ich auch Herrn Prof. U. Nackenhorst meinen Dank aussprechen, der mit großem Engagement den Vorsitz der Prüfungskommission übernommen hat. Zum Gelingen meiner Arbeit haben zudem Martin Kohlmeier, Jobst Maßmann, Matthias Ziefle und Astrid Krüger beigetragen, bei denen ich mich für die vielen Anregungen und die kritische Durchsicht meiner Schrift bedanken möchte.

Wichtige Grundlage meiner Arbeit war das bereits existierende finite Element Programm RockFlow, das am ISEB entwickelt wird und auf dessen Grundlage ich meine Erweiterungen durchführen konnte. Großer Dank gilt daher den ehemaligen sowie aktuellen Mitarbeitern der Grundwassergruppe. Hier sind insbesondere meine Kollegen Martin Kohlmeier und Jobst Maßmann zu nennen, mit denen mich eine jahrelange fröhliche Zusammenarbeit mit vielen bereichernden Diskussionen verbindet. Aber auch den zeitweiligen Kollegen René Kaiser, Sylvia Moenickes, Abderrahmane Habbar, Olaf Kolditz und Meike Wulkau sowie meinen Hiwis Michael Plotkowiak und Elisabeth Edom bin ich für ihre Anregungen und ihr Engagement sehr dankbar.

Weiterhin hat das gute Arbeitsklima am ISEB sehr zum Gelingen meiner Arbeit beigetragen. Daher möchte ich mich bei allen Beteiligten für die Schaffung dieser schönen Rahmenbedingungen mit vielen fachlichen aber auch immer wieder persönlichen Kontakten bedanken. Insbesondere möchte ich an dieser Stelle Frau Seifert für ihr persönliches Interesse sowie die engagierte Bereitschaft danken, mit der sie jegliche Probleme sofort und mit großem Einsatz zu lösen bereit war. Weiterhin bin ich ihr sowie den Kollegen Rainer Ratke, Ruth Grundt und Mark Markofsky für die vielen - nicht nur fachlichen - Gespräche dankbar. Die ersten Jahre am ISEB habe ich mit Jens Wiemann ein Zimmer geteilt - auch Dir Jens möchte ich für die Schaffung eines sehr angenehmen Arbeitsklimas sowie die gute Kameradschaft danken.

Neben dem kollegialen Rahmen am Institut hat mir die Einbindung in das GRK 615 vielfältige Kontakte beschert. Insbesondere die Interdisziplinarität hat hier zu immer neuen, spannenden Diskussionen und Erkenntnissen geführt, so dass ich mich auch hier bei allen Beteiligten für die vielfältigen Anregungen bedanken möchte.

Im Rahmen zahlreicher Projekte sowie den damit verbundenen Treffen und Konferenzen hat eine stete Zusammenarbeit des ISEB mit der Bundesanstalt für Geowissenschaften und Rohstoffe (BGR) stattgefunden. Für die damit verbundenen Anregungen, Diskussionen und den Ideenaustausch möchte ich mich in erster Linie bei den Kollegen Hua Shao, Thomas Nowak, Jürgen Hesser, Herbert Kunz und Dieter Stührenberg herzlich bedanken. Die Gewissheit, Programmentwicklungen nicht nur des reinen Forschens Willen durchzuführen, sondern auch konkrete Anwendungen zu sehen hat mich immer wieder neu motiviert.

Aber zum Glück gibt es neben den beruflichen Bekanntschaften auch einen - mal wieder interdisziplinären - privaten Freundeskreis. Ihr alle habt auf vielfältige Weise dazu beigetragen, dass mein Leben nicht nur aus numerischen oder physikalischen Problemen und deren Lösung besteht. Vielen Dank dafür.

Besonderer Dank gebührt auch meinen Eltern und Schwiegereltern, die mich immer unterstützt haben. Vor allem in den letzten Jahren hat ihr großes Engagement bei der Kinder- und Hundebetreuung wesentlich dazu beigetragen, dass ich sowohl die Zeit als auch den Kopf hatte, um mich mit meiner Arbeit beschäftigen zu können. In diesem Zusammenhang möchte ich mich auch bei Dir, Arne, für die Anregung zu zahlreichen ablenkenden Kurzurlauben und die damit verbundene gemeinsam verbrachte Zeit bedanken.

In ganz besonderem Maße sind natürlich auch mein Mann Matthias und mein Sohn Lasse an der Entstehung der vorliegenden Dissertation beteiligt. Sie teilen ein ereignisreiches, spannendes und fröhliches Leben mit mir, dass mir immer wieder den nötigen Abstand zu meiner Arbeit verschafft hat. Dennoch haben sie auch immer wieder mit großem Verständnis darauf reagiert, wenn ich zu arbeiten hatte oder in der Uni Termine anstanden. Ihr beiden, dafür bin ich euch sehr dankbar.

Contents

1 Introduction **1**
- 1.1 Motivation 1
- 1.2 Approach 1
- 1.3 Numerical background 4
- 1.4 Outline 4

2 Theoretical background **7**
- 2.1 Theory of porous media 7
  - 2.1.1 Theory of mixture 8
  - 2.1.2 Concept of volume fractions 8
- 2.2 Kinematical relations 10
  - 2.2.1 Initial and current configuration 10
  - 2.2.2 Deformation gradient 11
  - 2.2.3 Strain tensors 12
  - 2.2.4 Linearization of the strain tensor 13
  - 2.2.5 Stress tensors 13
- 2.3 Balance relations of the mixture 14
  - 2.3.1 Conservation of mass 15
  - 2.3.2 Conservation of linear momentum 16
  - 2.3.3 Conservation of angular momentum 17
  - 2.3.4 Conservation of energy 18
  - 2.3.5 Entropy inequality 18
- 2.4 Constitutive equations 19
  - 2.4.1 Linear elastic, isotropic material model 19
  - 2.4.2 Effective stresses 20
  - 2.4.3 Linear swelling model 21

2.4.4 Strain dependent porosity 22
2.4.5 *Darcy´s law* 22
2.4.6 Definition of a relative permeability 23
2.4.7 *Richards‘ approximation* 24
2.5 The mathematical point of view 25
2.5.1 Partial differential equations 25
2.5.2 Mathematical formulation of the classical boundary value problem (BVP) 26
2.5.3 The weak form 27
2.5.4 Investigating the weak form 28

3 A non linear elastic compressibility model 31
3.1 General derivation of constitutive material models 31
3.2 Linear elastic, compressible material 33
3.3 Non linear elastic, compressible material 33
3.3.1 Physical background and relating definitions 34
3.3.2 Theoretical background of the non linear compressibility model for the geometric linear case 36
3.3.3 Requirements on the strain energy function 39
3.3.4 Review of further physical requirements on the material matrix 40
3.3.5 Validation due to the comparison with experimental data found in the literature 42
3.3.6 Final remarks 45

4 Elasto-plasticity with respect to clay modeling 49
4.1 Historical review of plastic material modeling 49
4.2 Variable yield surfaces 53
4.2.1 Hardening and softening 53
4.2.2 Dependency of the yield criterion on the pore volume 54
4.2.3 Dependency of the yield function on the saturation 55
4.3 Theoretical background of elasto-plastic material modeling 56
4.3.1 Return mapping 56
4.3.2 Loading and unloading conditions 57
4.4 A plastic model of the Cam-Clay type 58
4.4.1 Basic equations of the proposed modified Cam-Clay model 58
4.4.2 Algorithmic formulation of the Cam-Clay model 61
4.4.3 Algorithmic consistent elasto-plastic tangent 65

5 Numerical Solution **67**

5.1 The Finite Element Method (FEM) 67

5.1.1 Idea and concept 67

5.1.2 Spatial discretization 68

5.1.3 Temporal discretization 68

5.1.4 Boundary Conditions 70

5.2 Weak formulation of the coupled problem 70

5.2.1 Mechanical subproblem 70

5.2.2 Hydraulic subproblem 71

5.3 Usage of the FEM for the coupled problem 72

5.3.1 Mechanical subproblem 73

5.3.2 Hydraulic subproblem 74

5.3.3 Temporal discretization 75

5.3.4 Formulation of a coupled hydraulic–mechanical problem for the numerical solution by the FEM 75

5.4 Solver 76

5.4.1 Newton-Raphson iteration 76

5.4.2 Picard iteration 77

5.5 The finite element code RockFlow 78

6 Applications **81**

6.1 Step-wise compression test 81

6.1.1 Model setup 81

6.1.2 Results 83

6.2 Step-wise compression of a preloaded sample 88

6.2.1 Model setup 88

6.2.2 Results 88

6.3 Foundation problem 90

6.3.1 Model setup 90

6.3.2 Results 92

6.4 Hardening and softening behavior found in a triaxial test 94

6.4.1 Model setup 94

6.4.2 Results 95

6.5 Deformation induced strain dependent permeability 97

6.5.1 Model setup 97
6.5.2 Results 98
6.6 Strain dependent permeability due to swelling and shrinkage 102
6.6.1 Model setup 102
6.6.2 Results 103
6.7 Migration test in a bentonite-sand-mixture („TDR experiment“) 107
6.7.1 Experimental design 107
6.7.2 Model setup 107
6.7.3 Material properties 109
6.7.4 Investigating the impact of various processes 112
6.7.5 Simulation of the TDR-test 113
6.7.6 Additional effect due to higher permeabilities in the upper part 117
6.7.7 Discussion of the results 119

7 Conclusion 121

A Basic notations and definitions 125

A.1 Voigt Notation 125
A.2 Definition of the fourth order identity tensor **I** 125
A.3 Definition of the second order identity tensor **1** 126
A.4 Euclidic norm 126
A.5 Neumann number 126
A.6 Definition of the p-q-plane in the principal stress space 127
A.7 The Euclidean space 127
A.8 The Lebesgue integral 128

Bibliography 129

Chapter 1

Introduction

1.1 Motivation

In the last years political as well as phenomenological publications illustrate the public and the scientific interest on storage techniques for high radioactive waste. This kind of waste is planned to be stored in high geological depths. In this framework a lot of research has been carried out over the last decades to simulate the effects in salt or in granite. During the last years, claystone has become more and more interesting as a potential host rock. It provides a low permeability, which is one of the most important properties of the potential host rock for a final repository.

In addition to the natural geological barrier proposed by the disposal in high depths, a so-called engineered barrier system (EBS) is situated in the near-field of the radioactive waste. The EBS may itself comprise a variety of sub-systems or components, such as the waste form, canister, buffer, backfill, seals and plugs. There exist various approaches for such a system, but many of them include the usage of a clay material like bentonite, often mixed with sand. This kind of material assures the general requirements on materials for backfilling: lower hydraulic conductivity than the surrounding rock, exertion of a swelling pressure that prevents rock fall, capability for placement even under the condition of significant water inflow and a rational placement (please refer to (Pusch & Yong, 2006)).

The related physical problems in the near- as well as in the far-field of the repository are characterized by the appearance of manifold interacting processes namely mechanical, hydraulic, thermal, chemical and biological ones which have a varying impact on the problem (please refer to (Kolditz, 1996), (Kolditz, 2002) or (Stephansson, Jing, & Tsang, 1996) amongst others).

1.2 Approach

The development of a mathematical model representing the physical problem in a comprehensive way requires the consideration of various aspects:

- type of material
- scale of time
- scale of space
- relevant processes
- interaction of the processes
- physical model approach
- publicity of the material properties
- numerical solvability
- evaluation of the results with respect to the problem description

Simulating the proposed problems the physical model should imply material parameters which are available in most of the cases. Within this context it has to be kept in mind, that geotechnical applications often include non-homogeneous materials, which have to be homogenized and incorporate varying material properties. The available properties are derived from field as well as laboratory tests and are often not very precise. Additionally, the physical model should be concise and mathematically solvable with reasonable amount. As the computational costs increase rapidly with the number of processes and the degree of coupling, the model should be restricted to the most important aspects of the specific problem. Within this work, the focus is put on hydraulic-mechanical problems.

Figure 1.1 gives an overview of the hydraulic as well as the mechanical processes, which have to be kept in mind to simulate the proposed kind of problems.

Plasticity & creep Clay materials behave in a visco-elasto-plastic manner. As the long term behavior is of special interest in the proposed field of applications, the influence of creep is neglected. Plastic effects might have a significant influence on the mechanical as well as on the hydraulic subproblem. Consequently, they have to be considered in various applications and are one topic of the work at hand.

Fracturing Especially the host rock in the far-field of a repository but also the engineered barrier system in the near-field might contain different kinds of fractures. Depending on the scale and physical treatment of fracturing, these effects might incorporate a lot of effort to be solved numerically. Combined with uncertainties due to the lack of in-situ measurements, fracturing is not part of the presented investigations in this work.

Non linearieties Nevertheless, various non linearities have to be handled. Especially the non linear elastic compression behavior will be in focus in the following sections.

Dilatancy & Strain-hardening/Strain-softening Additionally, like most of the soils, the clay provides dilatant as well as hardening and softening behavior, which is incorporated in the model description.

Swelling/Shrinkage & H Anisotropy & M Anisotropy Besides that, special properties of the clay material like swelling, shrinkage and hydraulic and mechanical anisotropy are included in the code.

Advection & Diffusion & Dispersion & Capillarity & Two-phase flow Concerning the hydraulic effects, transport processes like advection, diffusion and dispersion and as a consequence of the partial saturation two-phase flow and capillary effects have to be considered.

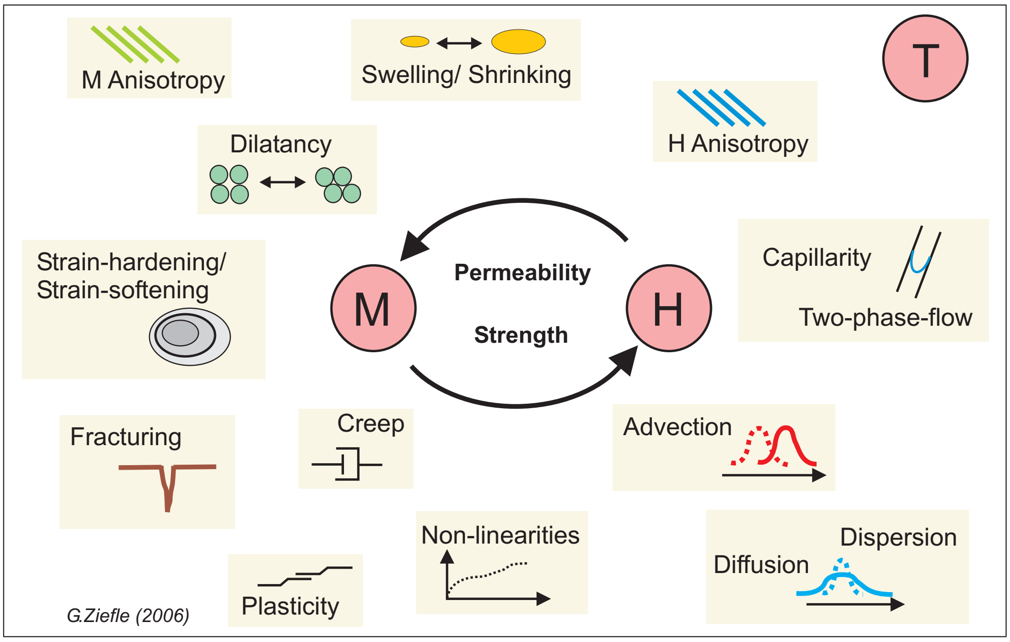

Figure 1.1: Hydraulic and mechanical processes in clay materials.

Summarizing this, the work at hand deals with the simulation of coupled hydraulic-mechanical processes in clay materials. It focuses on interacting processes like the impact of mechanical deformations as well as swelling and shrinkage on the porosity of the host rock. Additional incorporation of the relationship between porosity and permeability leads to a strain dependent permeability and indicates a direct influence on the hydraulic process. This relationship might also be treated in an anisotropic way. As the proposed materials provide low initial porosities this work additionally focuses on the impact of non linear elastic compression behavior for geometric linear problems. Furthermore, a plasticity model of the Cam-Clay type is introduced, incorporating effects like hardening, softening and pressure sensitivity. This kind of plastic model pictures typical behavior of clay materials and is based on the usage of only few material parameters which can be directly obtained from conventional laboratory experiments.

The development of the finite element code RockFlow is part of the research at the Institute of Fluid Mechanics since the 80th. Historically it was used for the simulation of hydraulic processes in fractured media, multi-phase flow and transport processes. In the last years it has been extended to a coupled hydraulic-mechanical and thermal program, which is described in detail in (Kohlmeier, 2006). The coupling of the participating hydraulic as well as mechanical processes takes place in the incorporation of stress-induced strains in the mass balance of the fluid as well as in the application of Terzaghis effective stresses. Additionally, non linear relations of capillary pressures and saturations as well as relative permeability and saturations are used.

Box 1.1: RockFlow: State of the art

1.3 Numerical background

The proposed types of clay material can be simplified by the theory of porous media. Founding on a kinematic description, balance equations as well as constitutive laws are applied to derive a mathematical description of the physical problem. Special attention should be turned on the physical and mathematical impact of the manifold interacting processes. As the finite element method turned out to be very robust and flexible concerning the proposed kind of problems, it is used to simulate the physical processes in a numerical way.

The available commercial simulation software (like ABAQUS, ANSYS amongst others) often focus on selected single processes with a restricted set of preassigned couplings. For example the incorporation of effects due to unsaturated media is often missing. Concerning the investigation of low permeable clay materials in the framework of nuclear waste disposal, various very specific effects and interactions have to be incorporated. Consequently, it is very advantageous to work with a code, which can be adopted to the special kind of problem at every time. The aspects presented in this work are implemented and investigated with the finite element code RockFlow, which is shortly introduced in box 1.1.

1.4 Outline

The investigation of the coupled hydraulic-mechanical processes starts with the examination of the physical model, which is expressed in a mathematical way and solved numerically. Within this work the physical problem is presented in a more general way before it is simplified to the specific hydraulic-mechanical problem. This procedure is chosen to provide a concise presentation for engineers as well as mathematicians.

Precisely, the work at hand starts with the presentation of the theoretical background. As the compressibility model as well as the elasto-plastic model are in the focus of the investigations presented here, these two topics are extended from the purely theoretical chapter. They are treated in a more detailed way in the following chapters. After that, the numerical approach is introduced and some applications are presented before the work is summarized. This procedure ends up in the following chapters:

Chapter 1 - Introduction

Chapter 2 - Theoretical background Within this chapter the theoretical background of the coupled hydraulic-mechanical problems is summarized. An overview of the theory of porous media (TPM) based on the theory of mixture and the concept of volume fractions is given. Afterwards the kinematical relations and the balance relations of the mixture are incorporated and the relating constitutive equations introduced. The chapter is restricted to linear elasticity, while extensions due to non linear elastic material behavior and plastic effects are discussed in the following chapters. Finally, this chapter provides a short introduction to the mathematical formulation of the problem.

Chapter 3 - A non linear elastic compressibility model This chapter deals with non linear effects in the compressive behavior of porous media. Starting with a general approach for elastic material it shortly introduces the theory of a linear elastic compressible material. Subsequently the necessity of a non linear elastic compressible model for geometric linear problems is pointed out. The development of the model is motivated, before the physical as well as the mathematical background and the derivation are presented. The mathematical and physical outcomes of the proposed model are discussed and validated by comparison with experimental results. Finally, the area of validity is discussed.

Chapter 4 - Elasto-plasticity Chapter 4 starts with an insight into the history of plastic material modeling. Beginning from the first approaches for metal plasticity, the models are continuously enhanced in various ways to provide their applicability for cohesive soils. After that introduction, the main theoretical assumptions of elasto-plasticity models are shortly summarized. Finally, a pressure sensitive, strain hardening and softening model of the Cam-Clay type is introduced and its algorithmic formulation is given.

Chapter 5 - Numerical solution As the finite element method turned out to be very robust and flexible, it is used for the numerical solution of the proposed problems. Accordingly, a short introduction is given in this chapter. Afterwards, the relating mathematical treatment as well as the usage of the finite element method for the derived balance equations are presented for a general coupled hydraulic-mechanical problem. Finally, some common solvers are referred to and a short introduction to the FEM code RockFlow is given.

Chapter 6 - Benchmarks and applications The following benchmarks and applications are presented and discussed:

Step-wise compression test

Assuming the material to behave non linear due to very low porosities, the resulting deformation and pressure fields have to be investigated by the proposed non linear elastic compressibility model. The difference between the linear and the non linear model as well as the influence of the permeability are presented within this benchmark. The aspects leading to a significant impact of the non linear model are pointed out.

Step-wise compression test on a preloaded sample

In many applications an initial state has to be prescribed in terms of initial stresses or initial compression associated with a predefined porosity. Therefore, the possibility to determine a preloaded initial case is given in the model. The influence of this initial state on the compression behavior is presented and an overview concerning the influence of the existing pore space is given.

Foundation problem

Many geotechnical applications imply an initial consolidation of the material which depends strongly on the geological depth. Consequently, a foundation problem on a nonuniformly preconsolidated soil is simulated. The arising plastic strains due to the pressure sensitive elasto-plastic model are presented within this section.

Hardening and softening found in a triaxial test

The triaxial test is a common laboratory experiment within the context of geotechnical investigations. Depending on the kind and actual state of the material, the material indicates hardening or softening due to compression. The ability to simulate these effects with the proposed model of the Cam-Clay type is shown in this section.

Deformation induced strain dependent permeability

Beside the classical couplings, the hydraulic process can be influenced by a strain dependent permeability due to various processes like pure deformation or swelling and shrinkage of the material. Additionally, the arising strains are affected by the chosen constitutive model. This example focuses on the impact of mechanical deformation on the strain dependent permeability. Within this context, the incorporation of plastic effects has an impact on migration problems in low permeable materials as they are investigated in this work.

Swelling induced strain dependent permeability

Swelling or shrinkage of a material is induced by a saturation change. The occurring volumetric swelling strains have an impact on the strain dependent permeability, which is investigated here. Related to this example, the influence of a swelling induced strain dependent permeability on the hydraulic process is presented within the context of the TDR experiment.

Migration test in a bentonite-sand-mixture („TDR experiment“)

This application deals with a coupled hydraulic-mechanical process at unsaturated conditions in a bentonite-sand-mixture with a very low permeability. Due to the precise description of the experiment and the well investigated material properties, it provides an insight in the capabilities and limitations of the simulation tool.

Chapter 7 - Summary

Chapter 2

Theoretical background

The work at hand focuses on the numerical simulation of geotechnical problems. Accordingly, this chapter gives a short introduction to the theoretical background of the theory of porous media which is used to picture the geologic material. To describe these physical relations in a mathematical way, the classical continuum theory is applied to state the mechanical subproblem. Combined with the hydraulic subproblem and related constitutive laws, the balance relations of the mixture are formulated. They build the foundation for the numerical problem.

2.1 Theory of porous media

The *Theory of Porous Media* (TPM) is a phenomenological theory which is used for volumetrically coupled solid-fluid aggregates. There exist various fields of applications in many departments. For example biomechanical problems like the simulation of load distributions in bones or flow processes in veins and arteries are investigated by the TPM. Concerning the vehicle manufacturing porous polymers like dampers are simulated and finally, in the area of geotechnics, materials like claystone, sand and rock salt are treated with this theory. Summarizing this, materials which are build by an immiscible mixture of a solid skeleton and a fluid pore content that should be analyzed on the basis of a continuum mechanical method can be investigated by the TPM. This is a continuum approach of multiphasic materials based on the *Theory of Mixtures (TM)* extended by the *Concept of Volume Fractions*. Especially for geotechnical problems this procedure is reasonable as most of the applications provide not enough information of the micromechanical constitution of the material. Consequently, a homogenization of the material, as it is done by the *Theory of Mixture (TM)* is necessary. In the following a short introduction to the TPM is given, for more information please refer to (Ehlers & Bluhm, 2002), (Ehlers, 1989) or (de Boer & Ehlers, 1986). An overview of the historical evolution is presented in (de Boer, 2000).

2.1.1 Theory of mixture

Within this theory, a *Representative Elementary Volume (REV)* is defined and the real microstructure is statistically smeared out through this considered domain. The REV has to be on the one hand large enough to allow for a statistical statement and on the other hand small enough in comparison to the macroscopic domain for the application of scale separation arguments. More information on the TM can be found in (Truesdell & Toupin, 1960). As the TM incorporates no measure of any kind of microscopic information, the solution of the presented problems also requires the usage of the *Concept of Volume Fractions*.

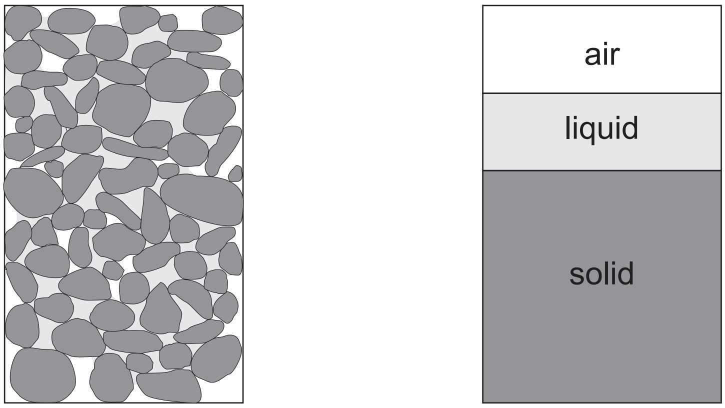

Figure 2.1: Porous medium simplified to a homogenized model.

2.1.2 Concept of volume fractions

The considered volume consists of k individual superimposed and interacting materials which compose the multiphasic aggregate. These constituents are statistically distributed over the control space. The total continuum ϕ is defined by the sum of the continua ϕ^α with $(\alpha = 1, ..., k)$

$$\phi = \sum_{\alpha=1}^{k} \phi^\alpha. \tag{2.1}$$

Thus, each spatial point x of the control space Ω is simultaneously occupied by particles P^α of all k constituents composing the multiphasic aggregate. Consequently, the mathematical functions for the description of the geometrical and physical properties of the individual materials are field functions defined all over the control space. The volume V of the overall multiphasic aggregate B might also be written in its integral form. This is used for the kinematical description and defined in equation 2.49. Within the context of volume fractions the volume results from the sum of the partial volumes of the constituents ϕ^α in B:

$$V = \int_B \mathrm{d}v = \sum_{\alpha=1}^{k} V^\alpha \tag{2.2}$$

with

$$V^\alpha = \int_B \mathrm{d}v^\alpha = \int_B n^\alpha \mathrm{d}v. \tag{2.3}$$

Here, n^α denotes the porosity of the constituent ϕ^α which is defined as

$$n^\alpha = \frac{\mathrm{d}v^\alpha}{\mathrm{d}v}. \tag{2.4}$$

Within the context of porous media, it is assumed, that the pore space is completely filled out by the defined constituents. Especially for various applications in the field of coupled hydraulic-mechanical problems, it is reasonable to introduce the saturation S. For that, we assume the material to consist of a single porous skeleton ϕ^s and k-1 pore fluids ϕ^β. Incorporating

$$n^f = \sum_{\beta=1}^{k-1} n^\beta \tag{2.5}$$

the saturation yields

$$S^\beta = \frac{n^\beta}{n^f}. \tag{2.6}$$

For geotechnical problems many publications establish the void ratio e instead of the porosity. e is defined by

$$e^f = \frac{\mathrm{d}v^f}{\mathrm{d}v^s} \tag{2.7}$$

where v^s is the volume of the skeleton and v^f the volume of the pore fluids respectively. The relation between porosity and void ratio remains

$$e^f = \frac{n^f}{(1-n^f)}. \tag{2.8}$$

Within the context of this theory, two different definitions of the density of a material are established.

- **Definition of the mean particle density**
  The mass of the constituent α is related to its volume. This definition is called realistic or effective density and results to

$$\hat{\rho}^\alpha = \frac{\mathrm{d}m^\alpha}{\mathrm{d}v^\alpha}. \tag{2.9}$$

- **Definition of the bulk density**
  The mass of the constituent α is related to the total volume of the element. This density is called global or bulk density. As in most of the applications this material parameter is known, this definition is used in the following chapters:

$$\rho^\alpha = \frac{\mathrm{d}m^\alpha}{\mathrm{d}v}. \tag{2.10}$$

2.2 Kinematical relations

The kinematical relations imply information on all quantities depending on the motion of a body. Within a continuum mechanical approach, the motion of all material points of the body represents the motion of the body. This body motion is described by the deformation in time and the definition of corresponding strains and deformation tensors. The relating definitions are introduced in the following chapter. Detailed information on the theoretical background can be found in (Haupt, 2002), (Bathe, 1996), (Stein & Barthold, 1996) amongst others.

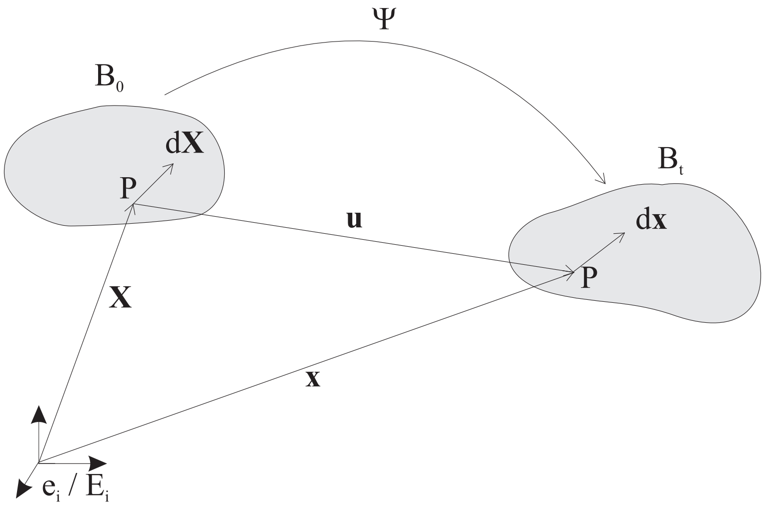

Figure 2.2: Initial and current configuration and relating definitions.

2.2.1 Initial and current configuration

Let a body *B* occupy a space B_0 at time $t_0 = 0$. Each material point *P* of the body can be identified by a unique mapping of *P* onto the Euclidean space E^3, which changes due to a deformation. To differ the initial from the current configuration, the indices 0 and t are introduced and the tensors are noted as an upper-case (initial configuration) or a lower-case (current configuration) letter.

The position vector $\mathbf{X}$ of a point *P* in the initial configuration is defined by

$$\mathbf{X} = \chi_0(P) \tag{2.11}$$

where χ_0 is the corresponding mapping in the initial configuration. In general one assumes the body *B* to be undeformed and stress free in the initial configuration. At an arbitrary time t the body occupies the space B_t, and the mapping of each material point *P* at that time is

$$\mathbf{x} = \chi_t(P) \tag{2.12}$$

where $\mathbf{x}$ is called the position vector of *P* in the current configuration, and χ_t is the mapping function in the current configuration. The mapping between $\mathbf{X}$ and $\mathbf{x}$ is shown in figure 2.2

and given by

$$\begin{aligned} \mathbf{x} &= \Psi\,\mathbf{X}, && (2.13)\\ \mathbf{X} &= \Psi^{-1}\,\mathbf{x}. && (2.14) \end{aligned}$$

The displacement $\mathbf{u}$ of *P* in time is defined as

$$\mathbf{u} = \mathbf{x} - \mathbf{X} \tag{2.15}$$

and its velocity $\mathbf{v}$ is the material time derivative of the displacements

$$\mathbf{v} = \frac{\mathrm{d}\mathbf{u}}{\mathrm{d}t} = \frac{\mathrm{d}\mathbf{x}}{\mathrm{d}t} = \dot{\mathbf{x}}. \tag{2.16}$$

The acceleration of point *P* is

$$\mathbf{a} = \frac{\mathrm{d}^2\mathbf{x}}{\mathrm{d}t^2} = \frac{\mathrm{d}\mathbf{v}}{\mathrm{d}t} = \ddot{\mathbf{x}} = \dot{\mathbf{v}}. \tag{2.17}$$

2.2.2 Deformation gradient

In general, one wants to describe the deformation in an infinitesimal environment of each material point *P* of the body in order to be able to determine the strains and rotations of the material in *P*. Therefore, it is necessary to define a mapping between infinitesimal line elements in the initial configuration $\mathrm{d}\mathbf{X}$ and the corresponding line elements in the current configuration $\mathrm{d}\mathbf{x}$.

$$\mathrm{d}\mathbf{x} = \mathbf{F} \cdot \mathrm{d}\mathbf{X} \tag{2.18}$$

with

$$\mathbf{F} = \mathrm{Grad}\,\mathbf{x} = \frac{\partial \mathbf{x}}{\partial \mathbf{X}}. \tag{2.19}$$

Here, the deformation gradient $\mathbf{F}$ is called material deformation gradient. In contrast to that, the inverse $\mathbf{F}^{-1}$ is called spatial deformation gradient and is defined by

$$\mathbf{F}^{-1} = \mathrm{grad}\,\mathbf{X} = \frac{\partial \mathbf{X}}{\partial \mathbf{x}}. \tag{2.20}$$

Depending on the displacements $\mathbf{u}$, the material deformation gradient $\mathbf{F}$ yields

$$\mathbf{F} = \mathbf{1} + \frac{\partial \mathbf{u}}{\partial \mathbf{X}} = \mathbf{1} + \mathbf{H}. \tag{2.21}$$

where $\mathbf{H}$ is the displacement gradient. The determinant of $\mathbf{F}$ is defined as the Jacobian J and equals the proportion of the density in the initial and the current configuration

$$J = \det \mathbf{F} = \frac{\rho_0}{\rho_t} > 0. \tag{2.22}$$

To debar negative volumes, J has to be positive.

Besides that, $\mathbf{F}$ is a non-singular two-point tensor which means that it can be written as

$$\mathbf{F} = F_{ij}\mathbf{e_i} \otimes \mathbf{E_j}, \tag{2.23}$$

where F_{ij} are the components of $\mathbf{F}$, $\mathbf{e_i}$ are the base vectors in the current configuration and E_j are the base vectors in the initial configuration.

Since the deformation gradient maps infinitesimal material line elements from the initial to the current configuration, one can also use it to map infinitesimal surface and volume elements. For surface elements one obtains Nanson's formula

$$\mathbf{n}\mathrm{d}a = J\mathbf{F}^{-T} \cdot \mathbf{N}\mathrm{d}A, \tag{2.24}$$

where $\mathbf{n}$ and $\mathbf{N}$ are the unit normal vectors on the surface element in the current and the initial configuration, and da and dA are the surface areas respectively. Additional usage of the Jacobian J leads to

$$\begin{aligned} d\mathbf{x} &= \mathbf{F}\mathrm{d}\mathbf{X} && (2.25)\\ da &= J\mathbf{F}^{-T}\mathrm{d}A && (2.26)\\ dv &= J\mathrm{d}V. && (2.27) \end{aligned}$$

The material time derivative of the deformation gradient is called the material deformation velocity gradient

$$\dot{\mathbf{F}} = \frac{\partial \dot{\mathbf{x}}}{\partial \mathbf{X}} \tag{2.28}$$

and its transformation to the current configuration leads to the spatial velocity gradient

$$\mathbf{l} = \dot{\mathbf{F}} \cdot \mathbf{F}^{-1} = \frac{\partial \dot{\mathbf{x}}}{\partial \mathbf{x}}. \tag{2.29}$$

2.2.3 Strain tensors

The deformation gradient is not suitable as a strain tensor, as it is asymmetric and depends on the direction and the rigid body motions. Due to the balance of momentum, the stresses are symmetric and consequently a symmetric strain tensor should be defined to derive simple material tensors. Accordingly, better descriptions for a strain tensor are defined due to the examination of surfaces built by quadratic line elements. Using the Euclidic Norm $\| \bullet \|$ defined in appendix A, the difference between initial and current configuration results to

$$\begin{aligned} \|\mathrm{d}\mathbf{x}\| \cdot \|\mathrm{d}\mathbf{x}\| - \|\mathrm{d}\mathbf{X}\| \cdot \|\mathrm{d}\mathbf{X}\| &= \mathrm{d}\mathbf{x} \cdot \mathrm{d}\mathbf{x} - \mathrm{d}\mathbf{X} \cdot \mathrm{d}\mathbf{X} && (2.30)\\ &= \mathrm{d}\mathbf{X} \cdot \mathbf{F}^T \cdot \mathbf{F} \cdot \mathrm{d}\mathbf{X} - \mathrm{d}\mathbf{X} \cdot \mathrm{d}\mathbf{X} && (2.31)\\ &= \mathrm{d}\mathbf{X} \cdot \left(\mathbf{F}^T \cdot \mathbf{F} \cdot -\mathbf{1}\right) \cdot \mathrm{d}\mathbf{X} && (2.32)\\ &= \mathrm{d}\mathbf{X} \cdot (\mathbf{C} - \mathbf{1}) \cdot \mathrm{d}\mathbf{X} && (2.33)\\ &= \mathrm{d}\mathbf{X} \cdot 2\mathbf{E} \cdot \mathrm{d}\mathbf{X} && (2.34) \end{aligned}$$

with the right Cauchy-Green tensor $\mathbf{C} = \mathbf{F}^T \cdot \mathbf{F} = \mathbf{U} \cdot \mathbf{U}$ and the Green-Lagrange strain tensor $\mathbf{E} = \frac{1}{2} \cdot (\mathbf{C} - \mathbf{1})$, defined in the initial configuration, or

$$\begin{aligned} \|\mathrm{d}\mathbf{x}\| \cdot \|\mathrm{d}\mathbf{x}\| - \|\mathrm{d}\mathbf{X}\| \cdot \|\mathrm{d}\mathbf{X}\| &= \mathrm{d}\mathbf{x} \cdot \mathrm{d}\mathbf{x} - \mathrm{d}\mathbf{x} \cdot \mathbf{F}^{-T} \cdot \mathbf{F}^{-1} \mathrm{d}\mathbf{x} && (2.35)\\ &= \mathrm{d}\mathbf{x} \cdot \left(\mathbf{1} - \mathbf{F}^{-T} \cdot \mathbf{F}^{-1}\right) \cdot \mathrm{d}\mathbf{x} && (2.36)\\ &= \mathrm{d}\mathbf{x} \cdot \left(\mathbf{1} - \mathbf{b}^{-1}\right) \cdot \mathrm{d}\mathbf{x} && (2.37)\\ &= \mathrm{d}\mathbf{x} \cdot 2\mathbf{e} \cdot \mathrm{d}\mathbf{x} && (2.38) \end{aligned}$$

with the left Cauchy-Green tensor $\mathbf{b} = \mathbf{F} \cdot \mathbf{F}^T = \mathbf{V} \cdot \mathbf{V}$ and the Euler-Almansi strain tensor $\mathbf{e} = \frac{1}{2} \cdot (\mathbf{1} - \mathbf{b}^{-1})$, defined in the current configuration. The Green-Lagrange strain tensor $\mathbf{E}$ as well as the Euler-Almansi strain tensor $\mathbf{e}$ are independent from the direction, symmetric and zero for rigid body motions. For more informations please refer to (Stein & Barthold, 1996).

2.2.4 Linearization of the strain tensor

As the strain tensor for the geometrically linear theory arises from the Green-Lagrange strain tensor, let‘ s have a closer look on it. With (2.21) it results

$$\begin{aligned} \mathbf{E} &= \frac{1}{2} \cdot \left(\mathbf{F}^T \cdot \mathbf{F} - \mathbf{1}\right) && (2.39)\\ &= \frac{1}{2} \cdot \Big((\mathbf{1} + \mathbf{H})^T \cdot (\mathbf{1} + \mathbf{H}) - \mathbf{1}\Big) && (2.40)\\ &= \frac{1}{2} \cdot \left(\mathbf{H} + \mathbf{H}^T + \mathbf{H}^T \cdot \mathbf{H}\right). && (2.41) \end{aligned}$$

As can be seen, the strain energy tensor can be split additively into a linear and a nonlinear part

$$\begin{aligned} \mathbf{E} &= \mathbf{E}_{\mathbf{lin}} + \mathbf{E}_{\mathbf{nonlin}} && (2.42)\\ &= \frac{1}{2} \cdot \left(\mathbf{H} + \mathbf{H}^T\right) + \frac{1}{2} \cdot \left(\mathbf{H}^T \cdot \mathbf{H}\right). && (2.43) \end{aligned}$$

Assuming the strains to be small in the sense of the geometric linear theory, it yields $\mathbf{H} = \mathrm{Grad}\,\mathbf{u} \ll 1$ and the nonlinear part can be neglected in comparison to the linear part. This linearization of $\mathbf{E}$ and accordingly $\mathbf{e}$ leads to the strain measure for the geometric linear theory

$$\boldsymbol{\varepsilon} = \frac{1}{2} \left(\frac{\partial \mathbf{u}}{\partial \mathbf{x}} + \left(\frac{\partial \mathbf{u}}{\partial \mathbf{x}} \right)^T \right). \qquad (2.44)$$

2.2.5 Stress tensors

On a solid body *B* two fundamental types of forces may act. Body forces are described by the body force density $\mathbf{b}$ and surface forces are described by the tractions $\mathbf{t}$. While body forces like the gravitation are related to the entire volume of the material, the surface tractions just act on the boundary of the body. In the 3D case this means that surface tractions are vectors with the physical unit $[F/L^2]$ and body force densities are vectors with $[F/M]$. Surface traction vectors are called stress vectors. Cauchy‘s theorem states that the stress vector $\mathbf{t}$ on the surface $\mathrm{d}a$ of an arbitrary cut of the body is a linear function of the outer normal vector $\mathbf{n}$ on this cut and can be written as

$$\mathbf{t}(\mathbf{x}, t, \mathbf{n}) = \boldsymbol{\sigma}_{\mathrm{tot}}(\mathbf{x}, t) \cdot \mathbf{n}(\mathbf{x}, t) \tag{2.45}$$

with the symmetric Cauchy stress tensor $\boldsymbol{\sigma}_{\mathrm{tot}} = \boldsymbol{\sigma}_{\mathrm{tot}}^T$. Summarizing body forces and the surface tractions leads to the totally force vector

$$\mathbf{f}(B, t) = \int_B \rho_{\mathrm{m}}(\mathbf{x}, t)\, \mathbf{b}\, \mathrm{d}v + \int_{\partial B} \mathbf{t}\, \mathrm{d}a \tag{2.46}$$

where ρ_{m} is the averaged mass density of the solid, defined in equation (2.50).

As the Cauchy stress tensor is defined in the current configuration, the *first Piola-Kirchhoff stress tensor* $\mathbf{P} = J\boldsymbol{\sigma}_{\mathrm{tot}} \cdot \mathbf{F}^{-T}$ is introduced, mapping a vector from the initial to the current configuration

$$\mathbf{t}\, \mathrm{d}a = \boldsymbol{\sigma}_{\mathrm{tot}} \cdot \mathbf{n}\, \mathrm{d}a = J\boldsymbol{\sigma}_{\mathrm{tot}} \cdot \mathbf{F}^{-T} \cdot \mathbf{N}\, \mathrm{d}a = \mathbf{P} \cdot \mathbf{N}\, \mathrm{d}A. \tag{2.47}$$

Unfortunately, this stress tensor is nonsymmetric. As a matter of fact, the *second Piola-Kirchhoff stress tensor* $\mathbf{S}$ is defined by

$$\mathbf{S} = \mathbf{F}^{-1} \cdot \mathbf{P} = J\mathbf{F}^{-1} \cdot \boldsymbol{\sigma}_{\mathrm{tot}} \cdot \mathbf{F}^{-T}. \tag{2.48}$$

This tensor does not have any physical meaning, but due to its mathematical advantages, it is usually used for the derivation of material tensors, as it is presented in chapter 3.

2.3 Balance relations of the mixture

Balance or conservation principles express fundamental physical observations concerning the interaction of a continuous medium and the environment. They reflect the balance of the most important physical measures for the body of interest. Within the classical theory of mechanics, this implies the balance of mass, the balance of linear and angular momentum, the balance of energy and the balance of entropy (please refer to (Bear & Verruijt, 1987), (Zienkiewicz & Taylor, 2005), (Lewis & Schrefler, 2000)). The balance equations can be written in the integral form for the whole body *B* or in the local form, concerning every single point *P*. One has to keep in mind, that the volume $\mathbf{V}$ is not necessarily constant over the time. Rather, it yields

$$\mathrm{d}v = J\, \mathrm{d}V. \tag{2.49}$$

Application to coupled hydraulic-mechanical problems

The classical mechanical theory should be applied for a hydraulic-mechanically coupled problem. For this case, the porous medium is assumed to be composed of a gaseous phase $((\bullet)^g)$, water as the liquid phase ($(\bullet)^{w}$) and the solid skeleton ($(\bullet)^{s}$). As it is defined in equation (2.6), the medium is called saturated, if there is no gaseous phase in the body, otherwise it is called unsaturated. Consequently, for unsaturated single phase flow the averaged density ρ_{m} is given by

$$\rho_{\mathrm{m}} \;=\; (1-n)\rho^{\mathrm{s}} + n\rho^{\mathrm{w}}S^{\mathrm{w}} + n\rho^{\mathrm{g}}S^{\mathrm{g}} \tag{2.50}$$

where n is the porosity, S^{w} is the water saturation, S^{g} the gas saturation, ρ^{w}, ρ^{s} and ρ^{g} are the density of the water, the solid body and the gaseous phase, respectively. In many cases, the equation can be reduced to the first two terms, as the last one is significantly smaller. For a water saturated continuum, the equation simplifies to

$$\rho_{\mathrm{m}} \;=\; (1-n)\rho^{\mathrm{s}} + n\rho^{\mathrm{w}}. \tag{2.51}$$

2.3.1 Conservation of mass

The mass of a saturated body *B* with a mass density $\rho_{\mathrm{m}}(\mathbf{x},t)$ results to

$$m(B,t) = \int_{B} \rho_{\mathrm{m}} \mathrm{d}v = \int_{B_0} \rho_{\mathrm{m}} J \mathrm{d}V = \int_{B_0} \rho_{\mathrm{m},0} \mathrm{d}V \tag{2.52}$$

with

$$\rho_{\mathrm{m},0} = \rho_{\mathrm{m}} J. \tag{2.53}$$

As the mass of a body has to be constant if no fluxes occur, the time derivative of the mass should vanish and for the balance of mass, it yields

$$\begin{aligned} \dot{m} &= \frac{\mathrm{d}}{\mathrm{d}t}\int_{B} \rho_{\mathrm{m}} \mathrm{d}v = \frac{\mathrm{d}}{\mathrm{d}t}\int_{B_0} \rho_{\mathrm{m}}\, J \,\mathrm{d}V = \int_{B_0} \frac{\mathrm{d}}{\mathrm{d}t}\left(\rho_{\mathrm{m}}\, J\right)\, \mathrm{d}V \\ &= \int_{B_0} \left(\dot{\rho}_{\mathrm{m}} + \rho_{\mathrm{m}}\, \nabla\cdot\dot{\mathbf{x}}\right) J \,\mathrm{d}V = \int_{B} \left(\dot{\rho}_{\mathrm{m}} + \rho_{\mathrm{m}}\, \nabla\cdot\dot{\mathbf{x}}\right) \mathrm{d}v \end{aligned} \tag{2.54}$$

with

$$\dot{J} = J\, \nabla\cdot\dot{\mathbf{x}} \tag{2.55}$$

with the velocity $\mathbf{v} = \dot{\mathbf{x}}$. The local form of the mass balance is often called continuity equation and is given for an arbitrary volume by

$$\dot{\rho}_{\mathrm{m}} + \rho_{\mathrm{m}}\, \nabla\cdot\dot{\mathbf{x}} = 0. \tag{2.56}$$

Investigating the hydraulic subproblem in an unsaturated porous medium, the mass balance equation may incorporate various effects. Detailed information can be found in (Lewis & Schrefler, 2000).

Application to coupled hydraulic-mechanical problems

For the hydraulic-mechanically coupled case, neglecting thermal effects and using the *Richards' Approximation*, the mass balance for the water species results to

$$n\rho^{\mathrm{w}}\frac{\partial S^{\mathrm{w}}}{\partial t}+\rho^{\mathrm{w}}S^{\mathrm{w}}\nabla\cdot\frac{\partial\mathbf{u}^{\mathrm{s}}}{\partial t}=0 \tag{2.57}$$

which directly results from equation (2.56) incorporating equation (2.50) and assuming the grains to be incompressible. The additional incorporation of a flux boundary condition leads to the typical description of the conservation of mass within the context of a hydraulic-mechanically coupled problem:

$$\nabla\cdot\mathbf{q}^{\mathrm{w}}+n\rho^{\mathrm{w}}\frac{\partial S^{\mathrm{w}}}{\partial t}+\rho^{\mathrm{w}}S^{\mathrm{w}}\nabla\cdot\frac{\partial\mathbf{u}^{\mathrm{s}}}{\partial t}=0 \tag{2.58}$$

Here, the variable $\mathbf{q}^{\mathrm{w}}$ denotes the flux of water over the boundary.

2.3.2 Conservation of linear momentum

The linear momentum $\mathbf{I}$ of a body is defined by

$$\mathbf{I}=\int_B\rho_{\mathrm{m}}\dot{\mathbf{x}}\,\mathrm{d}v. \tag{2.59}$$

The conservation of the linear momentum is also called the kinetic equilibrium of forces and indicates that the temporal change of the linear momentum $\dot{\mathbf{I}}$ equals the sum of all forces acting on the body.

$$\frac{\mathrm{d}}{\mathrm{d}t}\int_B\rho_{\mathrm{m}}\dot{\mathbf{x}}\,\mathrm{d}v=\int_B\rho_{\mathrm{m}}\mathbf{b}\,\mathrm{d}v+\int_{\partial B}\mathbf{t}\,\mathrm{d}a=\mathbf{f}. \tag{2.60}$$

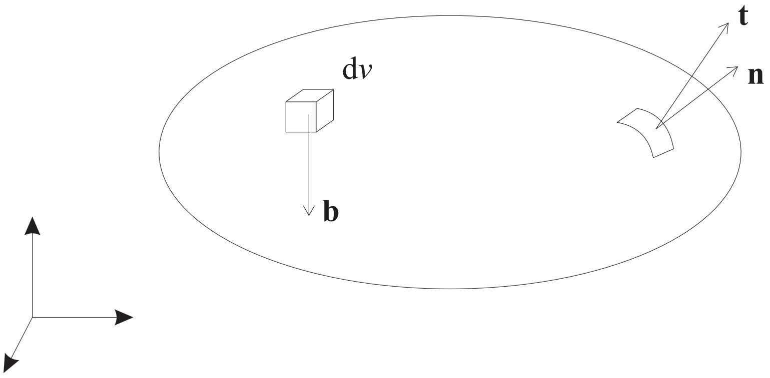

Figure 2.3: Forces acting on the body.

As explained in chapter 2.2.5 there exist body forces given by the body force density $\mathbf{b}$ and surface tractions given by $\mathbf{t}$. Using the Cauchy theorem given in equation (2.45), the local mass balance given in equation (2.56) and the Gauss‘ integral theorem (divergence theorem) given by

$$\int_B \nabla \cdot \boldsymbol{\sigma}_{\mathrm{tot}} \, \mathrm{d}v = \int_{\partial B} \boldsymbol{\sigma}_{\mathrm{tot}} \mathbf{n} \, \mathrm{d}a \tag{2.61}$$

leads to the following form of the balance of linear momentum

$$\int_B \rho_{\mathrm{m}} \ddot{\mathbf{x}} \, \mathrm{d}v = \int_B \left(\nabla \cdot \boldsymbol{\sigma}_{\mathrm{tot}} + \rho_{\mathrm{m}} \mathbf{b} \right) \mathrm{d}v \tag{2.62}$$

with the acceleration $\mathbf{a} = \dot{\mathbf{v}} = \ddot{\mathbf{x}}$. Consequently, the local form of the conservation of linear momentum, also called strong form of the equilibrium or Cauchy equation of motion yields

$$\rho_{\mathrm{m}} \ddot{\mathbf{x}} = \nabla \cdot \boldsymbol{\sigma}_{\mathrm{tot}} + \rho_{\mathrm{m}} \mathbf{b}. \tag{2.63}$$

Application to coupled hydraulic-mechanical problems

This work focuses on quasi-statical mechanical problems. As a matter of fact, the left part of the equation can be neglected. Also, for geotechnical problems, the body force density normally equals the gravity $\mathbf{g}$ and consequently the static equilibrium equation results to

$$\mathbf{0} = \nabla \cdot \boldsymbol{\sigma}_{\mathrm{tot}} + \rho_{\mathrm{m}} \mathbf{g} \tag{2.64}$$

with the total stress of the solid $\boldsymbol{\sigma}_{\mathrm{tot}}$, the acceleration due to gravity $\mathbf{g}$ and the averaged density ρ_{m}.

2.3.3 Conservation of angular momentum

The angular momentum $\mathbf{L}$ of a body is defined by

$$\mathbf{L} = \int_B \rho_{\mathrm{m}} \left(\mathbf{x} - \mathbf{x}_0 \right) \times \dot{\mathbf{x}} \, \mathrm{d}v. \tag{2.65}$$

The conservation of the angular momentum is also called the kinetic equilibrium of moments and indicates that the temporal change of the angular momentum $\dot{\mathbf{L}}$ equals the sum of all external moments acting on the body. The reference point $\mathbf{x}_0$ is arbitrary but fixed.

$$\frac{\mathrm{d}}{\mathrm{d}t} \int_B \rho_{\mathrm{m}} \left(\mathbf{x} - \mathbf{x}_0 \right) \times \dot{\mathbf{x}} \, \mathrm{d}v = \int_B \rho_{\mathrm{m}} \left(\mathbf{x} - \mathbf{x}_0 \right) \times \mathbf{b} \, \mathrm{d}v + \int_{\partial B} \left(\mathbf{x} - \mathbf{x}_0 \right) \times \mathbf{t} \, \mathrm{d}a. \tag{2.66}$$

With the balance of linear momentum given in equation (2.64), the Cauchy theorem given in equation (2.45) and the Gauss integral theorem given in equation (2.61) it can be shown that the local form of the balance of angular momentum leads to the symmetry of the Cauchy stress tensor

$$\boldsymbol{\sigma}_{\mathrm{tot}} = \boldsymbol{\sigma}_{\mathrm{tot}}^T. \tag{2.67}$$

2.3.4 Conservation of energy

The energy balance equation is also called *first law of thermodynamics*. It states that the temporal change of the total energy of a system equals the sum of the work supplied to a body due to mechanical or thermal power. With the kinetic energy K, the internal energy U, the mechanical power M and the thermal power T supplied to the body it results to

$$\frac{d}{dt}(K+U) = M + T \tag{2.68}$$

with the kinetic energy

$$K = \frac{1}{2}\int_B \rho\,\dot{\mathbf{x}}\cdot\dot{\mathbf{x}}\,\mathrm{d}v, \tag{2.69}$$

the internal energy given as a function of the specific internal energy u composed of the strain energy due to elastic strains and the stored heat

$$U = \int_B \rho\,u\,\mathrm{d}v, \tag{2.70}$$

the mechanical power resulting from all external forces acting on the body

$$M = \int_B \rho_{\mathrm{m}}\,\mathbf{b}\cdot\dot{\mathbf{x}}\,\mathrm{d}v + \int_{\partial B} \mathbf{t}\cdot\dot{\mathbf{x}}\,\mathrm{d}a, \tag{2.71}$$

the thermal power resulting from the heat due to internal heat sources given by $\rho\,r$ and the heat flux through the surface given by the heat flux vector $\mathbf{q}$ over the surface

$$T = \int_B \rho\,r\,\mathrm{d}v - \int_{\partial B} \mathbf{q}\cdot\mathbf{n}\,\mathrm{d}a. \tag{2.72}$$

Following these definitions the first law of thermodynamics yields

$$\frac{d}{dt}\int_B \rho\left(u + \frac{1}{2}\dot{\mathbf{x}}\cdot\dot{\mathbf{x}}\right)\mathrm{d}v = \int_B (\rho\,r + \rho_{\mathrm{m}}\,\mathbf{b}\cdot\dot{\mathbf{x}})\,\mathrm{d}v + \int_{\partial B} (\mathbf{t}\cdot\dot{\mathbf{x}} - \mathbf{q}\cdot\mathbf{n})\,\mathrm{d}a \tag{2.73}$$

which can be reformulated to the local form using the Cauchy stresses, the divergence theorem and the balance of linear momentum:

$$\rho\,\dot{u} = \boldsymbol{\sigma}_{\mathrm{tot}} : \mathbf{l} + \rho\,r - \nabla\cdot\mathbf{q} \tag{2.74}$$

2.3.5 Entropy inequality

Up to this point, the proposed formulation is only based on various balance equations. Furthermore, the irreversibility of thermomechanical processes have to be assured. This is done by the entropy inequality, also called *Clausius-Duhem* inequality. The introduced entropy η is not a conserved measure, the increase of entropy in a system is larger than or for reversible processes equal to the entropy brought into the system. This is given by

$$\frac{d}{dt}\int_B \rho\eta\,\mathrm{d}v \geq \int_B \rho\frac{r}{\Theta}\,\mathrm{d}v - \int_{\partial B} \frac{1}{\Theta}\mathbf{q}\cdot\mathbf{n}\,\mathrm{d}a \tag{2.75}$$

with the temperature field Θ. Introducing the intrinsic *free Helmholtz energy* ψ

$$\psi = u - \eta\,\Theta \tag{2.76}$$

the local form of this equation results to

$$-\rho\left(\dot{\psi} + \eta\dot{\Theta}\right) + \boldsymbol{\sigma}_{\text{tot}} : \mathbf{l} - \frac{1}{\Theta}\,\mathbf{q}\cdot\text{grad}\,\Theta \geq 0 \tag{2.77}$$

using the divergence theorem and the first law of thermodynamics.

For the isothermal case this law simplifies to

$$-\rho\dot{u} + \boldsymbol{\sigma}_{\text{tot}} : \mathbf{l} \geq 0 \qquad -\rho\dot{u} + \mathbf{S} : \dot{\mathbf{E}} \geq 0 \tag{2.78}$$

with u being the strain energy due to elastic strains and related to the mass. In the field of classical mechanics the energy on a specific volume is interesting. Consequently, the strain energy u is modified to the strain energy density function W

$$W = \rho u. \tag{2.79}$$

The material behavior can now be described by the strain energy density function W, which will be discussed in a detailed way in chapter 3.

2.4 Constitutive equations

Constitutive relations are equations that relate causes and effects. They may arise from experimental tests or other kinds of material testing and involve material parameters. While the balance equations like conservation of linear momentum or mass have to be fulfilled for every problem, the constitutive equations incorporate special properties of the problem (e.g. material properties). As this work focuses on hydraulic-mechanically coupled problems with unsaturated single phase flow and swelling, this chapter presents the most important constitutive relations concerning this field of applications. It starts with the equations relating the mechanical subproblem and continues with the description of the relations concerning the hydraulic problem.

2.4.1 Linear elastic, isotropic material model

The constitutive equation which gives the relationship between strains and stresses for the linear elastic, isotropic, linear geometric case is commonly given by the so-called *Hooke's law* - which is more an empirical approach than a law - but that should not be discussed here. As it is the common denotation, the presented relation will be referred to as Hooke's law within this work. For detailed information please refer to (Desai & Siriwardane, 1984) amongst others. Hooke's law was originally developed by Hooke in 1676 concerning the behavior of springs. Later it was extended to 3D continuous bodies by Cauchy. This extension is still widely used and called the *generalized Hooke's law*. This law incorporates the so-called elastic constants into the numerical model. For the isotropic case there exist five elastic constants - four of them give a relation between stresses and strains, the fifth one (*Poisson's ratio*) relates one extensional strain to another (see e.g. (Stein & Barthold, 1996)). The generalized Hooke's law contains two arbitrary parameters, as only two of the five given constants are independent, respectively. For the so-called *Lamé parameters* λ and μ it results to

$$\boldsymbol{\sigma}_{\text{eff}} = \lambda \operatorname{tr} \boldsymbol{\varepsilon}(\mathbf{u}) \mathbf{1} + 2\mu \boldsymbol{\varepsilon}(\mathbf{u}) \tag{2.80}$$

$$= \mathbb{C} : \boldsymbol{\varepsilon} \tag{2.81}$$

with the material matrix $\mathbb{C}$. More information as well as an extension of this material model, incorporating non linear material behavior, are given in chapter 3.

2.4.2 Effective stresses

The *Terzaghi approach* of effective stresses is one of the most important constitutive approaches for soil mechanics. It is explained in detail in (Terzaghi & Fröhlich, 1936) and (Terzaghi, 1943) and states that a load applied on a fully saturated body is ablated by the solid skeleton as well as by the pore water in the body (see figure 2.4).

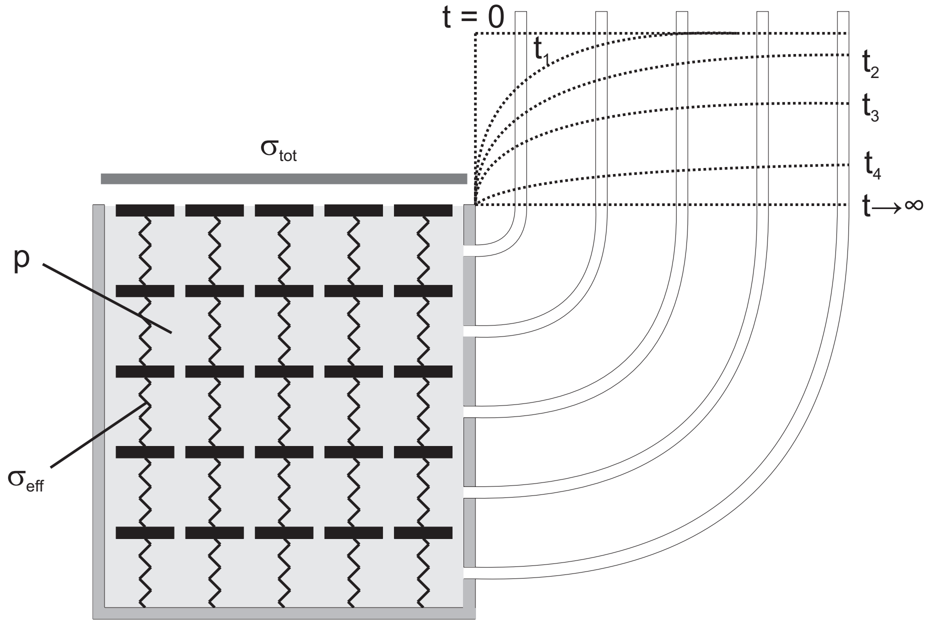

Figure 2.4: Terzaghi's approach of effective stresses according to (Terzaghi, 1943) .

As a matter of fact, it leads to pore water pressures as well as to effective stresses, which act on the solid skeleton and can be calculated by the difference between the applied load and the pore water pressure

$$\boldsymbol{\sigma}_{\text{eff}} = \boldsymbol{\sigma}_{\text{tot}} - (-p\mathbf{1}). \tag{2.82}$$

Assuming the area of interest to be permeable at least at one boundary, the process becomes time-dependent due to this effect, as the pressure gradient leads to a time-dependent fluid flow (please refer to figure 2.4).

Additional consideration of compressible grains

The presented relationship turned out to depend on the material properties of the solid. Assuming the soil particles to be compressible in an essential amount, the *Biot coefficient* α should be used as an additional multiplicative parameter (see equation (2.85)). It remains

$$\alpha = 1 - \frac{K}{K_s}, \tag{2.83}$$

with the bulk modulus of the porous medium K and the bulk modulus of the solid grains K_s. As the grain compressibility of most of the materials considered in this work is essentially smaller than the compressibility of the porous medium we assume

$$\alpha \equiv 1.0. \tag{2.84}$$

Additional consideration of high capillary pressures

Additionally, there exist various approaches to extend this model for unsaturated problems. Within this range, there exist capillary pressures and the proposed physical effect makes sense theoretically. But especially for high negative pressures at a low saturation level, the high capillary pressures lead to an overestimation of the effect. Assuming the pore pressure to be defined by equation (2.96) and simplified by the proposed Richards‘ approximation leads to an attenuation of the influence of high capillary pressures due to the incorporation of the saturation S^{w}. The effective stress law yields

$$\boldsymbol{\sigma}_{\mathrm{eff}} = \boldsymbol{\sigma}_{\mathrm{tot}} - (-\alpha S^{\mathrm{w}} p^{\mathrm{w}} \mathbf{1}). \tag{2.85}$$

Within the literature, this approach is found to be modified in various ways. The modification given by (Lu & Likos, 2004) is presented and applied in section 6.7.

2.4.3 Linear swelling model

Some geotechnical materials (e.g. claystone) incorporate a volumetric deformation due to a change of the water content. In order to incorporate this swelling or shrinkage of the material, an extension of the *Biot consolidation theory* is used. The calculation of the stresses for the elastic case remains

$$\boldsymbol{\sigma}_{\mathrm{eff}} = \mathbb{C} : \boldsymbol{\varepsilon} \tag{2.86}$$

with the fourth-order tensor $\mathbb{C}$ comprised of the linear elastic coefficients and the strains $\boldsymbol{\varepsilon}$ resulting to

$$\boldsymbol{\varepsilon} = \boldsymbol{\varepsilon}^{\mathrm{el}} + \boldsymbol{\varepsilon}^{\mathrm{sw}} \tag{2.87}$$

whereas

$$\varepsilon^{\mathrm{sw}} = \beta^{\mathrm{sw}} \Delta S^{\mathrm{w}} \mathbf{1} \tag{2.88}$$

$$\Delta S^{\mathrm{w}} = S^{\mathrm{w}} - S^{\mathrm{w}}_0 \tag{2.89}$$

where S^{w}_0 is the reference saturation, belonging to the reference volumetric strain $\varepsilon_0^{\mathrm{vol,sw}}$. S^{w} equals the actual saturation, while it is in the range between S^{w}_{min} and $S^{\mathrm{w}}_{\mathrm{max}}$. Out of this range, the marginal value has to be used (see figure 2.5).

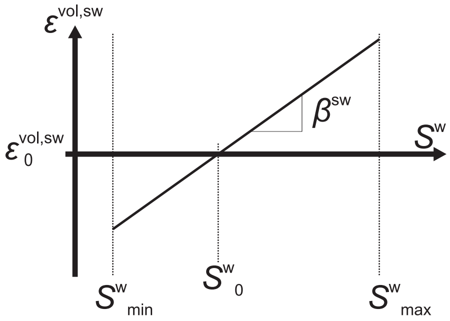

Figure 2.5: Linear swelling model.

2.4.4 Strain dependent porosity

The porosity n can be recalculated depending on the initial porosity n_0 and the volumetric strain caused by deformation $\operatorname{tr}\varepsilon$ and/or swelling/shrinkage $\operatorname{tr}\varepsilon^{\mathrm{sw}}$ of the material. It results to

$$n = n_0 + \operatorname{tr}\varepsilon - \operatorname{tr}\varepsilon^{\mathrm{sw}}. \tag{2.90}$$

This approach assumes the volumetric strain caused by deformation to affect the pore space, not the size of particles. Consequently, an expansion will lead to an increase; a compression to a decrease of pore space. In contrast to that, swelling or shrinkage leads to a change of the particle size of the material. As a matter of fact, the pore space will decrease while swelling, and increase while shrinkage occurs.

2.4.5 Darcy´s law

Darcy´s law is a generalized relationship for flow of Newtonian fluids in porous media. It can be derived from the conservation of linear momentum supplemented by a material dependent proportionality constant $\mathbf{k_f}$ which quantifies the permeability of the material for a fluid. It was established under saturated flow conditions but it may be transfused for unsaturated and multiphasic flow to the *modified Darcy´s law*. Consequently, the liquid flux for the coupled hydraulic-mechanical case is governed by:

$$\mathbf{q}^{\mathrm{w}} = -\frac{\mathbf{k}\, k_{\mathrm{rel}}}{\eta}(\nabla p - \rho^{\mathrm{w}} \mathbf{g}) \tag{2.91}$$

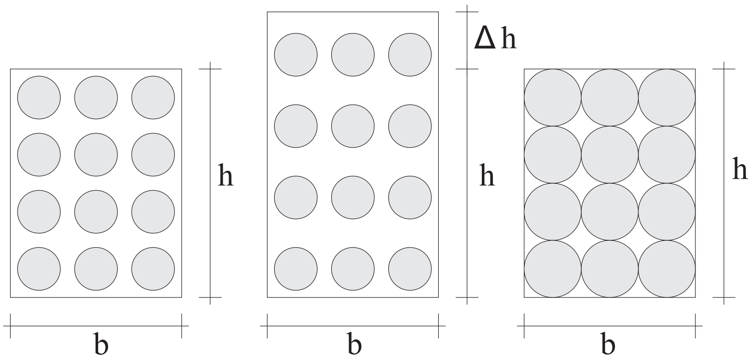

Figure 2.6: Modification of the initial porosity (left) due to deformation (center) and swelling (right).

Here, the liquid flux $\mathbf{q}^{\mathrm{w}}$ results from the intrinsic permeability $\mathbf{k}$, the relative permeability k_{rel} (see section 2.4.6), the liquid pressure p, the fluid absolute viscosity η, the density of water ρ^{w} and the acceleration due to the gravity vector $\mathbf{g}$.

Within this approach the intrinsic permeability $\mathbf{k}$ given in [m^2] is used. $\mathbf{k}$ depends only on the nature of the porous medium. As mentioned above, the classical derivation of Darcy's law incorporates the proportionality constant $\mathbf{k_f}$ given in [m/s] which depends on the attributes of the fluid as well as on the attributes of the solid. The relation between the proportionality constant $\mathbf{k_f}$, and the intrinsic permeability $\mathbf{k}$ is given by

$$\mathbf{k_f} = \mathbf{k}\,\frac{\rho^{\mathrm{w}}\,g}{\eta}. \qquad (2.92)$$

2.4.6 Definition of a relative permeability

The permeability of a material is on the one side affected by the saturation, on the other side by the porosity of the material. These dependencies are treated in different ways.

1. *Saturation dependent permeability*
   The saturation dependency is commonly treated by the definition of a relative permeability k_{rel}. The absolute permeability, used in Darcy's law results from the multiplication of this relative permeability with an intrinsic permeability k_{int}. The relationship of relative permeability and saturation is given for example by the *van Genuchten* or the *Brooks-Corey* relation. Exemplarily, a derived relation is presented in figure 2.7.

2. *Porosity dependent permeability*
   A constitutive relationship between the permeability k and the porosity n has to be defined. In the literature there are only few approaches for such a relationship. A possible approximation for this function is given by the *Kozeny-Carman* equation (e. g. (Bear,

1972)) for granular media:

$$k = \frac{n^3}{(1-n)^2}\frac{1}{5M_S^2} \tag{2.93}$$

with the specific surface M_S of a porous material and the absolute permeability k. A description of the related physical background can be found in (Kozeny, 1927).

Incorporating this physical approach in the coupled finite element code, equation (2.93) is integrated and reformulated for the relative permeability $k_{\mathrm{rel,n}}$. With the porosity n and the initial porosity n_0 it results to

$$k_{\mathrm{rel,n}} = \frac{n^3}{(1-n)^2}\frac{(1-n_0)^2}{n_0^3}. \tag{2.94}$$

The relationship is presented in figure 2.7 for an initial porosity of 0.296. As it is pointed out, this relationship is derived for granular media. Comparing it with data given for other materials like claystone, the approach turned out to give satisfying results for the applications presented in this work.

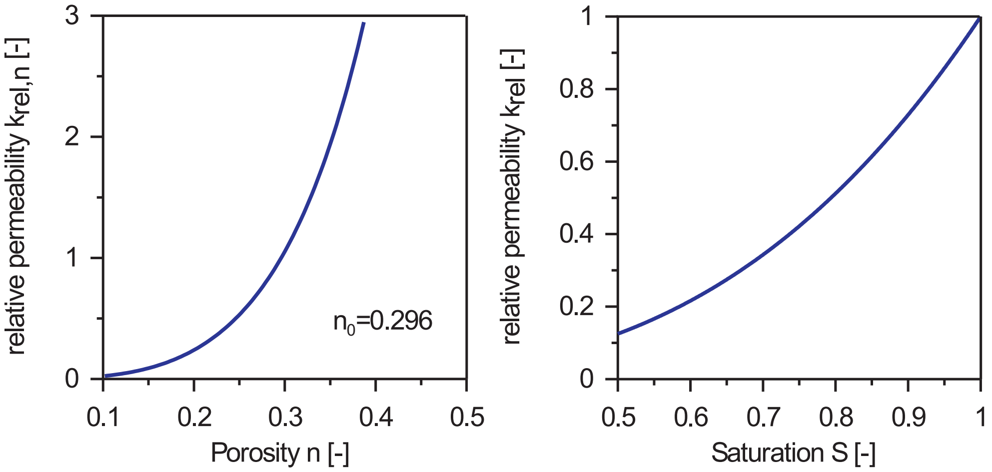

Figure 2.7: Relationship of permeabiliy and porosity (left) and of permeability and saturation (right).

The relative permeability depending on the water saturation and the porosity yields

$$k_{\mathrm{rel}} = k_{\mathrm{rel,S}} \cdot k_{\mathrm{rel,n}}. \tag{2.95}$$

2.4.7 Richards‘ approximation

By definition, the pore water pressure p for the unsaturated case results to

$$p = S^{\mathrm{w}} p^{\mathrm{w}} + S^{\mathrm{g}} p^{\mathrm{g}} \tag{2.96}$$

with the pore pressure of the water p^{w} and the gaseous phase p^{g}.

Richards proposed in 1931 an approximation for soil systems that are connected to the surface. It states that pressure changes in the gaseous phase can be neglected. Due to this approach the pressure of the gaseous phase is equal to the atmospheric pressure and assumed to be constant within the domain. This assumption leads to a direct dependency of the water saturation from the pore water pressure.

As a consequence, the differentiation between the saturated and the unsaturated case can be done by the comparison of the pore water pressure to the reference pressure, which is normally given by the atmospheric pressure. If the pore water pressure is below the reference pressure, it is called capillary pressure. The body is assumed to be partially saturated and the dependency of the capillary pressure and the saturation is given by a constitutive relation. If the pore water pressure is above the reference pressure, the body is fully saturated and the couplings due to the effective stress law, potentially extended by the Biot consolidation theory come into play for coupled hydraulic-mechanical problems.

To incorporate the impact of the compressibility of the matrix, the liquid and the gaseous phase to a purely hydraulic problem, the soil storativity may be introduced as it is done e.g. in (Thorenz, 2001).

2.5 The mathematical point of view

The formulation of the physical coupled hydraulic-mechanical problem is given in the previous chapters. As the remaining set of equations should be solved by a numerical method, it is important to investigate the applicability of the mathematical procedure to the existing physical problem. Consequently, the aim should be to define essential and sufficient conditions for the physical problem, which involve the existence and uniqueness of the numerical solution. More information concerning the mathematical point of view can also be found in (Simo & Hughes, 1998), (Stein & Barthold, 1996), (Knabner & Angermann, 2003), (Starke, 2004) and (Starke, 2003) amongst others. As the coupled problem is stated by a partial differential equation, this chapter starts with a short introduction to this topic.

2.5.1 Partial differential equations

Partial differential equations are equations involving some partial derivatives of an unknown function $\mathbf{u}$ in several independent variables. An example is given in equation (2.56) with the local form of the mass balance. This type of equations has the common form for the local case

$$\partial_t S(\mathbf{u}) + \nabla \cdot (q(\mathbf{u})) = Q(u) \tag{2.97}$$

where the storage term S quantifies the change of mass, the fluxes are given by q (resulting from the convective and the diffusive fluxes or the displacement) and the source term yields Q. The unknown is given by $\mathbf{u}$ and pictures the displacements or the pressure gradient, respectively.

The conservation equation has to be supplemented by initial and boundary conditions which are introduced in section 5.1.4. Depending on the boundary conditions the problem can be divided in different types of problems. It is called *nonstationary problem* if the storage term $S \neq 0$, otherwise one have a *stationary problem*. Additionally, if the fluxes $\mathbf{q} = \mathbf{0}$, the boundary conditions are referred to as *homogeneous boundary conditions* otherwise as *nonhomogeneous boundary conditions*. Furthermore, if $\mathbf{q}$ does not depend linearly on $\mathbf{u}$, one have a *linear boundary condition* otherwise a *nonlinear boundary condition*.

These definitions lead to the following classification of the problems. *Boundary value problems (BVP)* are stationary problems and *initial-boundary value problems (IBVP)* have arbitrary boundary conditions combined with an initial condition.

Differential equations can be defined nonlinear (due to a nonlinear relationship of $S, q,$ and Q), quasilinear (if all derivatives of the highest order are linear), semilinear (if nonlinearities exist only in $\mathbf{u}$, but not in the derivatives) or linear (if $Q(\mathbf{u}) = -r\mathbf{u} + f$). If f is termed zero, the linear differential equation is termed *homogeneous*, otherwise *inhomogeneous*.

For the proposed geotechnical problems, the resulting partial differential equation is called *elliptic* if the eigenvalues are not zero and if all of them have the same sign. This yields for stationary boundary value problems e.g. subsurface flow or fully saturated porous medium with stationary hydraulic potential. The relating problems are called *linear elliptic BVP*. Concerning the deformation of solids, a linear elastic material behavior results in a *linear elliptic BVP*. In spite of that, these kind of problems might be complicated due to the nonlinearities if plasticity and nonlinear elasticity are included. This may lead to time-dependent problems.

If one eigenvalue is positive and the other one is negative a convection dominated problem is indicated. These problems are *elliptic* or *parabolic* close to the *hyperbolic* case. A problem is called parabolic if exactly one eigenvalue is equal to 0 as it may be the case for *nonstationary initial-boundary value problems*.

Besides that, the investigation of variably saturated porous medium, which is time-dependent and nonlinear, results in *nonlinear parabolic initial-boundary value problems*. The depth-averaged surface flow investigated by the so-called *shallow water equations* is also time-dependent and nonlinear but *shallow water equations* are rather *hyperbolic* than *parabolic* as there exists a strong direction dependence of the solution.

The following remarks are restricted to 2nd order problems as most of the geotechnical problems are of this order. The proposed equations have to be discretized in time and space as it is described in chapter 5.

2.5.2 Mathematical formulation of the classical boundary value problem (BVP)

The classical linear boundary value problem is given by the balance equation (2.64), the Cauchy theorem (2.45) and the acquainted linear displacement boundary condition given by the displacements at a part of the boundary $\overline{\mathbf{u}}$. With the Hooke‘s law valid for the linear case (given in (2.80)) it yields

$$\begin{aligned}
\mathbf{0} &= \nabla \cdot (\lambda \,\mathrm{tr}\, \boldsymbol{\varepsilon}(\mathbf{u})\mathbf{1} + 2\mu\boldsymbol{\varepsilon}(\mathbf{u})) + \rho_{\mathrm{m}}\mathbf{g}. && \forall\ \mathbf{X}\,\epsilon\, B_0 && (2.98)\\
\overline{\mathbf{t}_0} &= (\lambda \,\mathrm{tr}\, \boldsymbol{\varepsilon}(\mathbf{u})\mathbf{1} + 2\mu\boldsymbol{\varepsilon}(\mathbf{u}))\,\mathbf{n} && \forall\ \mathbf{X}\,\epsilon\, \partial B_{0,\mathbf{t}} && (2.99)\\
\overline{\mathbf{u}} &= \mathbf{u} = 0 && \forall\ \mathbf{X}\,\epsilon\, \partial B_{0,\mathbf{u}}. && (2.100)
\end{aligned}$$

For further treatment, a bounded, open and connected subset $\Omega \subset \mathbb{R}^3$ with a sufficient smooth boundary Γ is considered. The boundary where the displacements are disabled is defined by $\Gamma_1 = \partial B_{0,\mathbf{u}}$ and the boundary where the surface tension acts is defined by $\Gamma_2 = \partial B_{0,\mathbf{t}}$. Consequently, it counts

$$\Gamma = \Gamma_1 \bigcup \Gamma_2 \quad \text{and} \quad \Gamma_1 \bigcap \Gamma_2 = \varnothing. \tag{2.101}$$

The initial configuration B_0 is than given by the closure $\bar{\Omega}$ of Ω. As it is defined previously, the points $\mathbf{X}$ of the initial configuration B_0 are termed $\mathbf{x}\,\epsilon\,\bar{\Omega}$.

Additionally, it is defined that:

$$\begin{aligned}
\mathbf{L}[\mathbf{u}(\mathbf{x})] &:= -\nabla \cdot (\lambda \,\mathrm{tr}\, \boldsymbol{\varepsilon}(\mathbf{u})\mathbf{1} + 2\mu\boldsymbol{\varepsilon}(\mathbf{u})) && (2.102)\\
\mathbf{B}[\mathbf{u}(\mathbf{x})] &:= (\lambda \,\mathrm{tr}\, \boldsymbol{\varepsilon}(\mathbf{u})\mathbf{1} + 2\mu\boldsymbol{\varepsilon}(\mathbf{u}))\,\mathbf{n} && (2.103)\\
\mathbf{f} &:= \rho_{\mathrm{m}}\mathbf{g} && (2.104)\\
\mathbf{g} &:= \overline{\mathbf{t}_0} && (2.105)
\end{aligned}$$

This leads to the following notation for the classical boundary value problem

$$\begin{aligned}
\mathbf{L}[\mathbf{u}(\mathbf{x})] &= \mathbf{f}(\mathbf{x}) && \text{in} && \Omega && (2.106)\\
\mathbf{u} &= \mathbf{0} && \text{at} && \Gamma_1 && (2.107)\\
\mathbf{B}[\mathbf{u}(\mathbf{x})] &= \mathbf{g}(\mathbf{x}) && \text{at} && \Gamma_2 && (2.108)
\end{aligned}$$

This BVP is defined in a reell vector space $\mathcal{C}$ with the scalar product

$$(\mathbf{u}, \mathbf{v}) := \int_{\Omega} \mathbf{u}(\mathbf{x}) \cdot \mathbf{v}(\mathbf{x})\, \mathrm{d}\mathbf{x} \qquad \mathbf{u}, \mathbf{v}\,\epsilon\,\mathcal{C}(\bar{\Omega}) \tag{2.109}$$

It can be shown, that this BVP has a unique solution as it is equivalent to a minimization problem. To mathematically proof the existence of a solution, the linear BVP has to be reformulated to a weak form.

2.5.3 The weak form

As a consequence of the weak formulation the requirements on the problem and the solution decrease. Physically this step is justified by the approach of the principle of the virtual work. Strictly speaking this is not the same as the weak form, as the requirements on the test functions are not the same than the requirements on the virtual displacements (the virtual displacements have to be infinitesimal small, the test functions are not restricted in that way). In spite of that difference, it is the common way to modify the problem in the proposed manner.

For the mathematical problem that means that, while there must exist continuous strong derivations for the strong formulation, the weak form only demands the existence of the integrals. This is given if the problem is square integrable within the sense of the *Lebesgue Integral* (please refer to appendix A.8), what means that there exists a convergence of a sequence of simple functions.

One resulting requirement for the weak form is the formulation of the given equations (2.106), (2.107) and (2.108) with functions being elements of an appropriate Hilbert space V, instead of only sufficient continuous functions. This means that instead of $\mathbf{u}, \mathbf{f}, \mathbf{g} \,\epsilon\, \mathcal{C}^2(\overline{\Omega})$ it yields $\mathbf{u}, \mathbf{f}, \mathbf{g} \,\epsilon\, \mathrm{V}$ where V is an appropriate Hilbert space with an appropriate scalar product. More information on the preconditions of this space can be found in section 2.5.4.

Introducing an arbitrary test function $\mathbf{v} \,\epsilon\, \mathrm{V}$ results in

$$(\mathbf{L}(\mathbf{u}), \mathbf{v}) - (\mathbf{f}, \mathbf{v}) = 0. \tag{2.110}$$

which can be paraphrased to the weak form of the BVP

$$\int_\Omega [\boldsymbol{\sigma}_{\mathrm{eff}}(\mathbf{u}) : \boldsymbol{\varepsilon}(\mathbf{v})] \,\mathrm{d}x - \int_\Omega \mathbf{f} \cdot \mathbf{v} \,\mathrm{d}x - \int_{\Gamma_2} \mathbf{g} \cdot \mathbf{v} \,\mathrm{d}s = 0 \tag{2.111}$$

by usage of the scalar product, the Gauss' integral theorem and the boundary conditions. To assure, that the strain energy function remains finite for arbitrary test functions $\mathbf{v}$, it has to hold that $\mathbf{v} \,\epsilon\, \mathrm{H}_0^1(\bar{\Omega})$ with the Hilbert space H_0^1.

Summarizing this leads to the theorem given in Box 2.1.

2.5.4 Investigating the weak form

Considering the common variational problem (pictured in box 2.2) the evidence of the existence, the uniqueness and the stability of the weak form in an adequate Hilbert space is given by the conditions of the *Lax-Milgram-Lemma* given in box 2.3.

Within this context, the uniqueness of the solution and the continuous dependency of the solution and the problem can be shown with additional usage of the V-ellipticity of $a(\mathbf{u}, \mathbf{v})$ and the continuity of $\mathbf{F}$. Furthermore, applying the *description sentence of Rieszsch* leads to the existence of the solution. Another important property of the solution is the regularity. This means that the solution of the weak formulation exhibit adequate differentiability to be a solution for the strong form of the classical BVP. This point can be investigated using the *embedding theorem of Sobolev* and observing the behavior of the function $\mathbf{u}$ on the boundary Γ.

Additionally, some preconditions for the *Hilbert* space and the *Lax-Milgram-Lemma* should be considered:

The determination of the solution $\mathbf{u}$ of the linear boundary value problem

$$\begin{aligned} \mathbf{L}[\mathbf{u}(\mathbf{x})] &= \mathbf{f}(\mathbf{x}) && \text{in} && \Omega && (2.112)\\ \mathbf{u} &= \mathbf{0} && \text{at} && \Gamma_1 && (2.113)\\ \mathbf{B}[\mathbf{u}(\mathbf{x})] &= \mathbf{g}(\mathbf{x}) && \text{at} && \Gamma_2 && (2.114) \end{aligned}$$

with $\mathbf{L}$ and $\mathbf{B}$ given in the equations (2.102) and following is formally equivalent to the solution of $\mathbf{u} \,\epsilon\, \mathrm{V}$ of the weak form

$$a(\mathbf{u}, \mathbf{v}) = \mathbf{F}(\mathbf{v}) \quad \forall\, \mathbf{v} \,\epsilon\, \mathrm{V} \tag{2.115}$$

with the bilinear form and the linear form respectively

$$\begin{aligned} a(\mathbf{u}, \mathbf{v}) &:= \int_\Omega \lambda(\text{tr}\,\boldsymbol{\varepsilon}(\mathbf{u})\text{tr}\,\boldsymbol{\varepsilon}(\mathbf{v})) + 2\mu\boldsymbol{\varepsilon}(\mathbf{u}) : \boldsymbol{\varepsilon}(\mathbf{v})\,\mathrm{d}x && (2.116)\\ \mathbf{F}(\mathbf{v}) &:= \int_\Omega \mathbf{f}\cdot\mathbf{v}\,\mathrm{d}x + \int_{\Gamma_2} \mathbf{g}\cdot\mathbf{v}\,\mathrm{d}s. && (2.117) \end{aligned}$$

V termed a space with sufficient smooth functions $\mathbf{u} : \mathrm{V} \rightarrow \mathbb{R}^3$, which vanishes on Γ_1.

Box 2.1: The linear boundary value problem (LBVP).

Determine an $\mathbf{u} \,\epsilon\, \mathrm{V}$, such that

$$a(\mathbf{u}, \mathbf{v}) = F(\mathbf{v}) \quad \forall \;\; \mathbf{v} \,\epsilon\, \mathrm{V}. \tag{2.118}$$

Box 2.2: The common variational problem.

Let $a(\mathbf{u}, \mathbf{v})$ be a continuous and V-elliptic bilinear form, which means that the constants $\alpha > 0$ and $M > 0$ exist so that

$$\begin{aligned} \mid a(\mathbf{u}, \mathbf{v}) \mid &\leq M \parallel \mathbf{u} \parallel_{\mathrm{V}} \parallel \mathbf{v} \parallel_{\mathrm{V}} && \forall \;\; \mathbf{u}, \mathbf{v} \,\epsilon\, \mathrm{V} && (2.119)\\ a(\mathbf{u}, \mathbf{u}) &\geq \alpha \parallel \mathbf{u} \parallel_{\mathrm{V}}^2 && \forall \;\; \mathbf{u} \,\epsilon\, \mathrm{V}. && (2.120) \end{aligned}$$

Additionally, let $\mathbf{F}$ be a continuous linear form at V. Than there exists exactly one solution $\mathbf{u} \,\epsilon\, \mathrm{V}$ of (2.118).

Box 2.3: *Lax-Milgram-Lemma.*

- $a(\mathbf{u},\mathbf{v})$ has to be a symmetric bilinear form

  Defining
  $$a(\mathbf{u},\mathbf{v}) := \frac{1}{2}\int_{\Omega} \boldsymbol{\sigma}_{\mathrm{eff}}(\mathbf{u}) : \boldsymbol{\varepsilon}(\mathbf{v})\,\mathrm{d}x \tag{2.121}$$
  with linear $\boldsymbol{\sigma}_{\mathrm{eff}}$ and $\boldsymbol{\varepsilon}$, incorporates the bilinear form of $a\,:\,\mathrm{V}\times\mathrm{V}\,\rightarrow\,\mathbb{R}^3$.

- $a(\mathbf{u},\mathbf{v})$ has to be a continuous, symmetric bilinear form

  The continuity of a is given in the *Hilbert* space V with the norm $\|\bullet\|_{\mathrm{V}}$ (defined in appendix A) if there exists a $M\,>\,0$, such that
  $$|\,a(\mathbf{u},\mathbf{v})\,| \leq M\,\|\,\mathbf{u}\,\|_{\mathrm{V}}\|\,\mathbf{v}\,\|_{\mathrm{V}} \qquad \forall\,\mathbf{u},\mathbf{v}\,\epsilon\,\mathrm{V}. \tag{2.122}$$
  This can be shown by usage of the bilinear form, the *Cauchy-Schwarz-inequality* and *Hooke‘ s law*. The proposed examination also announces the appropriate *Hilbert* space given in (2.123).

- V has to be an appropriate *Hilbert* space

  As explained above, the investigation of the continuity of the bilinear form leads to the appropriate *Hilbert* space:
  $$\mathrm{V} := \{\mathbf{v}\,\epsilon(H^1(\Omega))^3\,|\,\mathbf{v}\;=\;\mathbf{0}\,\mathrm{at}\,\Gamma\}. \tag{2.123}$$

- F has to be a continuous linear form

  With
  $$\mathbf{F}(\mathbf{v}) := \int_{\Omega} \mathbf{f}\cdot\mathbf{v}\,\mathrm{d}x + \int_{\Gamma_2} \mathbf{g}\cdot\mathbf{v}\,\mathrm{d}s \tag{2.124}$$
  this requirement directly results from the continuity of $\mathbf{f},\mathbf{v}$ and $\mathbf{g}$.

- $a(\mathbf{u},\mathbf{v})$ has to be V-elliptic

  The V-ellipticity implies that there exists a constant $\alpha\,>\,0$ such that
  $$a(\mathbf{u},\mathbf{u}) \geq \alpha\,\|\,\mathbf{u}\,\|^2_{\mathrm{V}} \qquad \forall\,\mathbf{u}\,\epsilon\,\mathrm{V}\,\subset\,(H^1(\Omega))^3. \tag{2.125}$$
  To show this, it is necessary to prove the equivalence of the half norm to the norm $\|\bullet\|_{1,\Omega}$ of the *Hilbert* space for every displacement $\mathbf{v}$ of the chosen *Hilbert* space $\mathrm{V} = (H^1(\Omega))^3$. This can be done applying the *inequality equation of Korn*.

Chapter 3

A non linear elastic compressibility model

Within the simulation of coupled geotechnical problems, the use of the well-known linear elastic material model, called Hooke‘s law, is widely spread. Nevertheless, some additional non linear effects have to be incorporated for various applications, e.g. the investigation of migration problems in mechanically loaded rocks with very low porosities and permeabilities.

Incorporating the nonlinearity due to the compressive behavior of the material influences the mechanical as well as the hydraulic subproblem. Particularly, the high compression of materials like dense smectite clays leads to a significant influence of the non linear compression behavior. This kind of materials is used for example for backfills or plugs of drifts, tunnels and shafts or for plugs in boreholes as well as in various fields of waste isolation (e.g. waste landfills). Because of the low initial porosities, also the compression behavior of host rocks like claystone used for high radioactive waste disposal is significantly influenced by the non linear compressibility.

Generally, one can state, that highly compressed materials as well as materials with a very low initial porosity have to be analyzed with an extended elastic model. Consequently, the work at hand presents an extension of the Hooke‘s law to a non linear elastic compressibility model.

This chapter starts with a short presentation of the general procedure for the derivation of constitutive material models. After that, it gives a short introduction to the linear elastic Hooke‘s law, before the non linear elastic compressibility model is introduced. Concerning this non linear theory, the physical background as well as relating definitions, the theory and requirements on the strain energy function are presented in a detailed way. Finally, the proposed model is validated by the comparison with experimental data found in the literature. Some applications are given in chapter 6 in section 6.1 and section 6.2.

3.1 General derivation of constitutive material models

The main feature of an elastic constitutive model is the existence of a reversibel and energy conserving deformation process, implicating the existence of an energy potential. Within the classical theory of elasticity, this fact is based on the existence of the so called *strain energy function* W. If an elastic body is loaded by specified displacements or forces, the resulting deformations imply a certain energy which is stored in the body. If the applied loads or specific displacements are removed, the energy will be recovered from the body. More information concerning the derivation of the elasticity theory can be found in (Davis & Selvadurai, 1996), (Haupt, 2002), (Zienkiewicz & Taylor, 2005) amongst others. For isothermal processes and perfectly elastic homogeneous materials producing no entropy, the strain energy function W related to the volume of the body as it is introduced in section 2.3.5 depends only on the strains and is given by

$$\dot{W} = \frac{\partial W}{\partial \mathbf{E}} : \dot{\mathbf{E}} \tag{3.1}$$

with the Green-Lagrange strain tensor E defined in section 2.2.3. Depending on the properties of the material like symmetry or compressibility, there exist various ways to constitute the strain energy function. An overview is presented in (Doll, 1998). The common definition of a strain energy function W for small deformations and linear elasticity leads to the Hooke's law

$$W = \frac{1}{2} \int_B \boldsymbol{\sigma} : \boldsymbol{\varepsilon} \, dV. \tag{3.2}$$

This energy function comprised the total elastic energy, stored in the body and equals the work of the external loads. The strain energy function on the representative volume element (RVE) remains

$$W = \frac{1}{2} \left(\boldsymbol{\sigma} : \boldsymbol{\varepsilon} \right) \tag{3.3}$$

and may be split into a deviatoric and a volumetric part

$$W = \frac{1}{2} \left[\left(\boldsymbol{\sigma}^{dev} + \frac{1}{3} \operatorname{tr} \boldsymbol{\sigma} \, \mathbf{1} \right) : \left(\boldsymbol{\varepsilon}^{dev} + \frac{1}{3} \operatorname{tr} \boldsymbol{\varepsilon} \mathbf{1} \right) \right]. \tag{3.4}$$

The stress field in the body is given by the derivative of the energy function with respect to the strains

$$\boldsymbol{\sigma} = \frac{\partial W}{\partial \boldsymbol{\varepsilon}}. \tag{3.5}$$

This coherence follows from the principle of the positive internal dissipation (2nd fundamental theorem of thermodynamics) which is presented in section 2.3.5 and implicates a constitutive relation of the stresses and the strains, depending on the energy potential.

The material matrix results from another differentiation and yields

$$\mathbb{C} = \frac{\partial^2 W}{\partial \boldsymbol{\varepsilon}^2} = \frac{\partial \boldsymbol{\sigma}}{\partial \boldsymbol{\varepsilon}}. \tag{3.6}$$

This leads to the incremental relation

$$\Delta \boldsymbol{\sigma} = \mathbb{C} \, \Delta \boldsymbol{\varepsilon}. \tag{3.7}$$

If the material matrix depends on the process variables, e.g. the existing strain field it is called non linear and is given by

$$\mathbb{C} = \mathbb{C}(\boldsymbol{\varepsilon}). \tag{3.8}$$

3.2 Linear elastic, compressible material

Assuming the strain energy function to be defined in the following way

$$W \;=\; \frac{1}{2}\boldsymbol{\varepsilon}\,\mathbb{C}\,\boldsymbol{\varepsilon} = \frac{1}{2}\lambda\,(\mathrm{tr}\,\boldsymbol{\varepsilon})^2 + \mu\boldsymbol{\varepsilon} : \boldsymbol{\varepsilon}, \tag{3.9}$$

the stresses, resulting from the derivative of the energy function to the strains, are given by

$$\frac{\partial W}{\partial \boldsymbol{\varepsilon}} = \boldsymbol{\sigma} = \lambda(\mathrm{tr}\,\boldsymbol{\varepsilon})\mathbf{1} + 2\mu\boldsymbol{\varepsilon}. \tag{3.10}$$

In this formulation λ and μ are the well-known Lamé parameter. This is the classical formulation for elastic materials and is already introduced in section 2.4.1 as the Hooke‘s law:

$$\boldsymbol{\sigma} = \mathbb{C} : \boldsymbol{\varepsilon} \tag{3.11}$$

Within this case, the material matrix $\mathbb{C}$ for isotropic material results to

$$\frac{\partial \boldsymbol{\sigma}}{\partial \boldsymbol{\varepsilon}} = \mathbb{C} = \lambda\mathbf{1} \otimes \mathbf{1} + 2\mu\mathsf{I} \tag{3.12}$$

or in matrix notation (with the definitions given in appendix A.1)

$$\mathbb{C} \;=\; \begin{pmatrix} \lambda+2\mu & \lambda & \lambda & 0 & 0 & 0 \\ \lambda & \lambda+2\mu & \lambda & 0 & 0 & 0 \\ \lambda & \lambda & \lambda+2\mu & 0 & 0 & 0 \\ 0 & 0 & 0 & 2\mu & 0 & 0 \\ 0 & 0 & 0 & 0 & 2\mu & 0 \\ 0 & 0 & 0 & 0 & 0 & 2\mu \end{pmatrix}. \tag{3.13}$$

3.3 Non linear elastic, compressible material

Assuming a linear elastic compressible model there is no limitation of the possible compaction of the material. Generally, the solid grains are presumed to be incompressible and the deformation only leads to a change of the porosity of the material. In spite of that, in many applications the incompressible state is not reached as most of the materials have relatively large porosities while the deformations are small. Applying this linear model to the prescribed materials with very low porosities, there is an important difference. In this case, even small volumetric deformations lead to a porosity near the compression point. At that point there is nearly no more pore space available and the material becomes incompressible.

To represent this situation with the theoretical model, a physically non linear elastic compressibility model which incorporates a compression point and restricts the porosity to the valid range has to be applied. Implementing this effect in the numerical model, an extension of the classical Hooke‘s law by an additional term is proposed as it is done by (Eipper, 1998) for the geometric non linear case. The modification for the geometric linear case, incorporating the initial state is described in the following. Due to the usage of a strain dependent permeability as it is presented in section 2.4.6 this effect also influences the hydraulic subproblem. The motivation for the development of a non linear elastic compressibility model for the geometric linear case is summarized in figure 3.1.

Various publications consider the effect of pore space and pore water pressure on the compressibility of the material. General remarks are given in (Davis & Selvadurai, 1996). Finally, there exist two common approaches to comprise this physical effect. On the one side, there exist purely mechanical models with a non linear elastic compressible approach (presented e.g. in (Eipper, 1998)). These models are used for geometric non linear problems with large deformations. On the other side, a common approach is the application of a bulk modulus depending on the pore space, the pore water pressure and the original bulk modulus of the material (given in (nagra-Opalinus, 2002) and others). This approach is used in various models and indicates an additional coupling of the hydraulic and the mechanical process.

To assure the clearness of the coupled model and to relate numerical coupling effects directly to physical processes, the work at hand treats the problem in a purely geometrical, mechanical way. The influence of the hydraulic process is already incorporated with Terzaghi‘s effective stress approach. Consequently, a purely mechanical approach is chosen. In this chapter, the physical as well as the theoretical background of the developed model are introduced. Afterwards, the mathematical and physical requirements are reviewed before the results are compared to experimental data found in the literature. The chapter finishes with some final remarks.

3.3.1 Physical background and relating definitions

Generally, in the theory of porous media, the material is composed of air, liquid and solid grains (see Chapter 2.1). While the air and the liquid are stored in the pore space of the body, the solid grains provide the material matrix. Assuming the solid grains to be incompressible, deformations only lead to a change of the pore space in the body. If the so called *compression point* is reached, there is no more pore space available and the material becomes incompressible. As a matter of fact, the investigation of materials with very small porosities may lead to incompressible material behavior already for deformations in the range of geometric linear material behavior. Consequently, a non linear elastic compressible material in the range of geometric linearity has to be defined. The material model has to fulfill the following requirements:

1. *The valid range should be the range of geometric linear deformations.*
2. *The low stress case should imply a material behavior similar to the behavior of* Hooke‘s *material.*
3. *The compression should be limited to the compression point. Convergence to this point should lead to a significant increase of the stresses.*

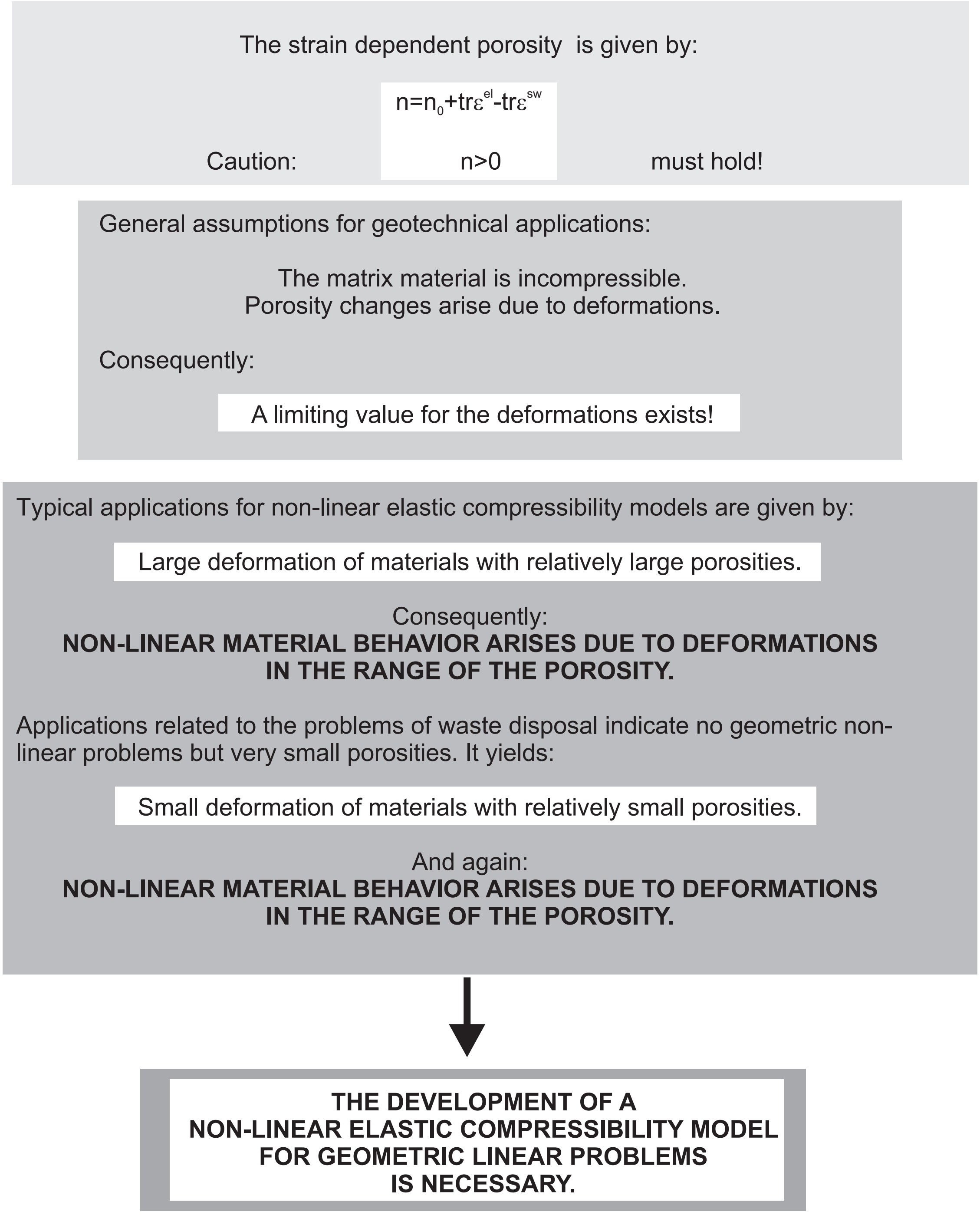

The strain dependent porosity is given by:

$n = n_0 + tr\varepsilon^{el} - tr\varepsilon^{sw}$

Caution: $n > 0$ must hold!

General assumptions for geotechnical applications:

The matrix material is incompressible.
Porosity changes arise due to deformations.

Consequently:

A limiting value for the deformations exists!

Typical applications for non-linear elastic compressibility models are given by:

Large deformation of materials with relatively large porosities.

Consequently:
NON-LINEAR MATERIAL BEHAVIOR ARISES DUE TO DEFORMATIONS IN THE RANGE OF THE POROSITY.

Applications related to the problems of waste disposal indicate no geometric nonlinear problems but very small porosities. It yields:

Small deformation of materials with relatively small porosities.

And again:
NON-LINEAR MATERIAL BEHAVIOR ARISES DUE TO DEFORMATIONS IN THE RANGE OF THE POROSITY.

THE DEVELOPMENT OF A NON-LINEAR ELASTIC COMPRESSIBILITY MODEL FOR GEOMETRIC LINEAR PROBLEMS IS NECESSARY.

Figure 3.1: Motivation for the development of the non linear elastic compressibility model for the geometric linear case.

An additional term of the strain energy function is given here to represent the mentioned material behavior. This term should modify the linear elastic case in the required way. As the behavior of the material significantly depends on the remaining pore space of the body, the function should depend on the porosity of the body. Therefore the porosity should be treated as a time-dependent material property. This is done by the proposed strain dependent porosity, which is already presented in section 2.4.4. Here the porosity is given by

$$n = n_0 + \operatorname{tr}\boldsymbol{\varepsilon} - \operatorname{tr}\boldsymbol{\varepsilon}^{\mathrm{sw}}. \tag{3.14}$$

As the material behavior is non linear, there must be a definition of an initial material behavior. This initial state should depend on the initial porosity of the material. To get a relation between the initial porosity and the initial stress conditions in the body, a difference between the initial and the stress-free porosity is made.

The stress-free porosity is the porosity of the material which indicates the beginning of elastic material behavior. It results from an unconstrained storage with no (sand-like materials) or only marginal (clay materials) compaction. It yields

$$n_{\mathrm{SF}} \quad = \quad n_{\sigma=0}. \tag{3.15}$$

The initial porosity is defined by

$$n_{\mathrm{IC}} = n_0 = n_{\mathrm{t=0}}. \tag{3.16}$$

The difference of both is given by

$$(\Delta n)_0 \equiv \Delta n = n_{\mathrm{IC}} - n_{\mathrm{SF}} \tag{3.17}$$

and presented in figure 3.2 for a material without preconsolidation and in figure 3.3 for a preconsolidated problem.

The strain field in the body is given by the elastic deformations due to the loads applied during the simulation time and the difference of stress-free and initial porosity Δn. The trace of the total strains results to

$$\begin{aligned} \operatorname{tr}\boldsymbol{\varepsilon}^{\mathrm{tot}} &= \operatorname{tr}\boldsymbol{\varepsilon}^{\mathrm{el}} + \operatorname{tr}\boldsymbol{\varepsilon}^{0} && (3.18)\\ &= \operatorname{tr}\boldsymbol{\varepsilon}^{\mathrm{el}} + \Delta n. && (3.19) \end{aligned}$$

3.3.2 Theoretical background of the non linear compressibility model for the geometric linear case

A strain energy function for the geometric non linear case is given by (Eipper, 1998). He proposed to extend the classical Hooke approach by the additional term W_{nlc} due to the non linear compressibility of the material

$$W = W_{\mathrm{Hooke}} + W_{\mathrm{nlc}} \tag{3.20}$$

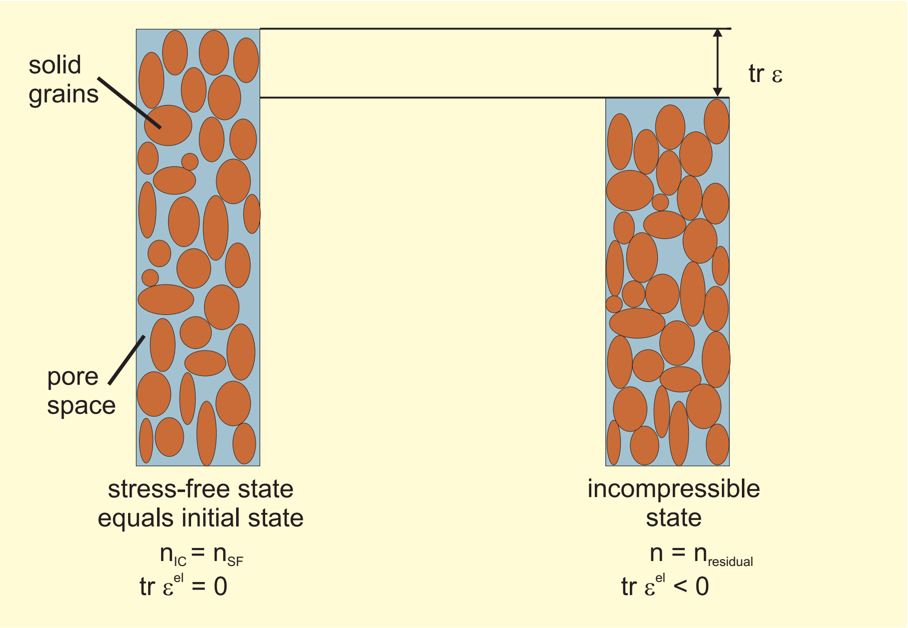

Figure 3.2: Physical model for the compression of porous media without preconsolidation.

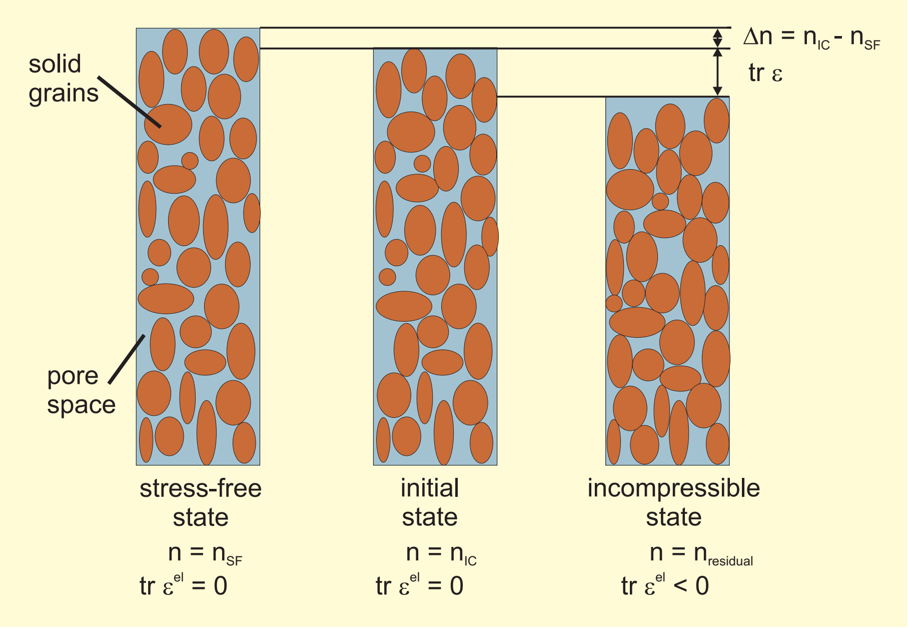

Figure 3.3: Physical model for the compression of porous media with preconsolidation.

with

$$W_{\mathrm{nlc}} = \frac{\lambda_{\mathrm{c}}}{\gamma\left(\gamma - 1 + \frac{1}{n_{\mathrm{SF}}^2}\right)} \left(J^{\gamma} - 1 - \gamma \ln \frac{J - (1 - n_{\mathrm{SF}})}{n_{\mathrm{SF}}} + \gamma (1 - n_{\mathrm{SF}}) \frac{J - 1}{n_{\mathrm{SF}}} \right). \quad (3.21)$$

With the Jacobian J and γ being a control parameter for the volumetric behavior. For the given applications, this parameter is set to $\gamma = 1$. Within the framework of the compressibility model, the common Lamé parameter λ is replaced by the compression parameter λ_c which is defined by

$$\lambda_\mathrm{c} = \frac{1}{2}\lambda. \tag{3.22}$$

The additional term of the strain energy function remains

$$W_\mathrm{nlc} = \frac{1}{2}\lambda n_\mathrm{SF}^2 \left(J - 1 - \ln\frac{(J - 1 + n_\mathrm{SF})}{n_\mathrm{SF}} + (1 - n_\mathrm{SF})\frac{J-1}{n_\mathrm{SF}} \right). \tag{3.23}$$

For geometric linearity, this term can be simplified by $J = \det \mathbf{F} = \mathrm{tr}\,\boldsymbol{\varepsilon}^\mathrm{el} + 1$. Consequently, the additional term of the strain energy function results to

$$W_\mathrm{nlc} = \frac{1}{2}\lambda n_\mathrm{SF}^2 \left(\mathrm{tr}\,\boldsymbol{\varepsilon}^\mathrm{el} - \ln\frac{(\mathrm{tr}\,\boldsymbol{\varepsilon}^\mathrm{el} + n_\mathrm{SF})}{n_\mathrm{SF}} + (1 - n_\mathrm{SF})\frac{\mathrm{tr}\,\boldsymbol{\varepsilon}^\mathrm{el}}{n_\mathrm{SF}} \right). \tag{3.24}$$

Incorporating this additional term to the classical linear approach, the total energy function remains

$$W = \frac{1}{2}\lambda \left[\frac{1}{2}(\mathrm{tr}\,\boldsymbol{\varepsilon}^\mathrm{el})^2 + n_\mathrm{SF}^2 \left(\mathrm{tr}\,\boldsymbol{\varepsilon}^\mathrm{el} - \ln\frac{(\mathrm{tr}\,\boldsymbol{\varepsilon}^\mathrm{el} + n_\mathrm{SF})}{n_\mathrm{SF}} + (1 - n_\mathrm{SF})\frac{\mathrm{tr}\,\boldsymbol{\varepsilon}^\mathrm{el}}{n_\mathrm{SF}} \right) \right] + \mu\boldsymbol{\varepsilon} : \boldsymbol{\varepsilon}. \tag{3.25}$$

Assuming the initial condition to be not necessarily equal to the stress-free condition, the total trace of strains results from equation $\mathrm{tr}\,\boldsymbol{\varepsilon}^\mathrm{tot} = \mathrm{tr}\,\boldsymbol{\varepsilon}^\mathrm{el} + \Delta n$ (given in equation (3.18)). For this case, the initial condition has to be incorporated in the strain energy function by using the total trace of strains $\mathrm{tr}\,\boldsymbol{\varepsilon}^\mathrm{tot}$ instead of $\mathrm{tr}\,\boldsymbol{\varepsilon}^\mathrm{el}$ for the compression term. The energy function yields to

$$\begin{aligned} W &= \frac{1}{2}\lambda \left[\frac{1}{2}(\mathrm{tr}\,\boldsymbol{\varepsilon}^\mathrm{el})^2 + n_\mathrm{SF}^2 \left(\mathrm{tr}\,\boldsymbol{\varepsilon}^\mathrm{tot} - \ln\frac{(\mathrm{tr}\,\boldsymbol{\varepsilon}^\mathrm{tot} + n_\mathrm{SF})}{n_\mathrm{SF}} + (1 - n_\mathrm{SF})\frac{\mathrm{tr}\,\boldsymbol{\varepsilon}^\mathrm{tot}}{n_\mathrm{SF}} \right) \right] + \mu\boldsymbol{\varepsilon} : \boldsymbol{\varepsilon} \\ &= \frac{1}{2}\lambda \left[\frac{1}{2}(\mathrm{tr}\,\boldsymbol{\varepsilon}^\mathrm{el})^2 + n_\mathrm{SF}^2 \left[\frac{\mathrm{tr}\,\boldsymbol{\varepsilon}^\mathrm{tot}}{n_\mathrm{SF}} - \ln\left(1 + \frac{\mathrm{tr}\,\boldsymbol{\varepsilon}^\mathrm{tot}}{n_\mathrm{SF}}\right) \right] \right] + \mu\boldsymbol{\varepsilon} : \boldsymbol{\varepsilon}. \end{aligned} \tag{3.26}$$

The derivation of stresses follows from differentiating with respect to the strains

$$\begin{aligned} \boldsymbol{\sigma} &= \frac{\partial W}{\partial \boldsymbol{\varepsilon}} \\ &= \frac{1}{2}\lambda \left[\mathrm{tr}\,\boldsymbol{\varepsilon}^\mathrm{el} + n_\mathrm{SF}\left(1 - \frac{n_\mathrm{SF}}{\mathrm{tr}\,\boldsymbol{\varepsilon}^\mathrm{el} + n_\mathrm{IC}}\right) \right] \mathbf{1} + 2\mu\boldsymbol{\varepsilon} \\ &= \frac{1}{2}\lambda \left[\mathrm{tr}\,\boldsymbol{\varepsilon}^\mathrm{el} + n_\mathrm{SF}\left(1 - \frac{n_\mathrm{SF}}{\mathrm{tr}\,\boldsymbol{\varepsilon}^\mathrm{tot} + n_\mathrm{SF}}\right) \right] \mathbf{1} + 2\mu\boldsymbol{\varepsilon}. \end{aligned} \tag{3.27}$$

Figure 3.4 shows the relation of stresses and $\mathrm{tr}\,\boldsymbol{\varepsilon}^\mathrm{tot}$. It can be seen that there exists an initial porosity which not necessarily equals the stress free porosity. The difference is given by Δn. Assuming the stress depending on the volumetric strains, the Δn is incorporated in the model as a kind of volumetric strain which is added to the elastic volumetric strains by the definition

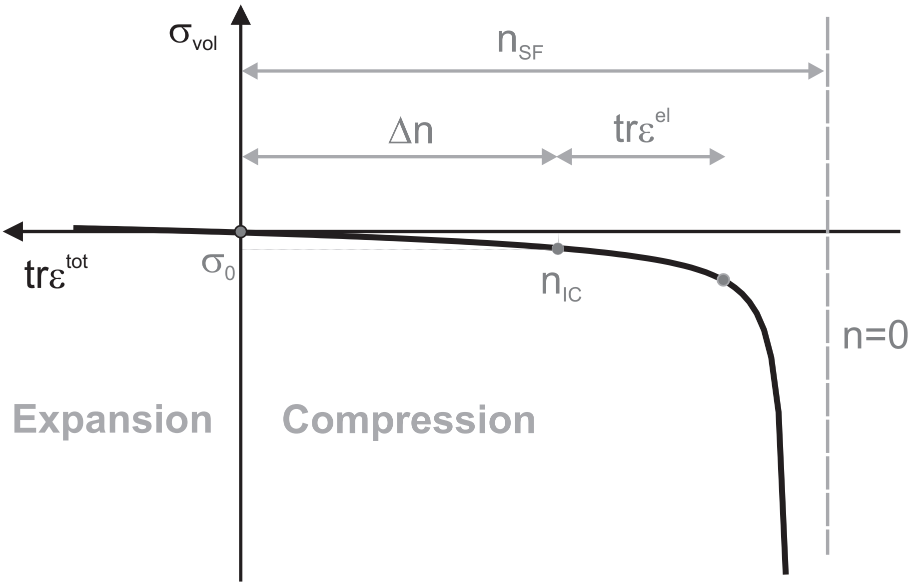

Figure 3.4: Nonlinear elastic compressible material model.

of tr $\varepsilon^{\mathrm{tot}}$. This incorporates some initial stresses to the model. The figure also shows that the given stress function leads to a significant increase of stresses in the compression area. This leads to limited strains in this range. Here the material converges to the incompressible state due to the lack of pore space.

Another differentiation leads to the material matrix

$$\begin{aligned}\mathbb{C}_{\mathrm{tang}} = \frac{\partial \boldsymbol{\sigma}}{\partial \boldsymbol{\varepsilon}} &= \frac{1}{2}\lambda\left(1+\frac{n_{\mathrm{SF}}^2}{(\mathrm{tr}\,\boldsymbol{\varepsilon}^{\mathrm{el}}+n_{\mathrm{IC}})^2}\right)\mathbf{1}\otimes\mathbf{1}+2\mu\mathbf{I}\\ &= \frac{1}{2}\lambda\left(1+\frac{n_{\mathrm{SF}}^2}{(\mathrm{tr}\,\boldsymbol{\varepsilon}^{\mathrm{tot}}+n_{\mathrm{SF}})^2}\right)\mathbf{1}\otimes\mathbf{1}+2\mu\mathbf{I}. \qquad (3.28)\end{aligned}$$

3.3.3 Requirements on the strain energy function

To prove the physical correctness of the proposed non linear compressibility model, the common procedure is given e.g. in (Eipper, 1998) or (Müllerschön, 2000). The following requirements have to hold.

1. The undeformed state has to be stress free. Consequently, for tr $\boldsymbol{\varepsilon}^{\mathrm{tot}} = 0.0$ and $n_{\mathrm{IC}} = n_{\mathrm{SF}}$ there exist no stresses. Resulting from equation (3.27), it yields

$$\frac{\partial W}{\partial \boldsymbol{\varepsilon}} = 0. \qquad (3.29)$$

   And consequently for W, defined in (3.26), it has to follow that

$$W = 0. \qquad (3.30)$$

2. A deformation to the compression point has to cause an infinite strain energy. This incorporates that the total strains in the negative range (compression behavior) converge to the stress free porosity $(\text{tr}\,\boldsymbol{\varepsilon}^{\text{tot}})^- \rightarrow n_{\text{SF}}$. Due to the last term this results in

$$W \rightarrow +\infty \tag{3.31}$$

   and for the stresses

$$\frac{\partial W}{\partial \boldsymbol{\varepsilon}} \rightarrow -\infty. \tag{3.32}$$

3. And finally a finite expansion given by $(\text{tr}\,\boldsymbol{\varepsilon}^{\text{tot}})^+ \rightarrow +\infty$ has to end up in a positively infinite strain energy function and infinite tension stresses. These requirements are fulfilled due to the classical linear term, while the additional term ends up with a limited value. For the strain energy function as well as for the stresses it holds:

$$W \rightarrow +\infty \tag{3.33}$$

$$\frac{\partial W}{\partial \boldsymbol{\varepsilon}} \rightarrow +\infty \tag{3.34}$$

4. The used material properties are compatible to the well known material properties λ and G. For the stress free case, the material matrix given in (3.28) equals the linear elastic material matrix derived by Hooke's law. The bulk modulus K results to

$$K = \frac{2}{3}G + \lambda. \tag{3.35}$$

5. The solution of the material model has to be unique, consequently the hydrostatic stress path has no extremum. It yields

$$\frac{\partial^2 W}{\partial \boldsymbol{\varepsilon}^2} \neq 0. \tag{3.36}$$

As all these requirements are fulfilled, the proposed material model seems to be mathematically correct. Further investigations are done using the material matrix to verify the physical outcomes.

3.3.4 Review of further physical requirements on the material matrix

As already stated in section 3.3.1 the material model has to fulfill some requirements. Some of them are already proven by the previous section. In spite of that, a short investigation concerning the material matrix given by

$$\frac{\partial \boldsymbol{\sigma}}{\partial \boldsymbol{\varepsilon}} = \frac{1}{2}\lambda\left(1 + \frac{n_{\text{SF}}^2}{(\text{tr}\,\boldsymbol{\varepsilon}^{\text{vol}} + n_{\text{SF}})^2}\right)\mathbf{1}\otimes\mathbf{1} + 2\mu\mathbf{I} \tag{3.37}$$

is done in this section. The essential term is the first one, the volumetric term, incorporating the compression behavior. The evolution of the multiplication factors within the brackets of this term is presented in figure 3.5. Within this representation, $n_{SF}^2/(\text{tr}\,\varepsilon^{\text{vol}} + n_{SF})^2$ is called the multiplication factor of the compressibility part and the constant value 1 is termed the multiplication factor of the linear part. The resulting factor is derived by the addition of both terms and is given by the green solid line in the figure 3.5. As can be seen here, the proposed model indicates residual porosities in the range of 20% of the stress free porosity n_{SF}. Although this value depends strongly on the material properties (please refer to section 3.3.5), this approximation is in the physically meaningful range (see section 3.3.5).

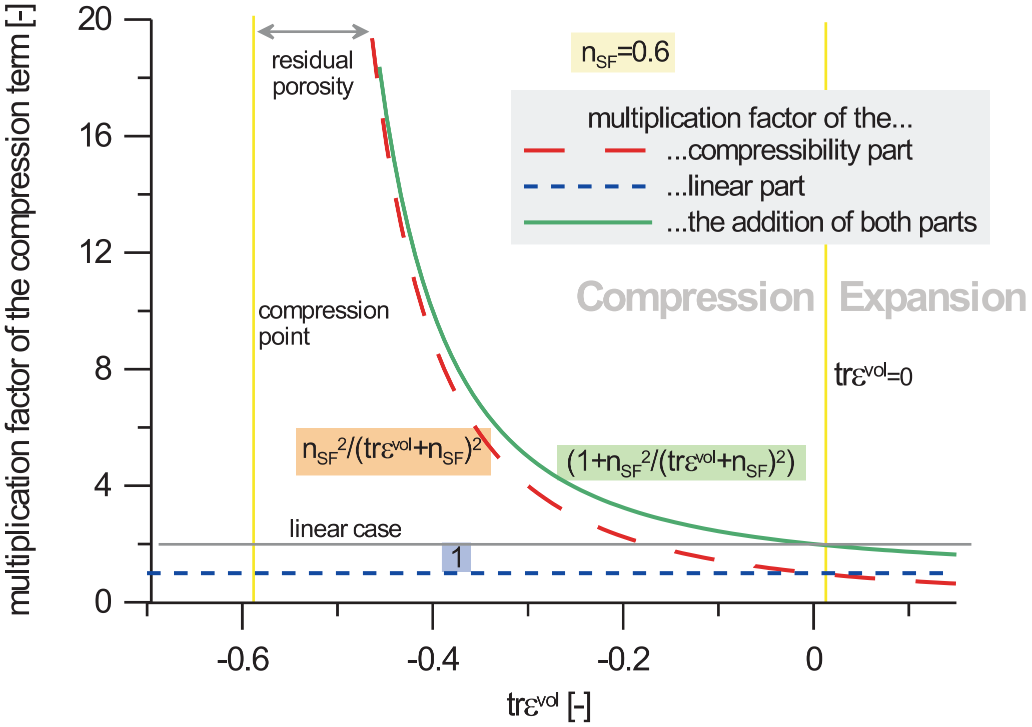

Figure 3.5: Multiplication factor of the volumetric term related to $\text{tr}\,\varepsilon^{\text{vol}}$.

The following requirements were given in section 3.3.1:

1. *The valid range should be the range of geometric linear deformations.*
   This is assured due to the presented derivation of the model.

2. *The low stress case should imply a material behavior similar to the behavior of Hooke's material.*
   This request is fulfilled as it yields

$$\frac{n_{\text{SF}}^2}{(\text{tr}\,\varepsilon^{\text{vol}} + n_{\text{SF}})^2} = 1 \tag{3.38}$$

for $\text{tr}\,\varepsilon^{\text{vol}} = 0$. Also figure 3.5 shows that the final multiplication factor, given by the green solid line equals the linear case for $\text{tr}\,\varepsilon^{\text{vol}} = 0$.

3. *The compression should be limited to the compression point. Convergence to this point should lead to a significant increase of the stresses.*
   A compression leads to significant compression strains given by negative values of $\operatorname{tr}\boldsymbol{\varepsilon}^{\mathrm{vol}}$ depicted by $(\operatorname{tr}\boldsymbol{\varepsilon}^{\mathrm{vol}})^{-}$. For
   $$(\operatorname{tr}\boldsymbol{\varepsilon}^{\mathrm{vol}})^{-} \rightarrow n_{\mathrm{SF}} \tag{3.39}$$
   it yields
   $$\frac{n_{\mathrm{SF}}^{2}}{(\operatorname{tr}\boldsymbol{\varepsilon}^{\mathrm{vol}} + n_{\mathrm{SF}})^{2}} \rightarrow \infty \tag{3.40}$$
   what incorporates the requested significant increase of the material matrix and consequently the stresses.

As a matter of fact, the requirements are fulfilled by the proposed model. But furthermore: What happens if the material is expanded? An expansion leads to strains pictured by $(\operatorname{tr}\boldsymbol{\varepsilon}^{\mathrm{vol}})^{+}$. Consequently it yields

$$\frac{n_{\mathrm{SF}}^{2}}{(\operatorname{tr}\boldsymbol{\varepsilon}^{\mathrm{vol}} + n_{\mathrm{SF}})^{2}} < 1 \tag{3.41}$$

and the material behaves softer than before (see figure 3.5). Physically, this is suggestive but there might be different approaches to handle this range of stresses. Depending on the exigencies of the physical model, there might be modifications of the proposed term or the insertion of other (additional) terms. Attention should be laid on the numerical robustness of the model, which will be imperiled for example by a singularity. For the geotechnical applications discussed in this work, the presented model is a useful approach.

3.3.5 Validation due to the comparison with experimental data found in the literature

Within this section various aspects of the proposed model should be validated due to the comparison with experimental data found in the literature. Here we do not focus on a specific material, because the general outcomes of the model are valid for various materials. In spite of that, a closer look on the curve progression indicates significant differences in the compression behavior of various materials. This will be one major part of the following investigations.

Additionally, an important attribute of the non linear elastic compressibility model is the residual porosity. As the material can not be compacted until the compression point is reached, the mathematical model should restrict the compression to this residual porosity, where the material indicates nearly incompressible behavior. Comparing various experimental data sets, one finally finds that this residual porosity also depends strongly on the material. As averaged value, a residual porosity of $\approx 20\%$ of the stress free porosity is supposed in the model. While this assumption underestimates the behavior of the salt grit presented in figure 3.6 marginally, it overestimates the data for smectite clays given in figure 3.7.

Oedometer tests carried out on salt grit of the Asse mine

The magnitude of the stresses is verified comparing the results with experimental data derived by *Oedometer tests*. These tests were carried out at the *Federal Institute for Geosciences and Natural Resources (BGR) in Germany, Hannover* and published in (Stührenberg, 2004).

The results of the proposed model in comparison with the experimental data is given in figure 3.6. The experimentally determined relationship between the void ratio e and the stress is given for different compaction velocities. Additionally, the stress as it results from the model approach depending on the void ratio e is given. The plottet simulation has been carried out with a stress free porosity assumed to be $n_{\mathrm{SF}} = 0.35$. It can be seen, that the approach of the non linear elastic compressibility model lies in the same magnitude as the experimental data. The curve progression as well as the remaining porosity fits the measured values quite good.

Furthermore, the experimental data indicates an influence of the compaction velocity. An increase of the compaction velocity leads to a damping of the non linear increase of stresses. As it can be seen, the numerical model fits the measured data very well for the highest and the lowest void ratio. Within this range, the model nearly pictures the curve derived for the lowest compaction velocity. This observance fits the physical background very well. The coupling of the proposed purely mechanical model with the hydraulic subproblem would also lead to a damping of the process due to the time-dependent pore water pressure. Depending on the hydraulic properties and the compaction velocity, the behavior found in the simulations will converge to the experimental data.

Oedometer tests carried out on highly compacted clays

The mechanical compaction of highly compacted clays is investigated in (Mondol, Bjorlykke, Jahren, & Hoeg, 2007). Within the mentioned publication, the results of this study are compared with various empirical approaches found in the literature (see figure 3.7). Additionally, a comparison with the curves given by the implemented non linear model (see figure 3.8) is carried out. Within (Mondol et al., 2007), the effective stresse is assumed to increase 1 MPa for every 100 m saturated depth. Consequently, the range of the stresses found in figure 3.7 lies between 0 and 50 MPa, what equals the range found in the previous example.

The experimental data is derived by oedometer tests which were carried out on saturated as well as on dry kaolinites, smectites and mixtures of both. These clays border the behavior of other types of clays, as smectite is the most fine-grained clay found in nature and kaolinite is the most coarse-grained one. Consequently, the kaolinite compacts much more than the smectite. The experimental results are presented by the black lines given in figure 3.7. They indicate a high non linear compression behavior in the low-stress area, a moderate nonlinearity between 2 and 20 MPa and a quasi-static state in greater depths. The observed behavior is assumed to be purely mechanical compaction behavior. It is interpreted as follows:

In the low-stress area, the dry clays initiate a first reorientation and rearrangement of solid particles. Additionally, the wet clays show rapid volume changes due to an interstitial water loss before the clay particles come into contact with each other. Within the second stage between 2 and 20 MPa the principle mechanism is particle rearrangement, which leads to a

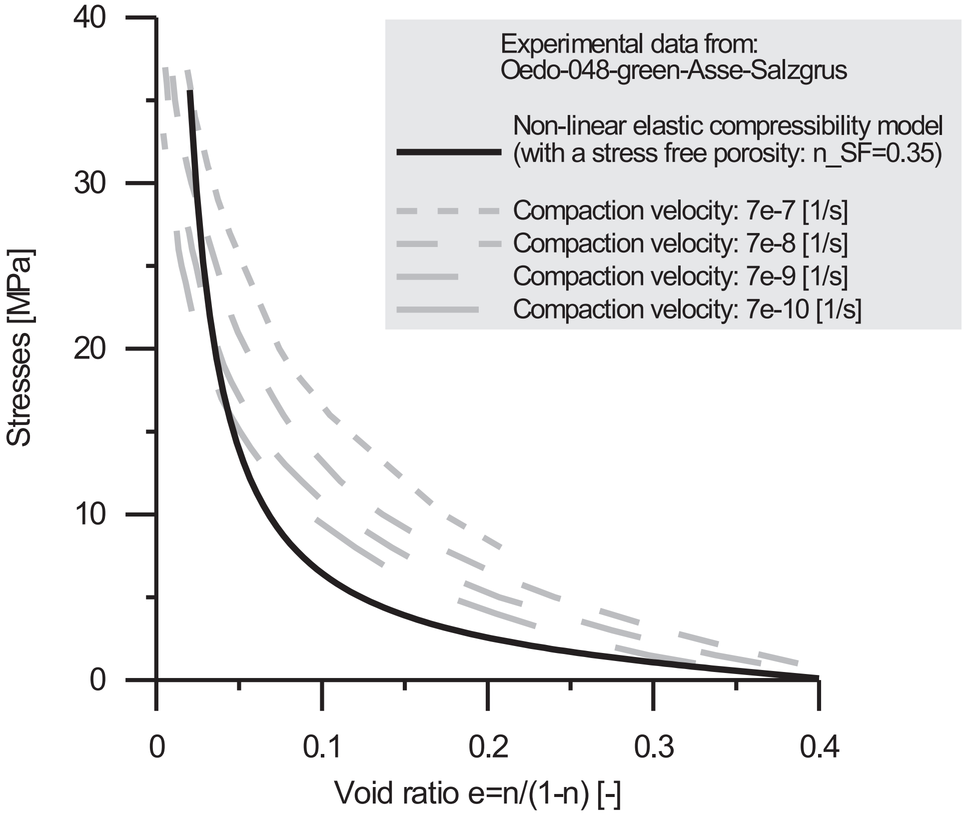

Figure 3.6: Relationship of stress and void ratio resulting from oedometer tests carried out on salt grit of the Asse mine.

closer grain-packing. At higher stresses the experiments indicate only very gradual changes of the porosity.

Comparing the experimental results (black lines) with various empirical approaches given by the grey lines in the same figure, two areas can be differentiated. For lower stresses, all empirical approaches show different behavior, but the experimental results lie clearly in the spanned range. For higher stresses, the empirical approaches indicate lower remaining porosities than the experimental results. The authors assume this difference to be a consequence of chemical compaction, that takes place in greater depths. This effect is not incorporated in their experiment.

Figure 3.8 presents the relation between stress and porosity of the proposed non linear model for various strengths and stress free porosities. The principal curve progression can be modeled. It depends strongly on the material properties, but all presented curves can be modeled due to the variation of strength and stress free porosity. Assuming a relatively high strength and a low stress free porosity leads to the curve, found in the experiments. Nevertheless, the highly non linear behavior at low stresses under ≈ 2 MPa can not be modeled, as the physical process pictured here is not part of the model approach. As the geotechnical applications presented in this work, deal with an at least marginal precompression, this evolution is not of significant interest in the given context.

Wetting and drying tests on compacted bentonite-sand mixtures

(Samingan, 2005) investigates the compression behavior of unsaturated, expansive materials due to suction changes. In this context wetting and drying tests under unconfined conditions are carried out on several heavily compacted specimens of a 50/50 bentonite-sand mixture. The influence of the suction on the void ratio is investigated. The results are presented in figure 3.9 and are similar to the curves given by the proposed non linear compressibility model. The remaining porosity is found to be $\approx 20\%$ of the stress free, initial porosity and the curve progression resembles the given curves. As this change of the void ratio is evoked by a physically completely different process (namely the increase of suction pressure), the non linear compression behavior seams to be independent from the process at least for these phenomenological effects.

3.3.6 Final remarks

An approach for a non linear elastic compressibility model for geometric linear problems is presented. Incorporating the initial state in the model, a difference between the stress free and the initial porosity is made (section 3.3.1). The derivation of the model is presented and afterwards the mathematical as well as the physical requirements were investigated. Finally, the model is verified due to the comparison with experimental data.

Summarizing this chapter, a purely mechanical model is developed to investigate the compression behavior of materials with very low porosities. Within this field of applications, the model pictures the behavior of a wide range of materials. It is verified for the compression state between very low negative stresses up to stresses close to the compression point.

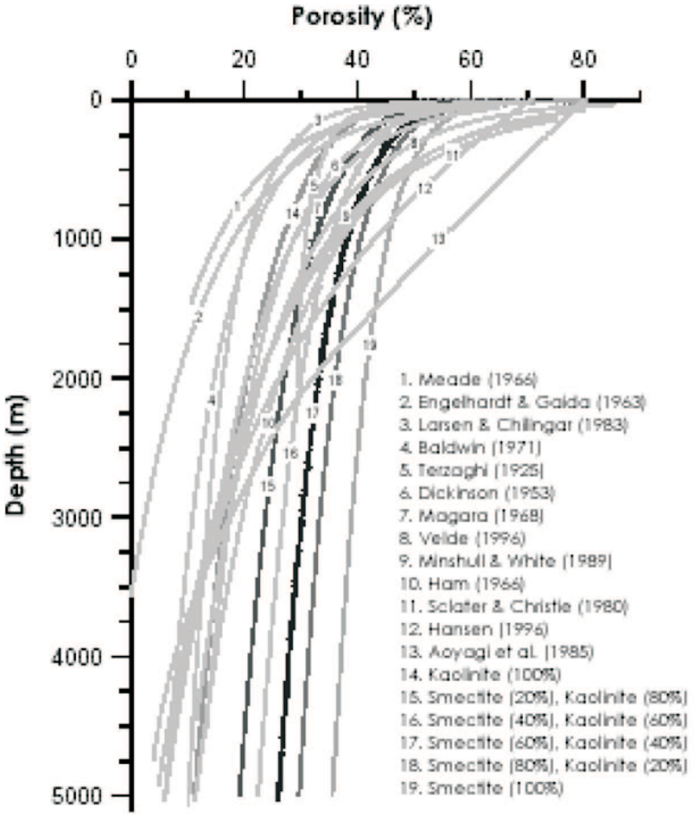

Figure 3.7: Depth versa porosity found in the experiments compared with empirical relations (please refer to (Mondol, Bjorlykke, J., & K., 2007)).

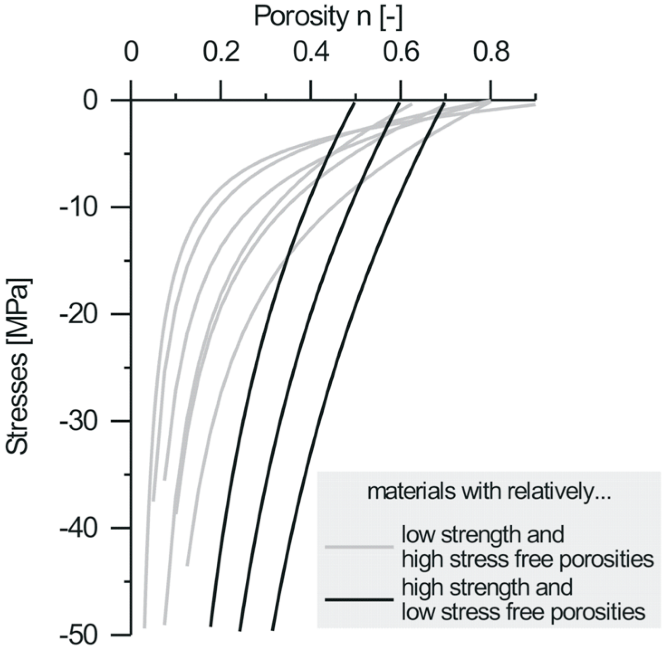

Figure 3.8: Relation of compression stress and porosity of the non linear elastic compressibility model for various strength and stress free porosities.

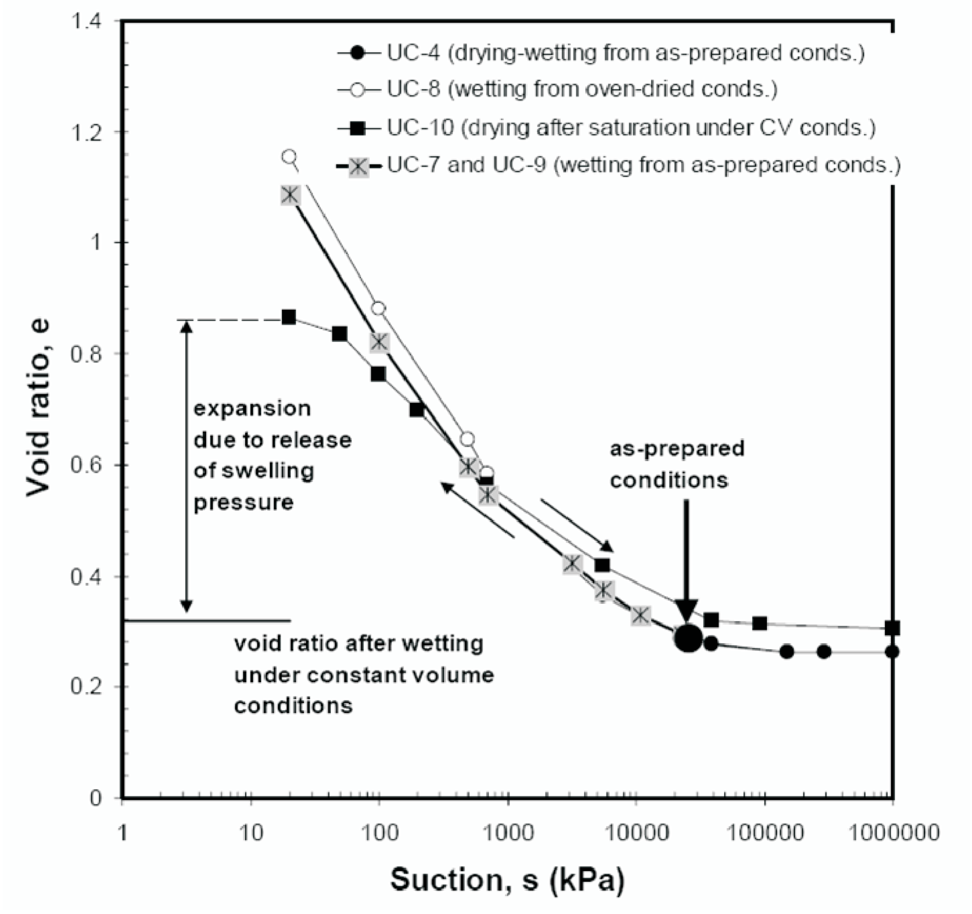

Figure 3.9: Influence of the suction on the void ratio of highly compacted bentonite-sand mixtures given in (Samingan, 2005).

Chapter 4

Elasto-plasticity with respect to clay modeling

Concerning structural engineering, one normally minimizes the appearance of plastic deformations in order to ensure the integrity of the entire structural system. In contrast to that, problems in geotechnics often imply plastic deformations that has to be considered in the design process in order to distinguish hardening from softening processes possibly causing global failure. Plastic deformations may lead to modifications of the material which affect the various coupled processes like mechanical, hydraulic, thermic or chemical effects. Consequently, accurate numerical simulations and comprehensive coupled models are required ensuring the coupling of manifold process variables and material properties.

The general idea of the common elasto-plastic material modeling is the partition of the stress space in two parts with elastic and plastic behavior, respectively. The classification is given by the so-called yield criterion, which may depend on material properties like the porosity or the saturation and on the history of loading. In the literature there exist various publications concerning different yield criteria and kinds of numerical treatment. A short introduction to this area is given here, for more information please refer to (Davis & Selvadurai, 2002), (de Boer, 2000), (Desai & Siriwardane, 1984), (Haupt, 2002), (Müllerschön, 2000), (Nackenhorst, 2003), (Panesso, 1998), (Simo & Hughes, 1998) or (Wriggers, 2001) amongst others.

As the history of elasto-plastic material modeling gives a good insight into the problems and the various extensions of simple plasticity models, this chapter starts with a historical review of plastic material modeling. Following this more physical reflection, the theoretical background is given in a generalized form. The chapter finishes by focusing on a plasticity model of the Cam-Clay type for which the theoretical background as well as the algorithmic formulation are presented.

4.1 Historical review of plastic material modeling

While there exist manifold publications concerning various types of elasto-plastic material modeling, a detailed summary on the history of material modeling is given in (de Boer, 2000).

In this work a short introduction is given, as this provides a good insight into the various effects, which have to be incorporated in such a model. The first investigations concerning the modeling of plastic effects were done in the area of metal research. Within this context von Mises (cyclic cylinder) as well as Tresca (hexagonal cylinder) presented a yield surface based on the derivations of Mohr, given by the well-known Mohr-circle at the end of the nineteenth century (see figure 4.1). These models imply only one parameter and may be used for brittle materials with a limitation in tensile stresses.

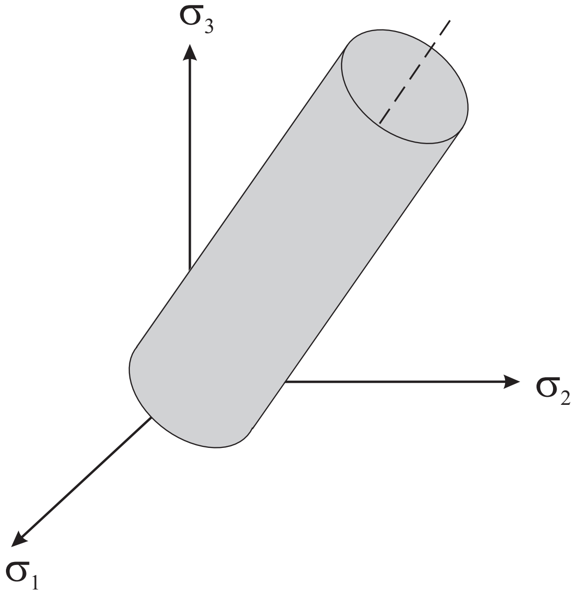

Figure 4.1: Von Mises plasticity (taken from (Davis & Selvadurai, 2002)).

In the geotechnical context, these material models can only be used for drained conditions without local increase in water pressure or suction. They are simple and numerically easy to handle but they do not suit multiphysical problems being addressed here. The most important shortcoming is that they do not relate the yield criterion on the hydrostatic pressure. To represent the cohesion of the geologic materials 2-parametric models have to be used which incorporate a dependence of the shear resistance to the hydrostatic pressure. These were presented by Drucker-Prager (conical yield surface in the principal stress space, please refer to (Drucker & Prager, 1952)) and Mohr-Coulomb (hexagonal conical yield surface in the principal stress space) and are depicted in figure 4.2 and compared in the deviatoric plane in figure 4.3.

These models are still the most widely used elasto-plastic material models. Comparing both, the Mohr-Coulomb model uses the well-known material parameters friction angle ϕ and cohesion c and shows a good approximation of many experimental results. But it implies numerical problems at points of discontinuity. While most of the discontinuities are avoided in the Drucker-Prager model, the circular shape of this model is contradictory to experimental results of cohesionless materials. Besides that, this model uses an approximation of the yield surface prescribed by the material parameters ϕ and c. Both of the presented models neglect failure due to hydrostatic loading and imply numerical problems at the tip of the cone. Con-

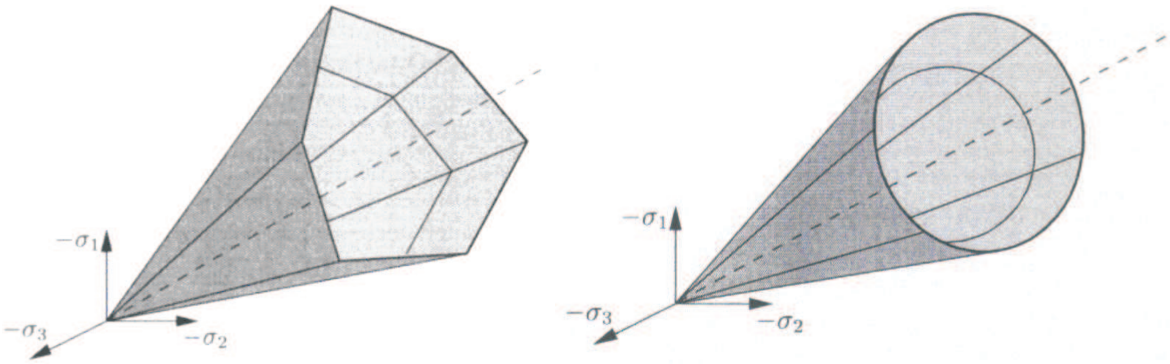

Figure 4.2: Mohr-Coulomb (left) and Drucker-Prager plasticity in the principal stress space (taken from (Davis & Selvadurai, 2002)).

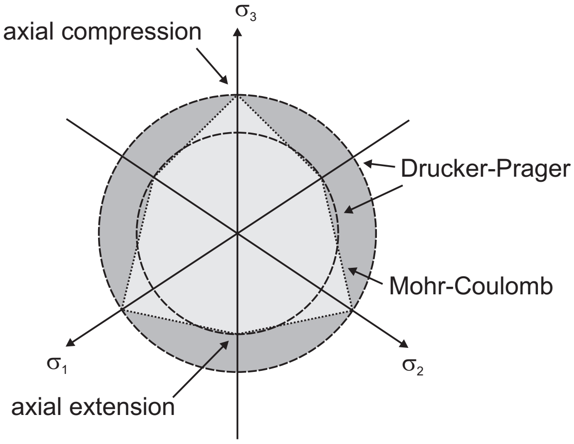

Figure 4.3: Comparison of the Mohr-Coulomb and the Drucker-Prager plasticity in the deviatoric plane.

cerning these models, the distinction between associative and non-associative flow rules, as it is explained later, is introduced in numerical plasticity modeling.

Extensions of the proposed 2-parametric models focus on different problems. In (Lade & Duncan, 1975) and (Matsuoka & Nakai, 1974) smoothed versions of the Mohr-Coulomb model are presented to avoid the numerical problems while retaining the established shape in the deviatoric plane. (Steinl, 2000) presents a yield surface with a hyperbolic shape, considering various compression and tensile strength.

Incorporating failure due to hydrostatic loading has been introduced in plastic material modeling by the so-called cap models namely the various Cambridge Clay Models: The Cam–Clay model presented in (Roscoe, Schofield, & Wroth, 1958), the Modified Cam–Clay model presented in (Roscoe & Burland, 1968), the Structured Cam–Clay model presented in (Liu & Carter, 2002) or the Simple Cyclic Loading Model presented in (Carter, Booker, & Wroth, 1982). The most common models of this type are the Original and the Modified Cam-Clay model, which are given in figure 4.4 in the p-q-space, which is introduced in A.6. More information on the Cambridge models is given in chapter 4.4 and a general description of a model of the Cam-Clay type is given in figure 4.5.

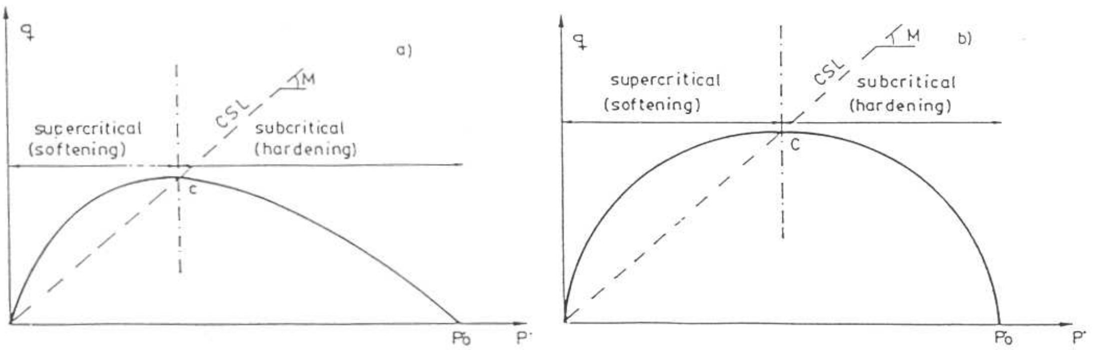

Figure 4.4: Original Cam–Clay–Model (left) and modified Cam–Clay–Model (right) in the p-q-plane (taken from (Desai & Siriwardane, 1984)).

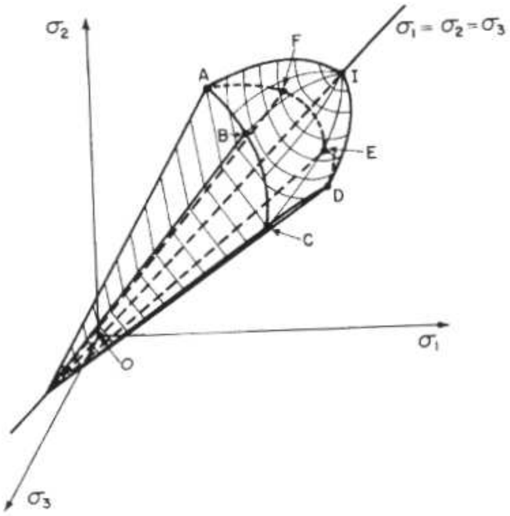

Figure 4.5: Plasticity model of the Cam-Clay type in the principal space (taken from (Desai & Siriwardane, 1984)).

In some of the plasticity models introduced here the cap is represented by an additional yield function which might lead to numerical problems at the intersection of both yield surfaces. Consequently, models with only one yield function has been established. Some of them are the HISS–Model (Hierarchical Single Surface Model) proposed by (Desai, 1989), the model by (Kim & Lade, 1988) and the models from (Ehlers, 1995) and (Findeiss, 2000) with their yield surfaces depicted in figure 4.6. These models avoid the numerical discontinuities but imply a great variety of material parameters, which are not known in many application cases.

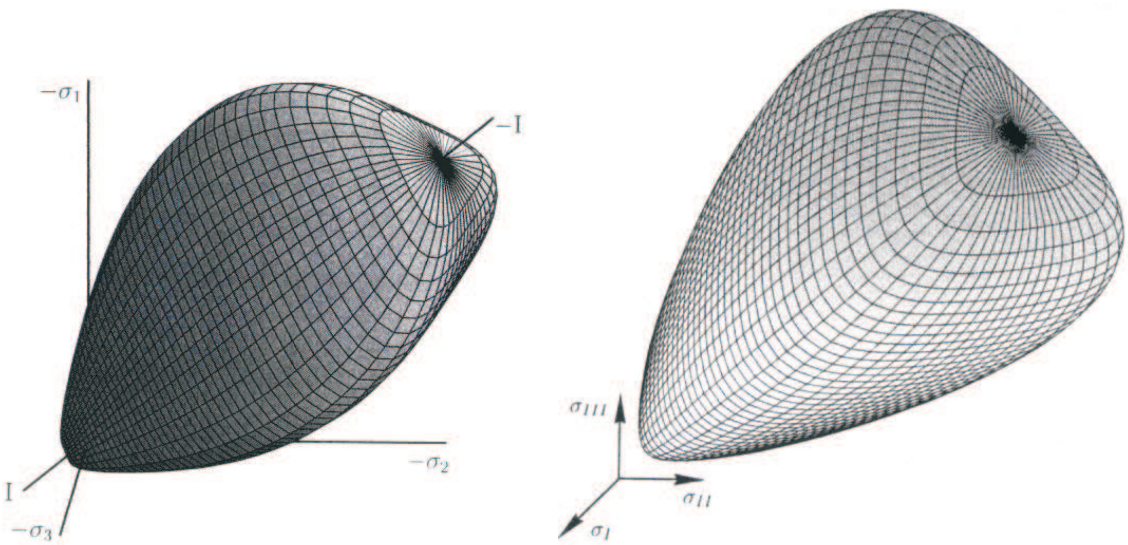

Figure 4.6: Models with a single yield function proposed by (Ehlers, 1995) and (Findeiß, 2000) presented in the principal space.

Current investigations concerning plastic material modeling are related to coupled problems. For example the Barcelona Basic Model (BBM) proposed by (Alonso, Gens, & Josa, 1990) or (Gens & Alonso, 1992), implies a saturation dependency of the yield function. In 1999 the same working group (Alonso, Vaunat, & Gens, 1999) suggested a model for the simulation of the mechanical behavior of expansive clays, called the Barcelona Expansive Model (BExM). Other approaches were presented by (Chen & Baladi, 1985), (Eekelen, 1980), or (Potts & Gens, 1984) amongst others.

4.2 Variable yield surfaces

The yield criterion may depend on various effects. The most important one is the hardening and softening of materials. These processes are incorporated in various plastic models with a so-called hardening law. Other effects like the influence of the pore space or the saturation to the yield function are not yet incorporated in standard plasticity modeling. The physical background of the proposed effects is briefly described in this chapter.

4.2.1 Hardening and softening

Various experiments show the influence of the load history on the material behavior. Besides, the yield surface depends on the preconsolidation of the material. These effects can be incorporated in the plastic model by applying a hardening law. There exist various approaches which might be classified to isotropic or kinematic hardening as it is explained below. Experimentally, this phenomenon is called the *Bauschinger effect*. In contrast to the perfect plastic model, shown in figure 4.7, the yield function may alter as it is presented in figure 4.8. Here, the left side demonstrates the isotropic hardening where the yield function increases due to a plastic load. In contrast to that, the picture on the right side illustrates the kinematical hardening, where a plastic load leads to a displacement of the yield surface. For this second case, the shape and the extent of the yield function remain constant. Typical evolutions of isotropic hardening and softening behavior occur in simulations of triaxial tests. Related results are presented in section 6.4.

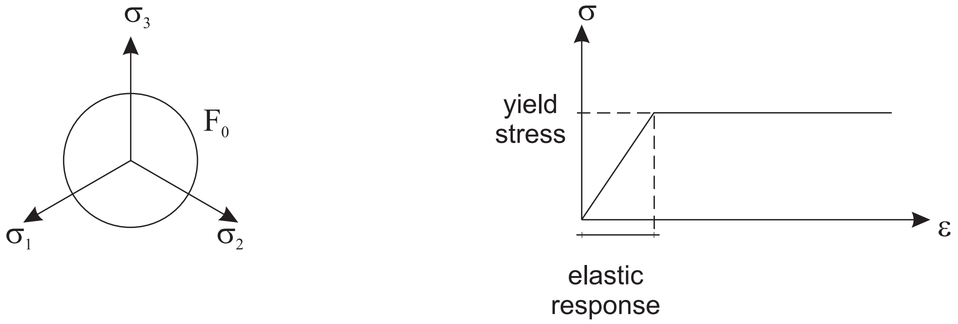

Figure 4.7: Perfect plasticity.

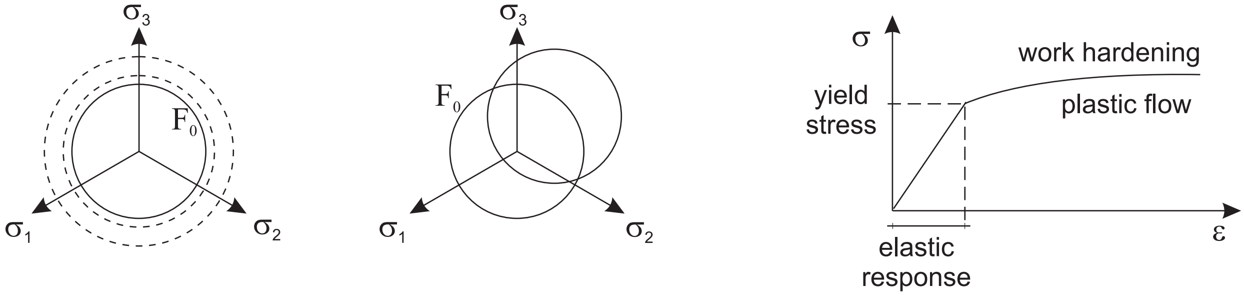

Figure 4.8: Hardening plasticity with isotropic (left) and kinematic hardening (right).

4.2.2 Dependency of the yield criterion on the pore volume

Various experimental results show the dependency of the yield criterion to the pore volume. It can easily be understood that a strongly compacted soil with a small porosity incorporates a larger elastic domain than an unconstrained one with a larger porosity. Up to now, there exist only few investigations concerning the influence of this physical effect on the plastic behavior. A model proposed by (nagra-Opalinus, 2002) is defined due to the pore volume e, resulting from

$$e = \frac{V_{\text{pores}}}{\text{V}_{\text{solid}}} = \frac{V_{\text{n}}}{V_{\text{s}}} \tag{4.1}$$

and is shown in figure 4.9.

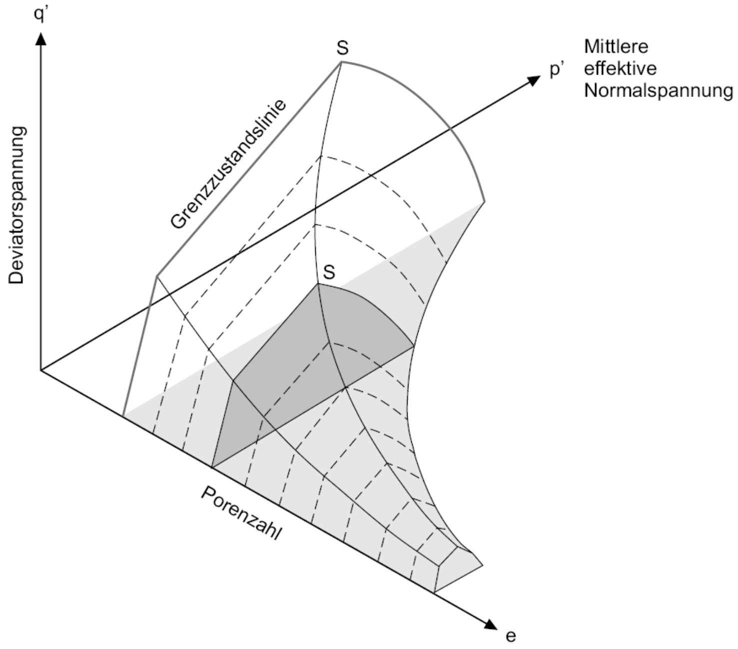

Figure 4.9: Porosity dependent yield function presented by (nagra-Opalinus, 2002). The yield surface is given in dependency on the void ratio e, the deviatoric stresses q‘ and the medial effective normal stresses p‘.

4.2.3 Dependency of the yield function on the saturation

Depending on the investigated material, the saturation might have a significant influence on the plastic behavior. While the incorporation of this effect seems not to be to important for example for granite, its influence should be tested especially for materials like salt or clay. A potential approach for this physical effect is given by (Gens, Jouanna, & Schrefler, 2002).

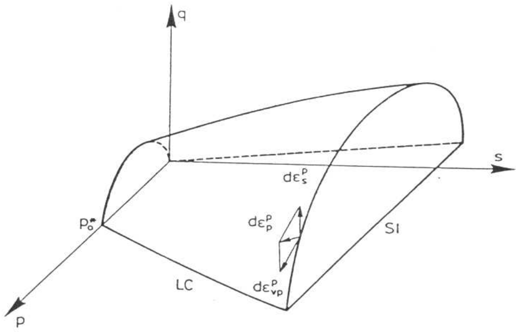

Figure 4.10: Saturation dependent plastic model presented by (Gens, Jouanna, & Schrefler, 2002). The yield surface is given in dependency on the suction s, the deviatoric stresses q and the medial effective normal stresses p.

4.3 Theoretical background of elasto-plastic material modeling

This chapter briefly reviews the main points of the theoretical background of plastic material modeling. For more information please refer to (Lewis & Schrefler, 2000), (Davis & Selvadurai, 2002), (Desai & Siriwardane, 1984), (Wriggers, 2001), (Nackenhorst, 2003), (Zienkiewicz & Taylor, 2005) or (Borja, Sama, & Sanz, 2003). As explained above, the stress space is divided in an elastic and a plastic part. Within the numerical procedure, a so-called trial state is defined, assuming the material to behave in an elastic way, without the appearance of plastic strains due to this load step. If this trial state ends up with a dissatisfying evaluation of the yield criterion, a return mapping is accomplished and finally the internal variables are adapted. Concerning this return mapping, there exist various flow rules, namely the associated and the non-associated one. For the loading and unloading conditions, the Kuhn-Tucker-conditions have to be mentioned. These topics will be shortly discussed within the following chapters.

4.3.1 Return mapping

Within the algorithmic formulation of the elasto-plastic model, the initial strains of each time step are assumed to result from the strains of the old time step and an additional increment due to the actual load step. Within this approach, the current incremental strain is assumed to result from a pure elastic behavior. The resulting state is called *„trial state"* and is not necessarily equal to a real state. The *„trial state"* is mathematically given by

$$\boldsymbol{\varepsilon}_{\mathrm{trial,n+1}} = \boldsymbol{\varepsilon}_{\mathrm{n}} + \Delta\boldsymbol{\varepsilon}_{\mathrm{n+1}} \qquad \lambda_{\mathrm{trial}} = 0. \tag{4.2}$$

The relating *„trial stresses"* result to

$$\boldsymbol{\sigma}_{\mathrm{trial,n+1}} = \boldsymbol{\sigma}_{\mathrm{n}} + \mathbb{C}^{\mathrm{el}}(\boldsymbol{\varepsilon}^{\mathrm{el}}_{\mathrm{n}}, \boldsymbol{\varepsilon}^{\mathrm{el}}_{\mathrm{trial,n+1}})\Delta\boldsymbol{\varepsilon}_{\mathrm{n+1}} \tag{4.3}$$

where the elastic material tensor $\mathbb{C}$ is split in a volumetric and a deviatoric part as follows to

$$\mathbb{C}^{\mathrm{el}} = \mathbb{C}^{\mathrm{el}}_{\mathrm{vol}} + \mathbb{C}^{\mathrm{el}}_{\mathrm{dev}}. \tag{4.4}$$

Within this approach, $\mathbb{C}^{\mathrm{el}}_{\mathrm{vol}}$ and $\mathbb{C}^{\mathrm{el}}_{\mathrm{dev}}$ are given by

$$\mathbb{C}^{\mathrm{el}}_{\mathrm{vol}} = K\,\mathbf{1}\otimes\mathbf{1} \tag{4.5}$$

$$\tag{4.6}$$

$$\mathbb{C}^{\mathrm{el}}_{\mathrm{dev}} = 2\mu(\mathbf{I} - \frac{1}{3}\mathbf{1}\otimes\mathbf{1}). \tag{4.7}$$

With this formulation, the elastic constitutive equation

$$\boldsymbol{\sigma} = \mathbb{C}^{\mathrm{el}} : \boldsymbol{\varepsilon} \tag{4.8}$$

can be reformulated with the hydrostatic pressure p and the deviatoric stresses $\mathbf{s}$ to

$$p^{\mathrm{trial}}_{\mathrm{n+1}} = p_{\mathrm{n}} + K\Delta\boldsymbol{\varepsilon}_{\mathrm{n+1}} : \mathbf{1} \tag{4.9}$$

$$\mathbf{s}^{\mathrm{trial}}_{\mathrm{n+1}} = \mathbf{s}_{\mathrm{n}} + 2\mu\Delta\boldsymbol{\varepsilon}^{\mathrm{dev}}_{\mathrm{n+1}} \tag{4.10}$$

for the „*trial state*". The hardening variables for this state are zero. The strains are given by an additive decomposition of the elastic and the plastic part

$$\Delta\boldsymbol{\varepsilon} = \Delta\boldsymbol{\varepsilon}^{\mathrm{el}} + \Delta\boldsymbol{\varepsilon}^{\mathrm{pl}}. \tag{4.11}$$

The plastic part of this equation can be derived by the incremental solution of the yield function for the plastic deformations:

$$\Delta\boldsymbol{\varepsilon}^{\mathrm{pl}} = \Delta\lambda \frac{\partial G(\boldsymbol{\sigma}_{\mathrm{n+1}}, \boldsymbol{\kappa})}{\partial \boldsymbol{\sigma}_{\mathrm{n+1}}} \tag{4.12}$$

with the plastic potential G and the internal variables $\boldsymbol{\kappa}$. An associative flow rule is defined by $\partial G/\partial\boldsymbol{\sigma} = \partial F/\partial\boldsymbol{\sigma}$ and is used in the following. Combining equation (4.3) and equation (4.12) yields

$$\begin{aligned} \boldsymbol{\sigma}_{\mathrm{n+1}} &= \boldsymbol{\sigma}^{\mathrm{trial}}_{\mathrm{n+1}} - \mathbb{C}^{\mathrm{el}} : \Delta\boldsymbol{\varepsilon}^{\mathrm{pl}}_{\mathrm{n+1}} && (4.13) \\ &= \boldsymbol{\sigma}^{\mathrm{trial}}_{\mathrm{n+1}} - \Delta\lambda_{\mathrm{n+1}}\mathbb{C}^{\mathrm{el}} : \boldsymbol{\varepsilon}^{\mathrm{pl}}_{\mathrm{n+1}}. && (4.14) \end{aligned}$$

The return mapping is carried out if the yield function $F(\boldsymbol{\sigma}_{\mathrm{trial}}, \boldsymbol{\kappa}) \leq 0$. It iteratively solves the system of equations until the final state is reached.

4.3.2 Loading and unloading conditions

The loading and unloading conditions are an additional requirement for the numerical solution of the elasto-plastic problem. They prove that the stresses are consistently at the yield surface and enable the appointment of the consistency parameter $\dot{\lambda}$ for the evolution equations. In the mathematical literature they are treated as a well-known optimization problem which is given by the Kuhn-Tucker conditions

$$\begin{aligned} \dot{\lambda} &\geq 0 && (4.15) \\ F(\boldsymbol{\sigma}; \boldsymbol{\kappa}) &\leq 0 && (4.16) \\ \dot{\lambda} F(\boldsymbol{\sigma}; \boldsymbol{\kappa}) &= 0. && (4.17) \end{aligned}$$

and the consistency requirement

$$\dot{\lambda}\dot{F}(\boldsymbol{\sigma}; \boldsymbol{\kappa}) = 0. \tag{4.18}$$

The investigation of these conditions leads to the following possible situations with the elastic domain given by $\mathbb{E}_{\boldsymbol{\sigma}}$

$$F < 0 \quad \Leftrightarrow \quad \boldsymbol{\sigma} \in \mathbb{E}_{\boldsymbol{\sigma}} \quad \Rightarrow \quad \dot{\lambda} = 0 \quad - \text{elastic} \tag{4.19}$$

$$F = 0 \quad \Leftrightarrow \quad \boldsymbol{\sigma} \in \partial\mathbb{E}_{\boldsymbol{\sigma}} \tag{4.20}$$

$$\begin{aligned} &\text{if} \quad \dot{F} < 0 \;\Rightarrow\; \dot{\lambda} = 0 \quad - \text{elastic unloading} \\ &\text{if} \quad \dot{F} = 0 \text{ and } \dot{\lambda} = 0 \quad - \text{neutral loading} \\ &\text{if} \quad \dot{F} = 0 \text{ and } \dot{\lambda} > 0 \quad - \text{plastic loading} \end{aligned}$$

4.4 A plastic model of the Cam-Clay type

One of the most widely used plasticity models for characterizing the stress-strain behavior of cohesive soils are the various models of the Cam-Clay type. The basics of this type of plasticity are given in (Roscoe & Burland, 1968). Other related publications are presented by (Potts & Zdravkovic, 2000), (Schofield & Wroth, 1968) or (Roscoe et al., 1958). The original model has been modified or extended in various ways as it is presented in (Borja & Kavazanjian, 1985), (Borja & Lee, 1990), (Panesso, 1998), (Gens et al., 2002), (Simo & Hughes, 1998) or (Ortiz & Pandolfib, 2004) amongst others. A detailed investigation of the influence of the input parameters in the context of the structured Cam-Clay model is given in (Liu & Carter, 2002). The presented models of the Cam-Clay type contain features such as hardening, softening and pressure sensitivity which are typical for cohesive soils. Additionally they require parameters which can be directly obtained from conventional laboratory tests. The Cam-Clay parameter M directly results from the well-known friction angle ϕ by the following relation:

$$M = \frac{6\sin\phi}{3-\sin\phi} \tag{4.21}$$

The maximum compression stress applied to the material is given by p_c and results directly from the history of the soil. λ_{VCI} and κ_{RCI} are usually determined from one-dimensional consolidation tests.

The Cam-Clay model applied in this work should be used within the context of the finite element method. Consequently a numerical integration for describing the incremental evolution of the stresses and the hardening parameters is carried out. The following description of the plastic model is based on the modified Cam-Clay model described in (Schofield & Wroth, 1968). More information about the implicit integration algorithm are given in (Borja & Lee, 1990). The presented model uses the same state boundary surface as yield and plastic potential surface (associated flow rule). It is described by an ellipses. The hardening rule is related only to plastic volumetric strains.

4.4.1 Basic equations of the proposed modified Cam-Clay model

The model is described in the p-q-space introduced in appendix A.6, where the volumetric stresses p and the deviatoric stresses q are defined by

$$p = \frac{1}{3}\,\mathrm{tr}\,\boldsymbol{\sigma} \tag{4.22}$$

$$q = \sqrt{\frac{3}{2}}\,\|\mathrm{s}\| \tag{4.23}$$

where $\boldsymbol{\sigma}$ is the Cauchy stress tensor and the deviatoric stress tensor s is given by

$$\mathrm{s} = \boldsymbol{\sigma} - \frac{1}{3}\,\mathrm{tr}\,\boldsymbol{\sigma}\mathbf{1} \tag{4.24}$$

with $\mathbf{1}$ being the second order identity tensor. The elliptic yield function of the modified Cam-Clay model is defined by

$$F = \frac{q^2}{M^2} + p(p - p_\mathrm{c}) \tag{4.25}$$

where M is the slope of the critical state line and p_c is the preconsolidation pressure, which gives the diameter of the ellipsoid in the direction of the p-axis.

Defining the current state of the material, the „over consolidation ratio“ *OCR* is introduced:

$$OCR = \frac{p_\mathrm{c,max}}{p_\mathrm{act}} \tag{4.26}$$

with the maximal pressure within the load history given by $p_\mathrm{c,max}$ and the current compression p_curr. The appellation „over consolidated“ follows directly from this definition to:

$$OCR = \frac{p_\mathrm{c,max}}{p_\mathrm{curr}} > 1 \tag{4.27}$$

And accordingly it follows the appellation „normally consolidated“:

$$OCR = \frac{p_\mathrm{c,max}}{p_\mathrm{curr}} \leq 1 \tag{4.28}$$

Additionally, the following hardening law, given here in the rate form, is used

$$\dot{p}_\mathrm{c} = \vartheta p_\mathrm{c} \dot{\boldsymbol{\varepsilon}}^\mathrm{pl}_\mathrm{vol} \tag{4.29}$$

$$\dot{\boldsymbol{\varepsilon}}^\mathrm{pl}_\mathrm{vol} = \mathrm{tr}\, \dot{\boldsymbol{\varepsilon}}^\mathrm{pl} \tag{4.30}$$

$$\vartheta = \frac{1 + e}{\lambda_\mathrm{VCI} - \kappa_\mathrm{RCI}} \tag{4.31}$$

where $\dot{\boldsymbol{\varepsilon}}^\mathrm{pl}_\mathrm{vol}$ is the plastic strain rate tensor, e is the void ratio of the soil mass, λ_VCI is the virgin compression index and κ_RCI is the recompression or swelling index. Both material parameters are constant and are usually determined by one-dimensional consolidation tests. While λ_VCI states the gradient of the „Virgo Consolidation Line“ *VCL*, κ_RCI is a measure for the gradient of the reconsolidation line. Both are depicted in figure 4.11. As the state variable e is assumed to be nearly constant within the context of the presented applications and for small time steps, the variable ϑ only varies very few within a time step. Consequently, the variables e and ϑ are treated explicitly, which means that they remain constant over a time interval and ϑ results to

$$\vartheta = \vartheta_n = \frac{1 + e_\mathrm{n}}{\lambda_\mathrm{VCI} - \kappa_\mathrm{RCI}}. \tag{4.32}$$

Within this publication an associative flow rule is assumed, defining the plastic flow by

$$\dot{\boldsymbol{\varepsilon}}^\mathrm{pl} = \dot{\phi} \frac{\partial F}{\partial \boldsymbol{\sigma}} \tag{4.33}$$

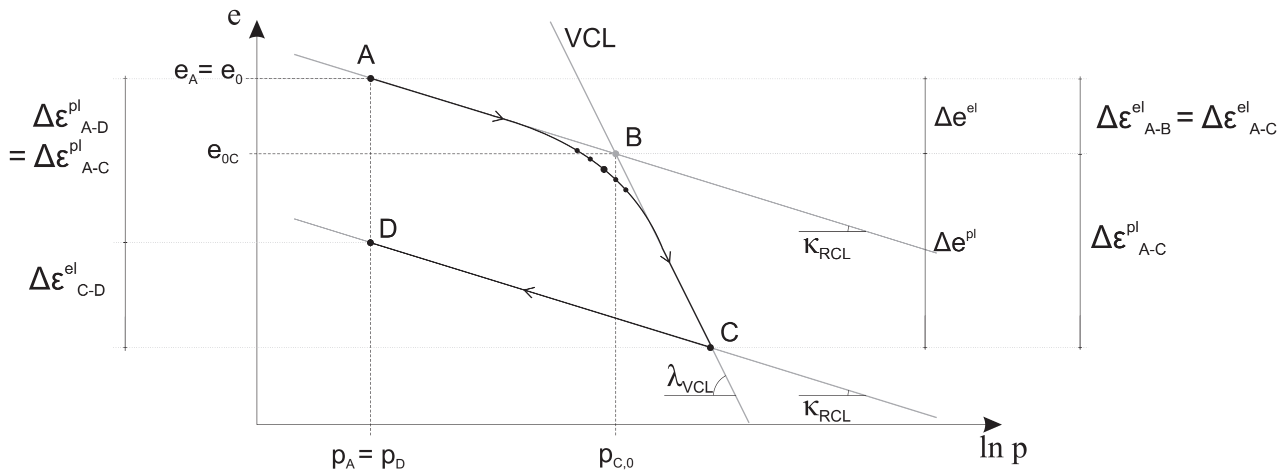

Figure 4.11: Hardening behavior due to virgo- and reconsolidation.

where $\dot{\phi}$ is the consistency parameter and the derivative of the yield condition can be derived by a direct application of the chain rule (see (Borja & Kavazanjian, 1985)):

$$\frac{\partial F}{\partial \boldsymbol{\sigma}} = \frac{\partial F}{\partial p}\frac{\partial p}{\partial \boldsymbol{\sigma}} + \frac{\partial F}{\partial q}\frac{\partial q}{\partial \boldsymbol{\sigma}} = \frac{1}{3}\frac{\partial F}{\partial p}\mathbf{1} + \sqrt{\frac{3}{2}}\frac{\partial F}{\partial q}\hat{\mathbf{n}} \tag{4.34}$$

where $\hat{\mathbf{n}} = \mathbf{s}/\|\mathbf{s}\|$. The derivatives of F, as defined in equation (4.25), with respect to p, q and p_{c} result to

$$\frac{\partial F}{\partial p} = 2p - p_{\mathrm{c}} \tag{4.35}$$

$$\frac{\partial F}{\partial q} = \frac{2q}{M^2} \tag{4.36}$$

$$\frac{\partial F}{\partial p_c} = -p. \tag{4.37}$$

(Borja & Lee, 1990) present two possibilities for the integration of the hardening parameter and the plastic strains. On the one side an analytical solution, on the other side the employment of the generalized trapezoidal method with respect to the variable p_{c}. Using the algorithmic integration over a time increment, one results in the incremental hardening law

$$p_{\mathrm{c,n+1}} = p_{\mathrm{c,n}} \exp \vartheta \Delta\varepsilon^{\mathrm{pl}}_{\mathrm{vol}} \tag{4.38}$$

where $p_{\mathrm{c,n}}$ is the preconsolidation pressure of the previous time step and $\Delta\varepsilon^{\mathrm{pl}}_{\mathrm{vol}} = \Delta\lambda\partial F/\partial p$.

In many classical variations of the Cam-Clay model the elastic moduli K and μ are state variables given by

$$K = \frac{1+e}{\kappa_{\mathrm{RCI}}}p \tag{4.39}$$

and

$$\mu = \frac{3K(1-2\nu)}{2(1+\nu)} \tag{4.40}$$

with the Poisson' s ratio ν. This approach is widely used but it is also discussed critical in current publications. The combination of elastic shear and bulk moduli may lead to a non-conservative model in which energy may be extracted due to loading cycles. Furthermore, the complexity of the proposed model in combination with the Cam-Clay theory of plastic behavior becomes obvious using a fully implicit Newton's method. The minor influence combined with a huge consumption of computer power can make such an approach unattractive for applications. In spite of the implicit method, an explicit treatment is proposed by (Borja & Lee, 1990) for the given nonlinearity. This means that

$$K = K_n = \frac{1+e_{\mathrm{n}}}{\kappa_{\mathrm{RCI}}} p_{\mathrm{n}} \tag{4.41}$$

and

$$\mu = \mu_{\mathrm{n}} = \frac{3K_{\mathrm{n}}(1-2\nu)}{2(1+\nu)}. \tag{4.42}$$

As the impact of this effect turns out to be small in various publications, the plastic model presented in this work neglects this effect.

4.4.2 Algorithmic formulation of the Cam-Clay model

The procedure for the numerical investigation of the elasto-plastic problem is given by the following:

1. *Start of the time step n+1*

   As explained above, the procedure for the investigation of the elasto-plastic problem starts with an elastic so-called *„trial state"*. The trial stresses are given by

$$p^{\mathrm{trial}} = \frac{1}{3} \operatorname{tr} \boldsymbol{\sigma}^{\mathrm{trial}} \tag{4.43}$$

   and

$$\begin{aligned} q^{\mathrm{trial}} &= \sqrt{\frac{3}{2}}\, \|\mathbf{s}^{\mathrm{trial}}\| \\ &= \sqrt{\frac{3}{2}}\, \|\mathbf{s}_n + 2\mu\Delta\boldsymbol{\varepsilon}^{\mathrm{dev}}_{\mathrm{n+1}}\| \end{aligned} \tag{4.44}$$

2. *Start of the iteration of $\Delta\lambda$ with the index k*

For the iteration of the variable $\Delta\lambda$ this item is the point of return, called

„START 1“

For further investigations concerning the elasto-plastic behavior, the yield function parameter F has to be determined by

$$F = \frac{q^2}{M^2} + p\,(p - p_\mathrm{c}) \tag{4.45}$$

where

$$p = p^\mathrm{trial} - K\Delta\lambda(2p - p_\mathrm{c}) \tag{4.46}$$

which can be reformulated to

$$p = \frac{p^\mathrm{trial} + \Delta\lambda K p_\mathrm{c}}{1 + 2\Delta\lambda K} \tag{4.47}$$

and

$$q = \frac{q^\mathrm{trial}}{1 + 6\mu\frac{\Delta\lambda}{M^2}} \tag{4.48}$$

$$p_c = p_\mathrm{c,n} e^{[\vartheta\Delta\lambda(2p - p_\mathrm{c})]}. \tag{4.49}$$

For the first iteration, the initial parameters yield

$$\Delta\lambda \;=\; 0 \tag{4.50}$$

and consequently

$$p = p^\mathrm{trial} \qquad q = q^\mathrm{trial} \qquad p_\mathrm{c} = p_\mathrm{c,n}. \tag{4.51}$$

For further iterations:

$$\Delta\lambda^\mathrm{k+1} = \Delta\lambda^\mathrm{k} - \frac{F^\mathrm{k}}{F'(\Delta\lambda)^\mathrm{k}} \tag{4.52}$$

The derivation of the yield function F to the consistency parameter $\Delta\lambda$ can be determined applying the chain rule

$$F'(\Delta\lambda) = \frac{\partial F}{\partial p}\frac{\partial p}{\partial\Delta\lambda} + \frac{\partial F}{\partial q}\frac{\partial q}{\partial\Delta\lambda} + \frac{\partial F}{\partial p_\mathrm{c}}\frac{\partial p_\mathrm{c}}{\partial\Delta\lambda} \tag{4.53}$$

which results in

$$\begin{aligned} F'(\Delta\lambda) \;&=\; -(2p - p_\mathrm{c})\left(K\frac{(2p - p_\mathrm{c})}{1 + (2K + \vartheta p_\mathrm{c})\Delta\lambda}\right) \\ &\quad -\frac{2q}{M^2}\frac{q}{(\Delta\lambda + \frac{M^2}{6\mu})} - \vartheta p p_\mathrm{c}\frac{(2p - p_\mathrm{c})}{1 + (2K + \vartheta p_\mathrm{c})\Delta\lambda}. \end{aligned} \tag{4.54}$$

The investigation whether the trial state is a real state or if further plastic deformations have to be investigated is done in the following way:
If:

$$F < 0 \tag{4.55}$$

The material behaves purely elastic or the plastic deformations are fit good due to the existing $\Delta\lambda$ for this time/load step. The final stress state can be calculated using equations (4.69), (4.70) and (4.71).
If:

$$F > 0 \tag{4.56}$$

Plastic deformations take place and are not yet pictured by the assumed $\Delta\lambda$. It is known that

$$\Delta\lambda \neq 0 \tag{4.57}$$

and a return mapping has to be carried out, iterating the variable $\Delta\lambda$.

3. *Start of the iteration of p_c with the index j*

For the iteration of the variable p_c this item is the point of return, called

„START 2“

Assuming $\Delta\lambda \neq 0$ the equation

$$F = \frac{q^2}{M^2} + p\,(p - p_\mathrm{c}) = f(\Delta\lambda, p^\mathrm{trial}, q^\mathrm{trial}, p_\mathrm{c}) \tag{4.58}$$

incorporates two unknowns, namely $\Delta\lambda$ and p_c. A sub-local Newton iteration is carried out to derive them.

From the definition of p_c given in equation (4.49) by the proposed hardening law and the derivation of p given in equation (4.47) the parameter $G(p_\mathrm{c})$ can be defined by

$$\begin{aligned} G(p_\mathrm{c}) &= p_{\mathrm{c,n}} e^{\left[\vartheta\Delta\lambda \frac{(2p^\mathrm{trial} - p_\mathrm{c})}{(1+2\Delta\lambda K)}\right]} - p_\mathrm{c} \\ &= f(p_\mathrm{c}, \Delta\lambda, p^\mathrm{trial}) \\ &\equiv 0. \end{aligned} \tag{4.59}$$

The investigation whether hardening or softening have to be investigated is done in the following way:
If:

$$G < 0 \tag{4.60}$$

no hardening occurs and

$$p_c = p_{\mathrm{c,n}}. \tag{4.61}$$

If:

$$G > 0 \tag{4.62}$$

hardening takes place and

$$p_{\mathrm{c}}^{\mathrm{j}+1} = p_{\mathrm{c}}^{\mathrm{j}} - \frac{G^{\mathrm{j}}}{G\,'(p_{\mathrm{c}})^{\mathrm{j}}} \tag{4.63}$$

with

$$G\,'(p_{\mathrm{c}}) = -\frac{\vartheta\Delta\lambda}{1+2\Delta\lambda K} p_{\mathrm{c,n}} e^{\vartheta\Delta\lambda\frac{2p^{\mathrm{trial}}-p_{\mathrm{c}}}{1+2\Delta\lambda K}} - 1. \tag{4.64}$$

Using equation (4.63) the variable p_c has to be updated and tested again:
If:

$$G > 0 \tag{4.65}$$

The proposed value for p_{c} has to be iterated furthermore. Start a new iteration at

„START 2“

If:

$$G < 0 \tag{4.66}$$

The iteration of p_{c} has finished. The yield function F has to be tested:
If:

$$F > 0 \tag{4.67}$$

The proposed value for $\Delta\lambda$ has to be iterated furthermore. Storage of the updated values of $\mathbf{n}, \Delta\lambda$ and $p_{\mathrm{c}}^{\mathrm{j}+1}$ and start of a new iteration at

„START 1“

If:

$$F < 0 \tag{4.68}$$

Exit. $\Delta\lambda$ and p_{c} are known and the final values for this time step might be calculated.

4. *Calculation of the final values for p, q, $p_{\rm c}$, $\boldsymbol{\varepsilon}^{\rm pl}$, tr$\boldsymbol{\varepsilon}^{\rm pl}$ and $\boldsymbol{\sigma}$*

The final values p, q and $p_{\rm c}$ for this time/load step result in:

$$p = p^{\rm trial} - K\Delta\lambda(2p^{\rm trial} - p_{\rm c}) \tag{4.69}$$

$$q = \frac{q^{\rm trial}}{1 + 6\mu\frac{\Delta\lambda}{M^2}} \tag{4.70}$$

$$p_{\rm c} = p_{\rm c,n}e^{\left[\vartheta\Delta\lambda(2p^{\rm trial} - p_{\rm c})\right]} \tag{4.71}$$

The plastic strains $\boldsymbol{\varepsilon}^{\rm pl}$ can be derived by:

$$\Delta\varepsilon^{pl}_{\rm n+1} = \Delta\lambda\frac{\partial F_{\rm n+1}}{\partial\sigma_{\rm n+1}} \tag{4.72}$$

with:

$$\frac{\partial F_{\rm n+1}}{\partial\sigma_{\rm n+1}} = \frac{\partial F}{\partial p}\frac{\partial p}{\partial\sigma} + \frac{\partial F}{\partial q}\frac{\partial q}{\partial\sigma} = \frac{1}{3}(2p - p_{\rm c})\mathbf{1} + \sqrt{\frac{3}{2}}\frac{2q}{M^2}\,\hat{\mathbf{n}} \tag{4.73}$$

The trace of the plastic strains tr$\,\boldsymbol{\varepsilon}^{\rm pl}$ yields:

$$tr\boldsymbol{\varepsilon}^{\rm pl}_{\rm n+1} = tr\boldsymbol{\varepsilon}^{\rm pl}_{\rm n} + 3\Delta\lambda\frac{1}{3}(2p - p_{\rm c}) \tag{4.74}$$

And the final stresses $\boldsymbol{\sigma}$ for this time/load step are:

$$\boldsymbol{\sigma} \;=\; p\,\mathbf{1} + q\sqrt{\frac{2}{3}}\,\hat{\mathbf{n}} \tag{4.75}$$

For a good convergence, the algorithmic consistent tangent modulus has to be used which is described in section 4.4.3.

4.4.3 Algorithmic consistent elasto-plastic tangent

In order to achieve a quadratic rate of convergence, the algorithmic consistent elasto-plastic tangent has to be used instead of the continuum elasto-plastic tangent. This can be done considering the incremental characteristic of the integration algorithm. More information on this topic can be found in (Wriggers, 1986), (Simo & Taylor, 1985) or (Simo & Hughes, 1998). The derivation of the algorithmic consistent tangent modulus for the presented model of the Cam-Clay type is given in (Borja & Lee, 1990) and results to:

$$\begin{aligned}\mathbb{C}_{CCM} = 2\mu\beta\,\mathbf{I} + [K(a_1 + a_2\,b_1) - \frac{1}{3}\,2\mu\,\beta]\,\mathbf{1}\otimes\mathbf{1} \\ +K(a_2\,b_2)\mathbf{1}\otimes\mathbf{n} + 2\mu\sqrt{\frac{2}{3}}\,a_6\,b_1\,\mathbf{n}\otimes\mathbf{1} \\ +2\mu(\sqrt{\frac{2}{3}}\,(a_5 + a_6\,b_2) - \beta)\mathbf{n}\otimes\mathbf{n}\end{aligned} \tag{4.76}$$

with the definitions of $\mathbf{I}$ and $\mathbf{1}$ given in appendix A.2 and A.3 and the variables

$$\beta = \frac{\|\mathbf{s}\|}{\|\mathbf{s}^{\mathrm{trial}}\|}, \tag{4.77}$$

$$a_1 = \frac{(1 + p_c\Delta\lambda)}{(1 + 2K\Delta\lambda + p_c\Delta\lambda)}, \tag{4.78}$$

$$a_2 = -\frac{(2p - p_c)}{(1 + 2K\Delta\lambda + p_c\Delta\lambda)}, \tag{4.79}$$

$$a_3 = \frac{2p_c\Delta\lambda}{(1 + 2K\Delta\lambda + p_c\Delta\lambda)}, \tag{4.80}$$

$$a_4 = \frac{p_c}{K}\frac{(2p - p_c)}{(1 + 2K\Delta\lambda + p_c\Delta\lambda)}, \tag{4.81}$$

$$a_5 = \sqrt{\frac{3}{2}}\left(1 + \frac{6\mu\Delta\lambda}{M^2}\right)^{-1}, \tag{4.82}$$

$$a_6 = -\frac{3q}{M^2}\left(1 + \frac{6\mu\Delta\lambda}{M^2}\right)^{-1}, \tag{4.83}$$

$$b_1 = -K\frac{\left[\left(a_3 - 2a_1\right)p + a_1 p_c\right]}{\left[-2\mu\frac{2q}{M^2}a_6 - K\left(2a_2 - a_4\right)p - a_2 p_c\right]} \tag{4.84}$$

and

$$b_2 = 2\mu\frac{2q}{M^2}\frac{a_5}{\left[-2\mu\frac{2q}{M^2}a_6 - K\left(2a_2 - a_4\right)p - a_2 p_c\right]}. \tag{4.85}$$

Chapter 5

Numerical Solution

For the numerical simulation of mechanical and hydraulic problems the finite element method is state of the art. It is proven to be a very robust and flexible method. Consequently, it is used for the numerical solution of the proposed problems. A short introduction is given in this chapter. Afterwards, the relating mathematical treatment as well as the usage of the finite element method for the derived balance equation are presented for the fully saturated case of a coupled hydraulic-mechanical problem in an elastic porous medium. Finally, some common solvers are presented and a short introduction into the FEM code RockFlow is given.

5.1 The Finite Element Method (FEM)

The finite element method is one of the most common numerical methods used for mechanical, hydraulic and coupled problems in the last years. Compared to other numerical tools, that approximate the solution of partial differential equations (PDEs), it turns out to be very useful. As a matter of fact, a great number of publications deal with this topic. Some of the most important ones are published by (Bathe, 1996), (Belytschko, Liu, & Moran, 2003), (Hughes, 2000), (Lewis & Schrefler, 2000), (Smith & Griffiths, 2004), (Wriggers, 2001) and (Zienkiewicz & Taylor, 2005).

5.1.1 Idea and concept

Analytical solutions of geotechnical problems are only known for very limited cases. Due to the geometrical and physical complexity most of the problems lead to mathematical problems that have to be handled with numerical tools. For a great variety of engineering problems, the finite element method turns out to be practicable. Consequently, this method is used within this publication and the essential steps for the mathematical treatment of the problem are summarized in the following:

Mathematical description of the physical problem. The physical problem, based on the balance relations combined with constitutive equations, has to be formulated using the theory of porous media and the kinematical relations presented in chapter 2.1. Within this publication the focus is put on geotechnical applications. These lead in most cases to partial differential equations as they are given for every subproblem in the strong form of equilibrium in chapter 2.3.

Formulation of the weak form. Combining the partial differential equations with constitutive models presented in chapter 2.4 and reformulating them in the way shown in chapter 5.2 leads to the weak form of the equilibrium.

Discretization of time and space. As the problem is solved element wise within different time steps, the geometry has to be meshed and the time has to be discretized. This is shown in chapters 5.1.2 and 5.1.3.

Formulation of the system of equations solved by the FEM. With respect to the chosen field variables (e.g. displacement and pressure), the field equations have to be interpolated by polynomial shape functions. Additionally, the system has to be assembled to a global algebraic system, incorporating the boundary conditions (*Dirichlet* type), which are introduced in section 5.1.4. This procedure is exemplarily shown in chapter 5.3 for the coupled HM-problem.

Solving of the system of equations. Due to various effects, a linear system of equations may imply nonlinearities. In most of the cases the mathematical problem can be solved by the combination of linear solvers with one of the nonlinear solvers presented in chapter 5.4.

5.1.2 Spatial discretization

Figure 5.1 shows an arbitrary body B on the left and a possible discretization of the geometry on the right.

Mathematically, the discretization is given by

$$B \simeq \bigcup_{e=1}^{n_e} \Omega_e \tag{5.1}$$

where the spatial domain B is approximated by n_e non overlapping finite elements Ω_e. The weak form of equilibrium is solved element wise before the system of equations is assembled to a global algebraic system. Within the elements the chosen field variables (in most of the cases the deformation and the pressure) are approximated by the same shape functions as the geometry - this is called *isoparametric* approach (see chapter 5.3).

5.1.3 Temporal discretization

For the temporal discretization, finite difference methods (FDM) are used. The temporal derivative of the unknown $\mathbf{u}$ for the time steps n and $n+1$ can be approximated by the

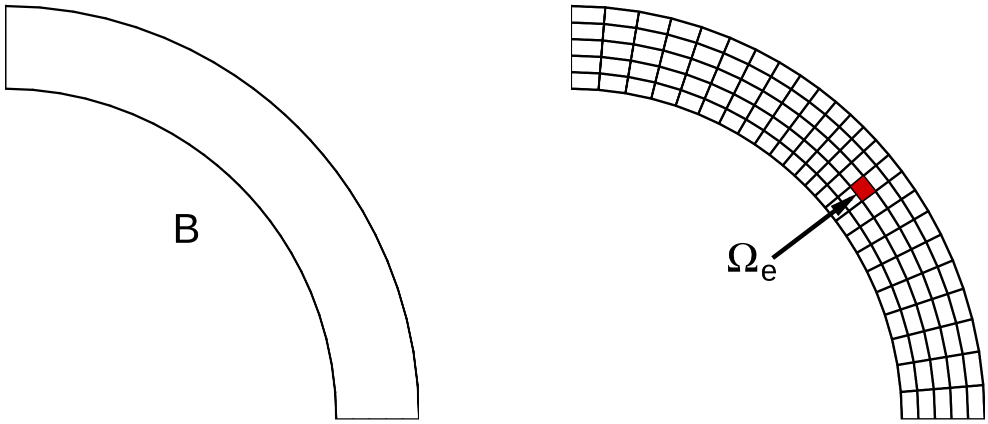

Figure 5.1: Discretization of a geometry.

following equation

$$\frac{\partial \mathbf{u}}{\partial t} \approx \frac{\Delta \mathbf{u}}{\Delta t} = \frac{\mathbf{u}_{n+1} - \mathbf{u}_n}{\Delta t}. \tag{5.2}$$

For the temporal evaluation of $\mathbf{u}$ there exist various methods which are described in detail in (Bathe, 1996), (Knabner & Angermann, 2003) or (Malcherek, 2001) amongst others. They are based on a weighting of the time steps given by:

$$u \approx \Theta\, \mathbf{u}_{n+1} + (1 - \Theta)\, \mathbf{u}_n \qquad\qquad 0 \le \Theta \le 1 \tag{5.3}$$

The common procedures can than shortly be summarized by:

1. *Explicit (forward) Euler*

$$\Theta = 0 \tag{5.4}$$

2. *Implicit (backward) Euler*

$$\Theta = 1 \tag{5.5}$$

3. *Crank-Nicolson (semi-implicit)*

$$\Theta = 0.5 \tag{5.6}$$

Depending on the mathematical problem, the usage of one of these methods might make sense. While the *Explicit Euler* method comprises very small computational costs, the time steps have to be reduced to avoid stability problems (investigation of the Neumann number, see appendix

A.5). In contrast to that, the time steps may be larger for the solution with an *Implicit Euler* method. But this method incorporates higher computational costs. Additionally, it causes numerical diffusion effects which leads to numerical damping of the computed solution. The investigation of the local method error indicates that both of these methods comprise accuracies of the order $\mathcal{O}(\Delta t)$, which means that the solution converges linear to the exact solution when the time step is reduced. An advantage of the *Crank-Nicolson* method is the accuracy of the order $\mathcal{O}(\Delta t^2)$, combined with a high stability and unfortunately high computational costs due to the asymmetry of the system matrix. Within the given framework, typically the implicit Euler method is used.

5.1.4 Boundary Conditions

The common boundary conditions are called *Dirichlet boundary condition* and *Neumann boundary condition*. Within the *Dirichlet boundary condition* the value interpolated over the boundary equals the given value. For example it yields for the unknown $\mathbf{u}$:

$$\mathbf{u} = BC_D \qquad \text{on} \;\; \Gamma_D. \tag{5.7}$$

For example this boundary condition is used for mechanical displacement boundary conditions.

In contrast to that, the *Neumann boundary condition* declares the gradient of the field variable over the boundary

$$\partial\mathbf{u} = BC_N \qquad \text{on} \;\; \Gamma_N. \tag{5.8}$$

This boundary condition is e.g. used to simulate the fluxes due to a pump or a sheet piling.

5.2 Weak formulation of the coupled problem

Coupled hydraulic-mechanical problems can be divided in single but coupled subproblems. For each of these problems balance equations have to be fulfilled. Combined with constitutive equations like material laws a system of equations can be build. Within the finite element program this system has to be solved by a numerical approach. In this chapter, the derivation of the set of equations for the coupled hydraulic-mechanical problem is shown exemplarily. More information about this topic is given in (Zienkiewicz & Taylor, 2005) and (Lewis & Schrefler, 2000) amongst others.

5.2.1 Mechanical subproblem

The conservation of linear momentum is already presented in section 2.3.2 and states the equilibrium of inertial stresses and volume and surface loads. Applying the principle of virtual work for this relation, all constituents are multiplied by an arbitrary virtual displacement $\delta\mathbf{u}$. Additional incorporation of the incremental form, introducing the increments of all variables given by d(•) leads to the weak form

$$\int_B \delta\boldsymbol{\varepsilon}^T \mathrm{d}\boldsymbol{\sigma}_{\mathrm{tot}}\,\mathrm{d}v - \int_B \delta\mathbf{u}^T \rho_{\mathrm{m}} \mathrm{d}\mathbf{b}\,\mathrm{d}v - \int_{\partial B} \delta\mathbf{u}^T \mathrm{d}\mathbf{t}\,\mathrm{d}a = 0. \tag{5.9}$$

This equation contains the total stresses, which should be replaced by the effective stresses given in equation (2.82) resulting to

$$\int_B \delta\boldsymbol{\varepsilon}^T \mathrm{d}\boldsymbol{\sigma}_{\mathrm{tot}}\,\mathrm{d}v = \int_B \delta\boldsymbol{\varepsilon}^T \frac{\partial\boldsymbol{\sigma}_{\mathrm{eff}}}{\partial t}\,\mathrm{d}v - \int_B \delta\boldsymbol{\varepsilon}^T \mathbf{m}\frac{\partial p}{\partial t}\,\mathrm{d}v \tag{5.10}$$

in the weak formulation. The additional multiplicators α and χ given in equation (2.85) are neglected in this chapter. Incorporating this approach in the weak form it results

$$\int_B \delta\boldsymbol{\varepsilon}^T \frac{\partial\boldsymbol{\sigma}_{\mathrm{eff}}}{\partial t}\,\mathrm{d}v - \int_B \delta\boldsymbol{\varepsilon}^T \mathbf{m}\frac{\partial p}{\partial t}\,\mathrm{d}v - \int_B \delta\mathbf{u}^T \rho_{\mathrm{m}} \mathrm{d}\mathbf{b}\,\mathrm{d}v - \int_{\partial B} \delta\mathbf{u}^T \mathrm{d}\mathbf{t}\,\mathrm{d}a = 0. \tag{5.11}$$

The constitutive relation for the material model is already given in equation (2.80). Extended by an additional term the effect of compressible grains is introduced. In its incremental form this term yields

$$\mathrm{d}\boldsymbol{\sigma}_{\mathrm{eff}} = \mathbb{C}(\mathrm{d}\boldsymbol{\varepsilon} - \mathrm{d}\boldsymbol{\varepsilon}_{\boldsymbol{p}}) \tag{5.12}$$

with the material matrix $\mathbb{C}$ and the additional term $\mathrm{d}\boldsymbol{\varepsilon}_{\boldsymbol{p}}$ due to the pore water pressure acting on the compressible grains given by:

$$\int_B \delta\boldsymbol{\varepsilon}^T \mathbb{C}\frac{\mathbf{m}}{3K_s}\frac{\partial p}{\partial t}\,\mathrm{d}v. \tag{5.13}$$

Combining all these appendages, the mechanical subproblem states

$$\begin{aligned}\int_B \delta\boldsymbol{\varepsilon}^T \mathbb{C}\frac{\partial\boldsymbol{\varepsilon}}{\partial t}\,\mathrm{d}v - \int_B \delta\boldsymbol{\varepsilon}^T \mathbf{m}\frac{\partial p}{\partial t}\,\mathrm{d}v + \int_B \delta\boldsymbol{\varepsilon}^T \mathbb{C}\frac{\mathbf{m}}{3K_s}\frac{\partial p}{\partial t}\,\mathrm{d}v \\ - \int_B \delta\mathbf{u}^T \rho_{\mathrm{m}} \mathrm{d}\mathbf{b}\,\mathrm{d}v - \int_{\partial B} \delta\mathbf{u}^T \mathrm{d}\mathbf{t}\,\mathrm{d}a = 0\end{aligned} \tag{5.14}$$

5.2.2 Hydraulic subproblem

Typically, the hydraulic subproblem is given by the mass balance, containing the fluxes, a storage term due to pressure or saturation modifications and a storage term due to deformations. This is already presented in section 2.3.1 where the problem is restricted to incompressible solid grains and a constant fluid density. Writing this in a more general way the mass balance can be given by

$$\nabla\cdot\mathbf{q} + S_p\, n\, \rho^{\mathrm{w}}\frac{\partial p}{\partial t} + \mathbf{S}_u\, \rho^{\mathrm{w}}\, S^{\mathrm{w}}\frac{\partial\boldsymbol{\varepsilon}}{\partial t} = 0. \tag{5.15}$$

Within this context, the storage term due to deformations $\mathbf{S}_u$ is given by

$$\mathbf{S}_u = \mathbf{m}^T - \frac{\mathbf{m}^T\mathbb{C}}{3K_s} \tag{5.16}$$

where the first term incorporates the rate of change of the total volumetric strain and the last term pictures the deformations of the solid grains.

The storage term due to pressure modifications S_p yields:

$$S_p = \frac{(1-n)}{K_s} + \frac{n}{K_f} - \frac{1}{(3K_s)^2}\mathbf{m}^T \mathbb{C}\,\mathbf{m} \tag{5.17}$$

with the deformation of the solid grains due to pressure, changes of the fluid density and deformation of the solid grains due to modifications of the acting stresses.

In addition to the equilibrium condition, the constitutive *Darcy´s law* given in equation (2.91) has to be incorporated in the model which results in the following formulation of the mass balance equation

$$-\nabla \cdot \left(\frac{\mathbf{k}\,k_{\mathrm{rel}}}{\eta}(\nabla p - \rho^{\mathrm{w}}\mathbf{g}) \right) + \mathbf{S}_u\,\rho^{\mathrm{w}}\,\frac{\partial \boldsymbol{\varepsilon}}{\partial t} + S_p\,n\,\rho^{\mathrm{w}}\frac{\partial p}{\partial t} = 0. \tag{5.18}$$

Applying the method of weighted residuals by multiplying the mass balance equation by an arbitrary weight function w yields:

$$-\int_B w\nabla \cdot \left(\frac{\mathbf{k}\,k_{\mathrm{rel}}}{\eta}(\nabla p - \rho^{\mathrm{w}}\mathbf{g}) \right) \mathrm{d}v + \int_B w\mathbf{S}_u\,\rho^{\mathrm{w}}\,\frac{\partial \boldsymbol{\varepsilon}}{\partial t}\,\mathrm{d}v + \int_B wS_p\,n\,\rho^{\mathrm{w}}\frac{\partial p}{\partial t}\,\mathrm{d}v = 0 \tag{5.19}$$

A partial integration due to the Green‘s Theorem of the first term leads to the hydraulic subproblem

$$\begin{aligned} -\int_B (\nabla w)^T \left(\frac{\mathbf{k}\,k_{\mathrm{rel}}}{\eta}(\nabla p - \rho^{\mathrm{w}}\mathbf{g}) \right) \mathrm{d}v + \int_B w\,\mathbf{S}_u\,\rho^{\mathrm{w}}\,\frac{\partial \boldsymbol{\varepsilon}}{\partial t}\,\mathrm{d}v \\ + \int_B wS_p\,n\,\rho^{\mathrm{w}}\frac{\partial p}{\partial t}\,\mathrm{d}v + \int_{\partial B} w\,q\,\mathrm{d}a = 0. \end{aligned} \tag{5.20}$$

5.3 Usage of the FEM for the coupled problem

For the solution of the derived system of equations, the field variables on the elements, introduced in chapter 5.1.2, are converged by shape functions. Due to the *Galerkin* approach the weighting functions of the elements are equal to the ansatz functions of the field variables. Within the coupled simulation of geotechnical problems the common way is to choose quadratic ansatz functions for the mechanical problem and linear ansatz functions for the hydraulic problem. Considering the coupled hydraulic-mechanical problem the ansatz functions for the displacement $\mathbf{N_u}$ and the pressure N_p for every single element are incorporated in the following way

$$\mathbf{u} = \mathbf{N_u}\,\tilde{\mathbf{u}} \tag{5.21}$$

$$p = N_p\,\tilde{p} \tag{5.22}$$

$$w = N_p \tag{5.23}$$

to approximate the displacement field $\mathbf{u}$, the pressure field p and the weighting function w in dependency of the values at the nodes given by $\tilde{\mathbf{u}}$ and $\tilde{p}$. Within this description, $\mathbf{N_u}$ and N_p are defined on every node of the given element as follows:

$$\mathbf{N_u} = \begin{bmatrix} \mathbf{N_u} \\ \mathbf{N_v} \\ \mathbf{N_w} \end{bmatrix} \quad \text{with} \quad \mathbf{N_u} = \mathbf{N_v} = \mathbf{N_w} = \begin{bmatrix} N_u^{\mathrm{n1}}, N_u^{\mathrm{n2}}, N_u^{\mathrm{n3}}, ...N_u^{\mathrm{nn}} \end{bmatrix}$$

$$\text{and} \quad \mathbf{N_p} = \begin{bmatrix} N_p^{\mathrm{n1}}, N_p^{\mathrm{n2}}, N_p^{\mathrm{n3}}, ...N_p^{\mathrm{nn}} \end{bmatrix}.$$

The strains result to

$$\boldsymbol{\varepsilon} = \mathbf{B}\,\tilde{\mathbf{u}} \tag{5.24}$$

with

$$\mathsf{B} = \begin{bmatrix} N_{u,x} & 0 & 0 \\ 0 & N_{v,y} & 0 \\ 0 & 0 & N_{w,z} \\ N_{u,y} & N_{v,x} & 0 \\ 0 & N_{v,z} & N_{w,y} \\ N_{u,z} & 0 & N_{w,x} \end{bmatrix}.$$

5.3.1 Mechanical subproblem

With these definitions for each element, the equilibrium condition for the mechanical subproblem on the domain *B*, derived in equation (5.14), is given by

$$\begin{aligned} \int_B \delta\tilde{\mathbf{u}}^T \mathbf{B}^T \mathbb{C} \mathbf{B}\, \mathrm{d}v \frac{\mathrm{d}\tilde{\mathbf{u}}}{\mathrm{d}t} - \int_B \delta\tilde{\mathbf{u}}^T \mathbf{B}^T \mathbf{m} \mathbf{N}_p\, \mathrm{d}v \frac{\mathrm{d}\tilde{p}}{\mathrm{d}t} + \int_B \delta\tilde{\mathbf{u}}^T \mathbf{B}^T \mathbb{C} \frac{\mathbf{m}}{3K_s} \mathbf{N}_p\, \mathrm{d}v \frac{\mathrm{d}\tilde{p}}{\mathrm{d}t} \\ - \int_B \delta\tilde{\mathbf{u}}^T \rho_{\mathrm{m}} \mathbf{N}_u^T \frac{\mathrm{d}\mathbf{b}}{\mathrm{d}t}\, \mathrm{d}v - \int_{\partial B} \delta\tilde{\mathbf{u}}^T \mathbf{N}_u^T \frac{\mathrm{d}\mathbf{t}}{\mathrm{d}t}\, \mathrm{d}a = 0 \end{aligned} \tag{5.25}$$

with the tensor of the first order $\mathbf{N}_p$ and the tensor of the second order $\mathbf{N}_u^T$. This can be simplified to

$$\begin{aligned} \int_B \mathbf{B}^T \mathbb{C} \mathbf{B}\, \mathrm{d}v \frac{\mathrm{d}\tilde{\mathbf{u}}}{\mathrm{d}t} - \int_B \mathbf{B}^T \mathbf{m} \mathbf{N}_p\, \mathrm{d}v \frac{\mathrm{d}\tilde{p}}{\mathrm{d}t} + \int_B \mathbf{B}^T \mathbb{C} \frac{\mathbf{m}}{3K_s} \mathbf{N}_p\, \mathrm{d}v \frac{\mathrm{d}\tilde{p}}{\mathrm{d}t} \\ - \int_B \rho_{\mathrm{m}} \mathbf{N}_u^T \frac{\mathrm{d}\mathbf{b}}{\mathrm{d}t}\, \mathrm{d}v - \int_{\partial B} \mathbf{N}_u^T \frac{\mathrm{d}\mathbf{t}}{\mathrm{d}t}\, \mathrm{d}a = 0 \end{aligned} \tag{5.26}$$

and summarized by

$$\mathbf{K}\frac{\mathrm{d}\tilde{\mathbf{u}}}{\mathrm{d}t} + \mathbf{L}\frac{\mathrm{d}\tilde{p}}{\mathrm{d}t} = \frac{\mathrm{d}\mathbf{f}}{\mathrm{d}t} \tag{5.27}$$

with the stiffness matrix

$$\mathbf{K} = -\int_B \mathbf{B}^T \mathbb{C} \mathbf{B} \, \mathrm{d}v, \tag{5.28}$$

the coupling term

$$\mathbf{L} = \int_B \mathbf{B}^T \mathbf{m} N_p \, \mathrm{d}v - \int_B \mathbf{B}^T \mathbb{C} \frac{\mathbf{m}}{3K_s} N_p \, \mathrm{d}v \tag{5.29}$$

where the first term results from the introduction of the effective stresses and the second one from the observance of the pore pressure on the solid grains; and finally the external loads and the internal loads due to gravity given by $\mathrm{d}\mathbf{f}$

$$\mathrm{d}\mathbf{f}_u = \int_B \rho_{\mathrm{m}} \, \mathbf{N}_u^T \mathrm{d}\mathbf{b} \, \mathrm{d}v - \int_{\partial B} \mathbf{N}_u^T \mathrm{d}\mathbf{t} \, \mathrm{d}a. \tag{5.30}$$

5.3.2 Hydraulic subproblem

Accordingly, the hydraulic subproblem on the domain Ω given by equation (5.20) yields

$$\begin{aligned} -\int_B (\nabla \mathbf{N_p})^T \frac{\mathbf{k}\, k_{\mathrm{rel}}}{\eta} \nabla \mathbf{N_p} \, \mathrm{d}v \, \tilde{p} + \int_B (\nabla \mathbf{N_p})^T \frac{\mathbf{k}\, k_{\mathrm{rel}}}{\eta} \rho^{\mathrm{w}} \mathbf{g} \, \mathrm{d}v \\ + \int_B \mathbf{N_u}^T \rho^{\mathrm{w}} \, (\mathbf{m}^T - \frac{\mathbf{m}^T \mathbb{C}}{3K_s}) \mathbf{B} \, \mathrm{d}v \frac{d\tilde{\mathbf{u}}}{dt} \\ + \int_B \mathbf{N_p}^T n \, \rho^{\mathrm{w}} \left(\frac{(1-n)}{K_s} - \frac{n}{K_f} - \frac{1}{(3K_s)^2} \mathbf{m}^T \mathbb{C} \mathbf{m} \right) \mathbf{N_p} \, \mathrm{d}v \frac{d\tilde{p}}{dt} \\ + \int_{\partial B} \mathbf{N_p}^T q \, \mathrm{d}a = 0 \end{aligned} \tag{5.31}$$

which can be arranged to

$$\mathbf{H}\tilde{\mathbf{p}} + \mathbf{S} \frac{d\tilde{\mathbf{p}}}{dt} + \mathbf{L^T} \frac{d\tilde{\mathbf{u}}}{dt} = \mathbf{f}_p \tag{5.32}$$

with the term due to the fluxes in the investigated area

$$\mathbf{H} = -\int_B (\nabla \mathbf{N_p})^T \frac{\mathbf{k}\, k_{\mathrm{rel}}}{\eta} \nabla \mathbf{N_p} \, \mathrm{d}v, \tag{5.33}$$

the coupling term incorporating variable grain sizes and fluid densities

$$\mathbf{S} = \int_B \mathbf{N_p}^T n \, \rho^{\mathrm{w}} \left(\frac{(1-n)}{K_s} - \frac{n}{K_f} - \frac{1}{(3K_s)^2} \mathbf{m}^T \mathbb{C} \mathbf{m} \right) \mathbf{N_p} \, \mathrm{d}v, \tag{5.34}$$

the coupling term incorporating variations of the total strains and the grain sizes

$$\mathbf{L^T} = \int_B \mathbf{N_u} \, \rho^{\mathrm{w}} \, \mathbf{m} \mathbf{B}^T \, \mathrm{d}v - \int_B \mathbf{N_u} \, \rho^{\mathrm{w}} \, \mathbb{C} \frac{\mathbf{m}}{3K_s} \mathbf{B}^T \, \mathrm{d}v, \tag{5.35}$$

and the term due to gravity and the fluxes over the boundary of the area

$$\mathbf{f}_p = \int_B (\nabla \mathbf{N_p})^T \frac{\mathbf{k}\, k_{\mathrm{rel}}}{\eta} \rho^{\mathrm{w}} \mathbf{g} \, \mathrm{d}v + \int_{\partial B} \mathbf{N_p}^T q \, \mathrm{d}a. \tag{5.36}$$

5.3.3 Temporal discretization

Finally, the discretization in time has to be carried out for equations (5.27) and (5.32). Solving this system with an *Implicit Euler* algorithm, it yields

$$\mathbf{K}\Delta\tilde{\mathbf{u}} + \mathbf{L}\tilde{\mathbf{p}}_{(n+1)} = \mathbf{f}_{u,(n+1)} + \mathbf{L}\tilde{\mathbf{p}}_{(n)} \tag{5.37}$$

$$\mathbf{H}\tilde{\mathbf{p}}_{(n+1)} + \mathbf{S}\frac{\tilde{\mathbf{p}}_{(n+1)}}{\Delta t} + \mathbf{L}^{\mathbf{T}}\frac{\Delta\tilde{\mathbf{u}}}{\Delta t} = \mathbf{f}_{p,(n+1)} + \mathbf{S}\frac{\tilde{\mathbf{p}}_{(n)}}{\Delta t}. \tag{5.38}$$

with the number of time steps n.

5.3.4 Formulation of a coupled hydraulic–mechanical problem for the numerical solution by the FEM

Summarizing the derivations of the last chapters, the coupled hydraulic-mechanical problem can be formulated for the solution within a FEM formulation in the following way:

$$\mathbf{K}\Delta\tilde{\mathbf{u}} + \mathbf{L}\tilde{\mathbf{p}}_{(n+1)} = \mathbf{f}_{u,(n+1)} + \mathbf{L}\tilde{\mathbf{p}}_{(n)} \tag{5.39}$$

$$\mathbf{H}\tilde{\mathbf{p}}_{(n+1)} + \mathbf{S}\frac{\tilde{\mathbf{p}}_{(n+1)}}{\Delta t} + \mathbf{L}^{\mathbf{T}}\frac{\Delta\tilde{\mathbf{u}}}{\Delta t} = \mathbf{f}_{p,(n+1)} + \mathbf{S}\frac{\tilde{\mathbf{p}}_{(n)}}{\Delta t} \tag{5.40}$$

With the following definitions

$$\mathbf{K} = \mathbf{K}_{uu} \tag{5.41}$$

$$\mathbf{L} = \mathbf{C}_{up} \tag{5.42}$$

$$\mathbf{L}^{T} = \mathbf{C}_{pu} \tag{5.43}$$

$$\mathbf{H} + \frac{\mathbf{S}}{\Delta t} = \mathbf{K}_{pp} \tag{5.44}$$

$$\mathbf{f}_{u,(n+1)} + \mathbf{L}\tilde{\mathbf{p}}_{(n)} = \mathbf{R}_{u} \tag{5.45}$$

$$\mathbf{f}_{p,(n+1)} + \mathbf{S}\frac{\tilde{\mathbf{p}}_{(n)}}{\Delta t} = \mathbf{R}_{p} \tag{5.46}$$

the system of equations results in

$$\begin{bmatrix} \mathbf{K}_{uu}^{(n)} & \mathbf{C}_{up}^{(n)} \\ \mathbf{C}_{pu}^{(n)} & \mathbf{K}_{pp}^{(n)} \end{bmatrix} \begin{bmatrix} \Delta\mathbf{u}_{(i)}^{(n+1)} \\ \mathbf{p}_{(i)}^{(n+1)} \end{bmatrix} = \begin{bmatrix} \mathbf{R}_{u} \\ \mathbf{R}_{p} \end{bmatrix}. \tag{5.47}$$

This can be simplified with the matrix $\mathbf{M}$, the vector of unknowns $\mathbf{x}$ and the right side $\mathbf{f}$ to

$$\mathbf{M}(\mathbf{x})\mathbf{x} = \mathbf{f} \tag{5.48}$$

and solved numerically by an appropriate solver (please refer to section 5.4).

5.4 Solver

Common linear solvers like the Biconjugate gradient stabilized method are used for the mathematical solution of the problem (please refer to (Feldmann, 2001)). Due to various effects like coupling or material nonlinearities, the problem becomes nonlinear. As a consequence it has to be solved by nonlinear solvers, incorporating the incremental solution with the mentioned linear solver. There exist various ways to solve the nonlinear mathematical problem in a numerical way. Usually some kind of *fixed-point iterations* for finding a numerical approximation are used for the proposed kind of problems. There convergence can be investigated with the *Banach fixed-point theorem*. Some of the developed methods turned out to be robust with good convergence for the proposed physical problems. For more information please refer to (Knabner & Angermann, 2003), while a short introduction to the most important solvers relating geotechnical applications, namely the *Newton-Raphson* and the *Picard* iteration, is given here. Both of them are widely accepted, although both of them have advantages and disadvantages. While the *Newton-Raphson* iteration provides fast convergence, it is restricted to a small convergence radius and consequently the step size is bounded. Besides that, the adaption of the stiffness matrix for every step is very costly, due to the derivatives within the formulation (see section 5.4.1). As a consequence the *modified Newton-Raphson* iteration has been established, where the stiffness matrix is not adapted for every single step. In contrast to that, the *Picard* iteration provides a slow convergence combined with a great convergence radius. Section 5.4.2 and 5.4.1 give a short introduction to the *Picard* as well as the *Newton-Raphson* iteration.

5.4.1 Newton-Raphson iteration

The procedure of the Newton-Raphson iteration is given in various publications, for example it is presented in detail in (Wriggers, 2001) or (Zienkiewicz & Taylor, 2005). Consequently, only a short introduction is given here. The fundamental idea of the Newton iteration is the solvation of a system of equations $\mathbf{G}$ using the Taylor series at a given load step n:

$$\mathbf{G}(\mathbf{x}_{(n)} + \Delta\mathbf{x}_{(n+1)}) = \mathbf{G}(\mathbf{x}_{(n)}) + \mathrm{d}\mathbf{G}(\mathbf{x}_{(n)})\Delta\mathbf{x}_{(n+1)} + \mathbf{r}(\mathbf{x}_{(n)}) \tag{5.49}$$

Here the vector $\mathbf{r}$ presents higher order terms of the Taylor series and is neglected in the following. The linearisation $\mathrm{d}\mathbf{G}$ of $\mathbf{G}$ is called tangential matrix and in the following given by $\mathbf{M}$. Searching for the equilibrium GG$_{n+1}$ of the system of equations $\mathbf{G}(\mathbf{x}_{(n)} + \Delta\mathbf{x}_{(n+1)})$ at the actual load step $n+1$, this leads to:

$$\mathbf{G}(\mathbf{x}_{(n)} + \Delta\mathbf{x}_{(n+1)}) = \mathbf{G}(\mathbf{x}_{(n)}) + \mathbf{M}(\mathbf{x}_{(n)})\Delta\mathbf{x}_{(n+1)} \tag{5.50}$$

where GG$_n$ or $\mathbf{G}(\mathbf{x}_{(n)})$ and $\mathbf{M}(\mathbf{x}_{(n)})$ are known (see figure 5.3). The unknown $\mathbf{x}_{(n+1)}$ can be derived by

$$\mathbf{x}^i_{(n+1)} = \mathbf{x}^{GG}_{(n)} + \Delta\mathbf{x}^i_{(n+1)} \tag{5.51}$$

due to the iteration i of the total increment $\Delta\mathbf{x}_{(n+1)}$. With the residuum

$$\mathbf{G}(\mathbf{x}_{(n)} + \Delta\mathbf{x}_{(n+1)}) = \mathbf{R} = \mathbf{f}_{(n+1)} - \mathbf{M}(\mathbf{x}^i_{(n+1)})\mathbf{x}^i_{(n+1)} \approx \mathbf{0} \tag{5.52}$$

the end of the iterative procedure derives from the comparison with the tolerated error:

$$\parallel \mathbf{R} \parallel \leq TOL \tag{5.53}$$

.

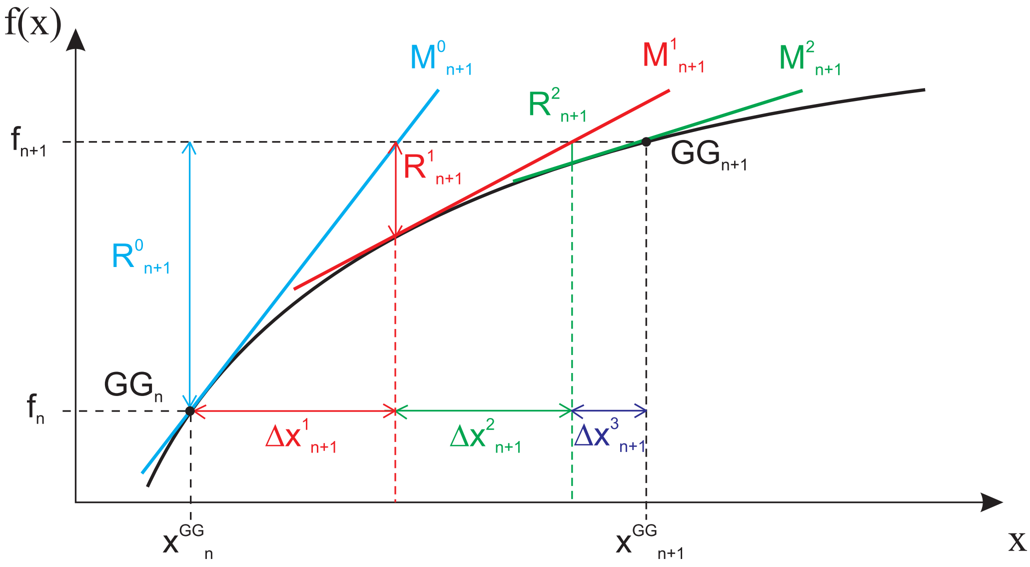

Figure 5.2: Procedure of the Newton iteration.

5.4.2 Picard iteration

The solution due to the Picard iteration is also given in various publications e.g. in (Zienkiewicz & Taylor, 2005). It ist directly evaluated by

$$\mathbf{G}(\mathbf{x}^{i+1}_{(n+1)}) = \mathbf{G}(\mathbf{x}^{i}_{(n+1)}) - \mathbf{M}(\mathbf{x}^{i}_{(n+1)})\Delta\mathbf{x}^{i}_{(n)} \tag{5.54}$$

with

$$\mathbf{G}(\mathbf{x}^{i}_{(n+1)}) = \mathbf{f}_{n+1} - \mathbf{M}(\mathbf{x}^{i}_{(n+1)})\mathbf{x}^{i}_{(n+1)} \tag{5.55}$$

and

$$\mathbf{M}(\mathbf{x}^{i+1}_{(n+1)}) = \mathbf{M}(\mathbf{x}^{i}_{(n+1)}) + \frac{\partial \mathbf{M}(\mathbf{x}^{i}_{(n+1)})}{\partial \mathbf{x}^{i}_{(n+1)}}\mathbf{x}^{i}_{(n+1)}. \tag{5.56}$$

Neglecting the second term of $\mathbf{M}(\mathbf{x}^{i+1}_{(n+1)})$ and replacing $\Delta\mathbf{x}^{i}_{(n)} = \mathbf{x}^{i+1}_{(n+1)} - \mathbf{x}^{i}_{(n+1)}$ one get

$$\mathbf{G}(\mathbf{x}^{i+1}_{(n+1)}) = \mathbf{R} = \mathbf{f}_{n+1} - \mathbf{M}(\mathbf{x}^{i}_{(n+1)})\mathbf{x}^{i+1}_{(n+1)} \approx \mathbf{0} \tag{5.57}$$

with the updated value

$$\mathbf{x}^{i+1}_{(n+1)} = \mathbf{M}(\mathbf{x}^{i}_{(n+1)})^{-1}\mathbf{f}_{n+1}. \tag{5.58}$$

Again, the iterative procedure ends if:

$$\parallel \mathbf{R} \parallel \leq TOL \tag{5.59}$$

.

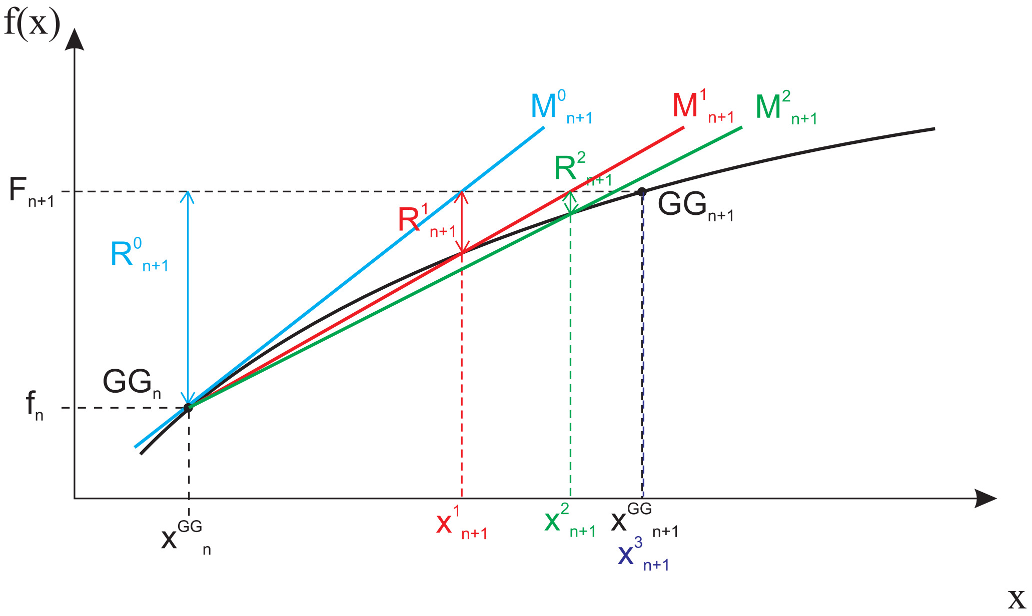

Figure 5.3: Procedure of the Picard iteration.

5.5 The finite element code RockFlow

The history of the finite element code RockFlow starts in the mid eighties. Within these years a finite element code for the simulation of flow processes in fractures was developed at the *Institute of Fluid Mechanics and Computer Applications in Civil Engineering (ISEB)*. For this purpose various routines were written in *Fortran* and documented in (Kröhn, 1991) and (Wollrath, 1990). These developments were extended to a simulator for multiphase flow problems by (Helmig, 1993) and (Shao, 1994) and supplemented by various mathematical features. Combined with the turn-over to the program language *C* the possibility of an adaptive grid refinement was implemented by (Barlag, 1997) and (Kaiser, 2001) in the nineties. Finally, the program was able to simulate ground water flow and transport as well as gas and heat transport, which is documented in (Kolditz, 1996). Afterwards further development focuses on multiphase flow (please refer to (Thorenz, 2001)) and reactive transport processes (please refer to (Habbar, 2001)). At the end of the nineties, these enhancements yield to the first official version of RockFlow.

In the following years it became obvious that in many fields of application various coupled processes, especially focusing on mechanical aspects have to be investigated. Furthermore, the features of an object oriented language should be used increasingly in the code. Consequently, (Kohlmeier, 2006) focuses on coupled thermo–hydro–mechanical effects with a special focus on the mechanical model using features of the program language *C++*. At the same time effort was made to develop a user-friendly program code. As a matter of fact, a Graphical User Interface (GUI) (please refer to (Kohlmeier, 2006)) was implemented and the documentation of the code was extended (Wulkau, 2005). These developments as well as the presentation in the internet support the publicity of the code, which is used by various users like the Federal

Institute for Geosciences and Natural Resources (BGR) and the (GGA).

Nowadays the code is used within various applications. One example is the project DECOVALEX THMC, which started in 2003 and refers to the investigation of coupled processes in potential host rocks for high radioactive waste disposal (please refer to (Ziefle, Kohlmeier, Massmann, & Zielke, 2005) and (Massmann, Ziefle, Kohlmeier, & Zielke, 2007)). Claystone as a potential host rock for the final disposal of radioactive waste is being investigated in several countries. The Federal Institute for Geosciences and Natural Resources (BGR) is involved in several international projects in clay formations, e.g. the Underground Laboratories at Mont Terri (Switzerland) and Bure (France). Within this context, RockFlow is enhanced by various processes and the applicability is proven due to relating simulations. The application concerning various geotechnical problems indicates that material properties have to be treated more in detail. Consequently, actual research, presented in the work at hand, focuses on non linear material behavior due to compressible material behavior as well as the coupling between hydraulic and mechanical processes due to changes of material properties and more complicated material models like hardening plasticity.

Chapter 6

Applications

6.1 Step-wise compression test

The impact of the non linear elastic compression behavior on the resulting strains and pressure evolution of a compression test is investigated within this section. A step-wise compression of an initially unloaded sample is simulated. The process is simulated as a coupled hydraulic-mechanical problem and consequently every load step leads to a classical consolidation problem with a time-dependent behavior until the final equilibrium stage is reached. As the consolidation process is a classical example of a coupled hydraulic-mechanical problem, the resulting deformation and pressure evolution are given in various literature. (Kohlmeier, 2006) uses this example to present a verification of the linear elastic model implemented in RockFlow due to the comparison with an analytical solution.

Comparing the linear elastic model with the non linear approach, a relatively high permeability is chosen, as the focus is laid on the pure mechanical process. Afterwards, the results derived with a significantly lower permeability are presented, leading to an increase of the water pressure and a more dominant time-dependent behavior. Concerning this example, the initial porosity is chosen to be equal to the stress-free porosity. The influence of a preloaded initial state is investigated in the next section.

6.1.1 Model setup

The soil column given in figure 6.1 is mechanically fixed and impermeable at the sides and at the bottom. At the top exists a permeable boundary and a time-dependent load is applied. The load results from a constant value of -125.0 kN/m multiplied with the time dependent load factor given in figure 6.1. The initial pore water pressure within the whole domain is assumed to be zero. The material properties are presented in table 6.1.

Additionally, a strain dependent porosity as well as a strain dependent permeability are assumed. The porosity results from equation (2.90) and the current relative permeability de-

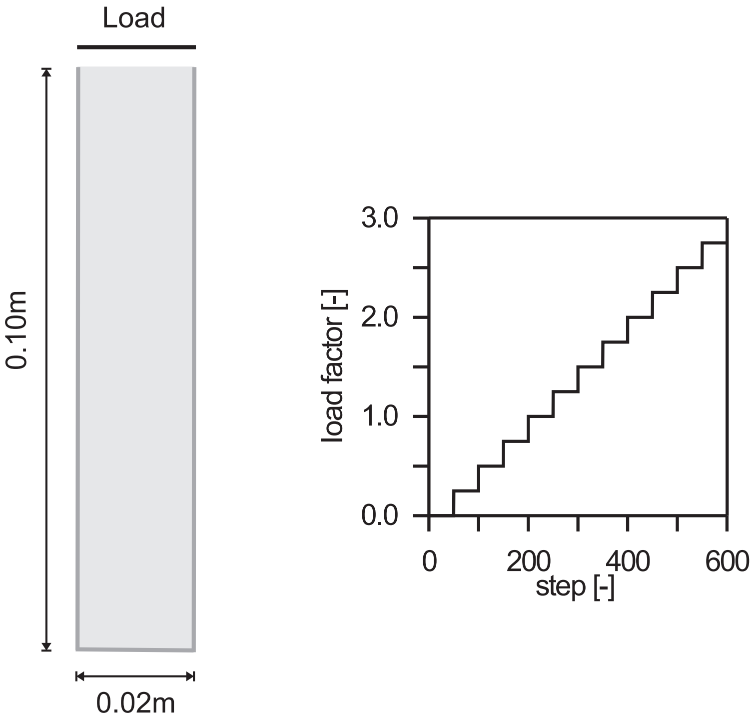

Figure 6.1: Geometry and load factor of the consolidation problem.

Parameter	Unit	Value
Young‘s modulus E	[kPa]	250
Poisson‘s ratio ν	[-]	0.2
Initial porosity n_{IC}	[-]	0.05
Stress-free porosity n_{SF}	[-]	0.05
Simulation with a higher intrinsic permeability k	[m^2]	5.0$\cdot$ 10^{-10}
Simulation with a lower intrinsic permeability k	[m^2]	5.0$\cdot$ 10^{-12}

Table 6.1: Material properties for the step-wise compression test.

pending on the porosity is given by the following linear relationship:

$$k_{\mathrm{rel,n}} = 0.5n + 0.5 \tag{6.1}$$

6.1.2 Results

Every load step leads to a classical consolidation problem. The pressure field and the fluxes for various time steps within one load step are presented in figure 6.2. The time-dependent decrease of the pressure field due to the fluid flow can be observed. The last picture shows the additional increase of pressures due to the next load step.

In the following the temporal evolution of the volumetric strains as well as the pressure evolution over the column height are investigated. Within this framework, the linear and the non linear model as well as a higher ($k = 5.0 \cdot 10^{-10}$m^2) and a lower ($k = 5.0 \cdot 10^{-12}$m^2) permeability are compared.

Linear versus non linear model

Due to the load controlled type of boundary condition at the top, the stresses increase step-wise with constant step increments. The evolution of strains depends on the type of constitutive model. In contrast to the constant strain increments arising by the linear elastic model, the non linear material model presented in chapter 3 leads to step-wise increasing but quantitatively varying strain increments. The results of both models are given in figure 6.3. The red line in the figures presents the stress-free porosity, which equals the initial porosity for this example.

Whereas the simulations pictured on the left are performed with the linear elasticity model, the results of the non linear model are given on the right side. Concerning the strains one can state that the final strains are bordered by the porosity of the material if the non linear model is used. Especially if high compressive strains lead to a significant reduction of the pore space, the results of the non linear model differ significantly from the results derived by the linear approach. Consequently, the simulation of problems including high compressions up to the compression point of the material have to be analyzed with the proposed model. As the compression point depends directly on the stress-free porosity of the material, the non linear elastic compressibility model is of special interest for materials with low porosities.

An additional effect can be observed investigating the strains. Due to the presented material model, the material behaves somehow stiffer than in the elastic case already for the initial case. Consequently, the strain increments are smaller than in the elastic case at the whole simulation time.

The evolution of the pressure field over the height is given in figure 6.4. At the left side, the results derived by the linear model are presented, at the right side, the non linear model is used. The evolution of the water pressure is given over the hight for various time steps within one load step by the green lines. The red line shows the pressure at one time step after the next load step. While the figures at the top, present the results for various time steps between step 50 and 101, the middle concentrates on step 150 to 201 and the bottom on step 450 to

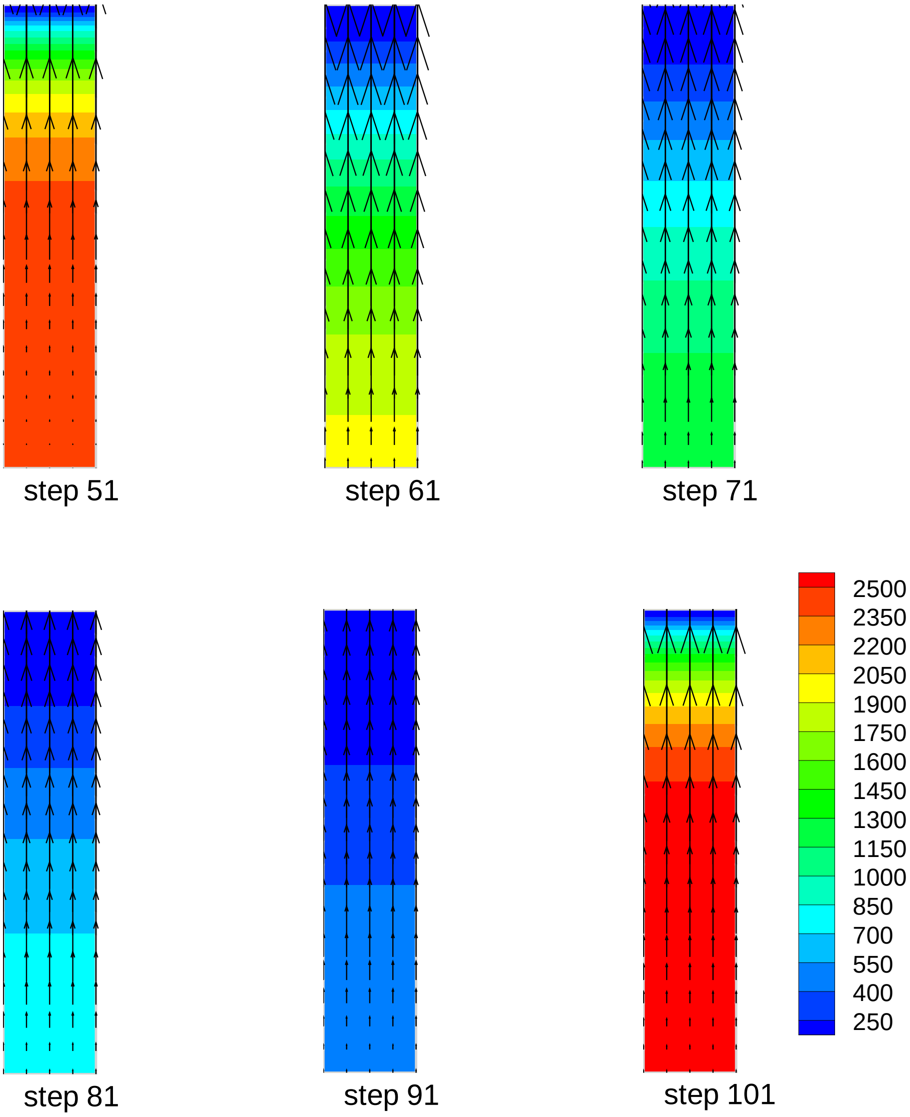

Figure 6.2: Pressure evolution [kPa] and resulting fluxes in the soil column between step 50 and 101.

501. Concerning the pressure field, it can easily be seen that lower strain increments lead to lower water pressures. Consequently, the impact of the material model increases significantly if the compression strains converge to the compression point.

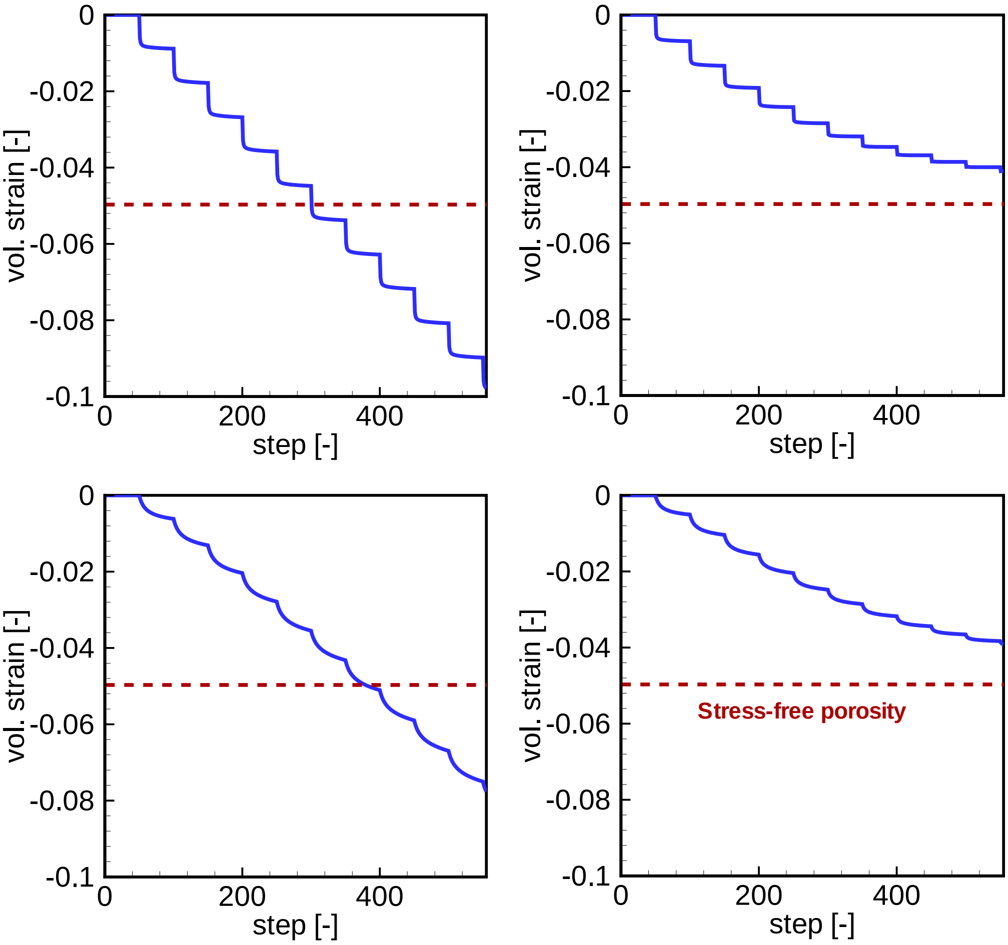

Figure 6.3: Temporal evolution of the volumetric strains. Left: Linear model. Right: Non linear model. Top: Higher permeability leads to a low time-dependent impact. Bottom: Lower permeability leads to a high time-dependency.

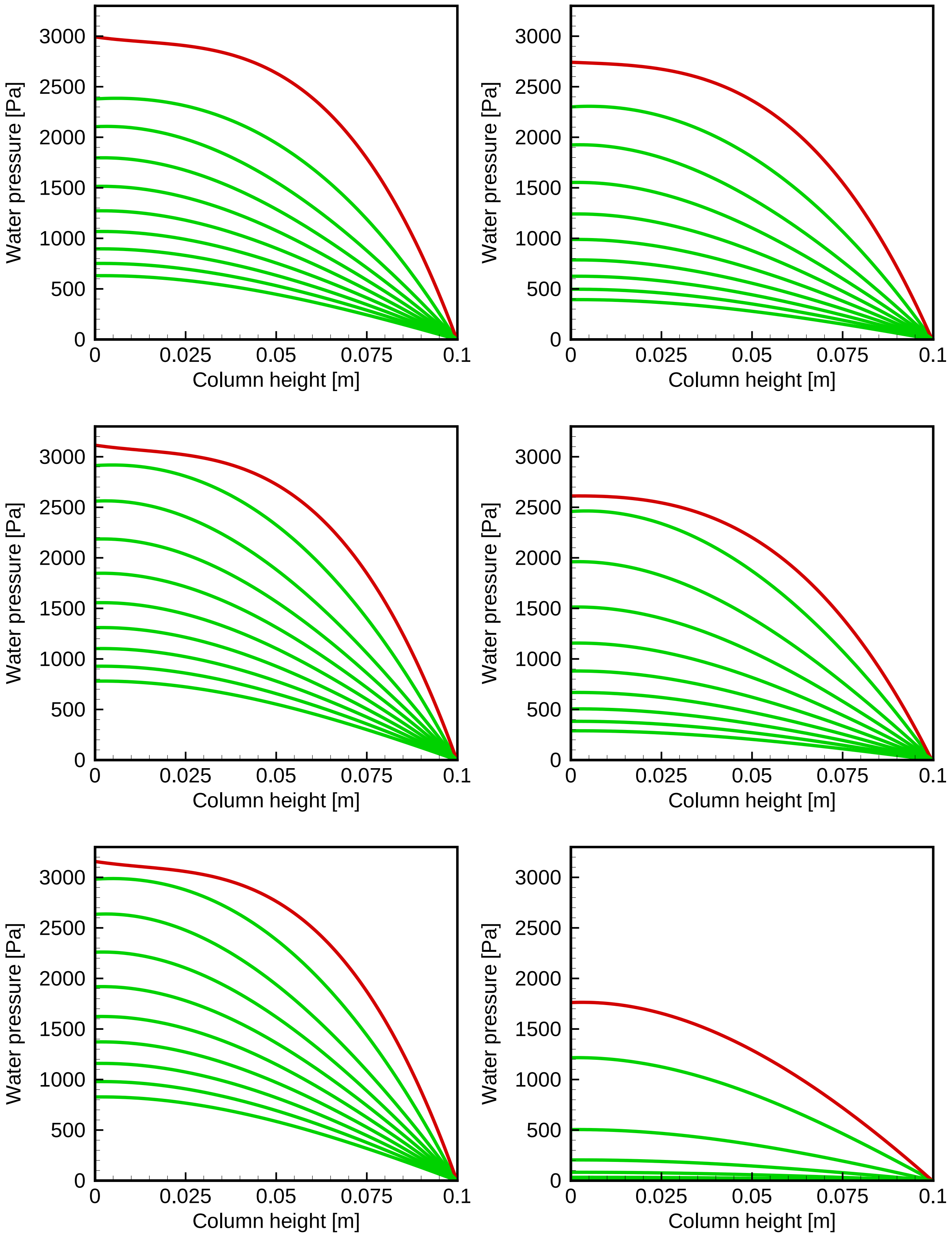

Figure 6.4: Impact of the material model on the pressure evolution at different time steps for the simulation with the higher permeability. Left: Linear elastic model. Right: Non linear elastic model. Top: Steps 50 to 101. Middle: Steps 150 to 201. Bottom: Steps 450 to 501.

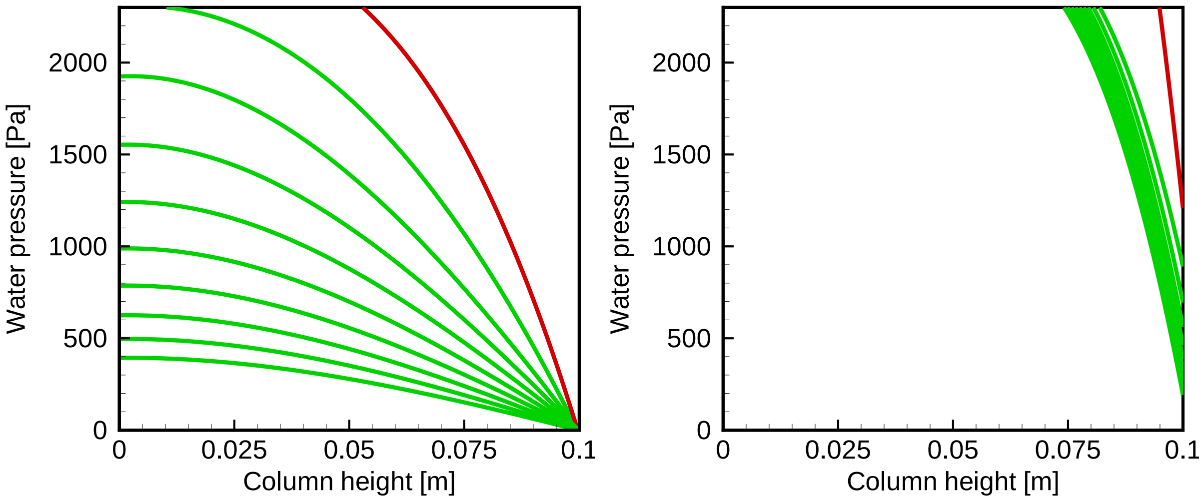

Figure 6.5: Pressure evolution over the column height resulting from a higher (left) and a lower (right) permeability. The pressure field is given for the steps 50 to 101.

Impact of a lower permeability

The influence of the hydraulic process increases if the permeability decreases. Significant temporal effects can be observed concerning the evolution of strains (see figure 6.3). Consequently, there is no equilibrium stage reached after a time increment of one load step. Besides that, the final conclusion remains the same. The non linear model has a significant influence if the pore space is reduced to the compression point by high compression strains.

Concerning the pressure evolution the lower permeability leads to significantly higher water pressures in the whole area. This can be seen in figure 6.5. As a consequence, the influence of the mechanical material model is of less importance related to the impact of the permeability. Anyhow, the pressure field is affected especially if the material converges to the compression point.

6.2 Step-wise compression of a preloaded sample

In contrast to the step-wise compression presented in section 6.1, the sample used here is already preloaded. This means that the initial porosity is not equal to the stress-free porosity (please refer to chapter 3). The behavior of this sample is investigated with the non linear elastic compressibility model.

6.2.1 Model setup

The model setup generally equals the setup of the step-wise compression test given in section 6.1. In contrast to the load presented there, the load given in this example results from a smaller constant value of -12.5 kN/m multiplied with the time dependent load factor given in the previous section (please refer to figure 6.1). The material properties are presented in table 6.2.

Parameter	Unit	Value
Young‘s modulus E	[kPa]	250
Poisson‘s ratio ν	[-]	0.2
Initial porosity n_{IC}	[-]	0.05
Stress-free porosity n_{SF}	[-]	0.15
Intrinsic permeability k	[m^2]	$5.0\cdot 10^{-10}$

Table 6.2: Material properties for the compression test on a preloaded sample.

6.2.2 Results

As the previous example shows, the stiffness of the material depends strongly on the existing porosity. If the initial porosity differs strongly from the stress-free porosity, the compressibility obviously decreases. Assuming the stress-free porosity to be 15% and the initial porosity to be 5% for the proposed consolidation problem, the resulting strains at the top of the column are given in figure 6.7. To show the influence of the hydraulic-mechanical coupling, the left side shows the results for a pure mechanical compaction of the material, whereas the right side presents the strains due to the consolidation problem. It can be seen that the resulting volumetric strains are relatively small, which results from the preloaded initial state. An overview of the pore space in the sample is given in figure 6.7 and indicates that the incompressible state is almost reached at the beginning of the simulation. There is only a small modification of the volumetric strains due to the increasing load. The remaining porosity is about 20% of the stress-free porosity. This dimension of the remaining porosity equals the experimental results given in (Stührenberg, 2004) and (Mondol et al., 2007).

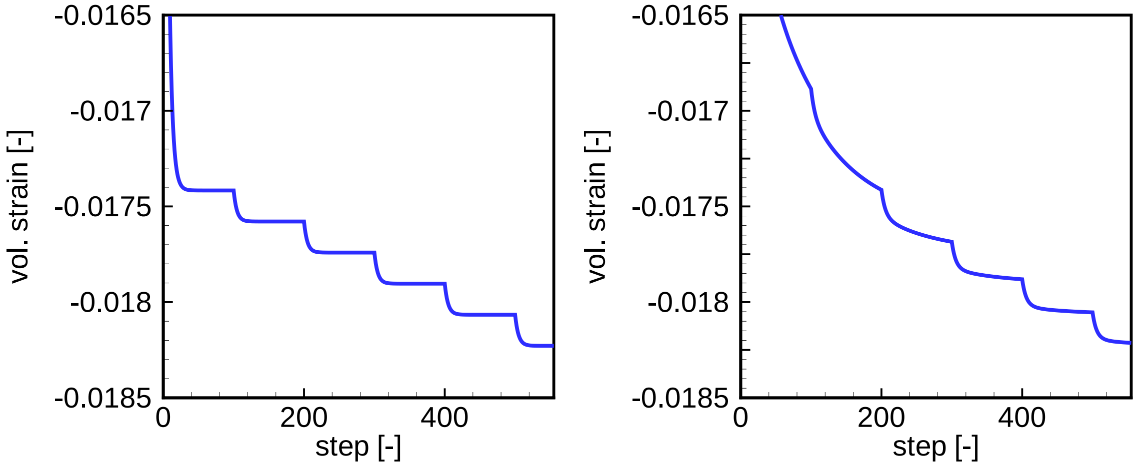

Figure 6.6: Resulting strains for the purely mechanical (left) and coupled hydraulic-mechanical (right) case.

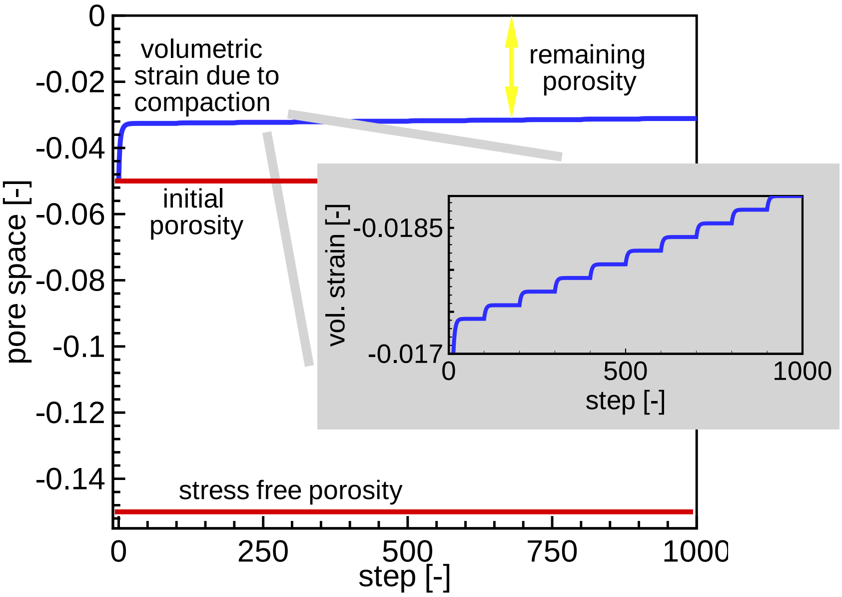

Figure 6.7: Evolution of the pore space due to the compression of the preloaded sample.

6.3 Foundation problem

The coupled hydraulic-mechanical simulation of a foundation problem with the finite element code RockFlow has already been presented in (Kohlmeier, 2006). Within that publication the von Mises as well as the Drucker-Prager plasticity are applied investigating the effect of plasticity focusing on dilatant and contractant behavior under drained and undrained conditions. It has been pointed out, that especially dilatant and contractant behavior may have a significant impact on the hydraulic process. Nevertheless, plastic effects due to a compression of the material can not be evaluated with that kind of models. Consequently, a pressure sensitive model of the Cam-Clay type has been implemented and is presented in this work. This section investigates the plastic behavior due to that kind of model. As significant volumetric plastic strains occur, this kind of model interacts strongly with the fluid flow. The impact on the hydraulic process, combined with the strain dependent permeability model and compared with a purely elastic simulation is given in section 6.5.

6.3.1 Model setup

The model domain is assumed to have a width of 12.0 m and a hight of 6.0 m. It is divided in 1800 quadrilateral elements and pictures Bay Mud, which material properties are presented in table 6.3.

Parameter	Unit	Value
Young‘s modulus E	[Pa]	$1\cdot 10^9$
Poisson‘s ratio ν	[-]	0.35
Acceleration due to gravity g	[m/s^2]	9.81
Cam-Clay parameter M	[-]	1.4
Preconsolidation p_c	[kPa]	10.0
Virgin compression index λ_{VCI}	[-]	0.37
Recompression index κ_{RCI}	[-]	0.054
Dry density ρ	[kg/m^3]	2038.74
Initial porosity n	[-]	0.2
Intrinsic Permeability k	[m^2]	$1\cdot 10^{-10}$

Table 6.3: Material properties for the simulation of the foundation problem.

The left and the right boundary are mechanically fixed in horizontal direction, while the bottom is fixed vertically. Besides that, the surface is assumed to be permeable while all other boundaries are impermeable. The initial water pressure as well as the initial compressive stresses in the whole domain are assumed to be 10.0 kPa. An initial load of 10.0 kN/m is brought up at the whole surface. Additional loads shortly were performed beside the fundament to derive an initial over consolidation. Furthermore, a uniform load is applied in the center of the top over a width of 0.60 m simulating a foundation. This load increases until a value of 80.0 kN/m is reached. This load represents about 95% of the full value of the failure load of Bay Mud. The difference between the load history in the area of and beside the foundation plate is presented in figure 6.8. The load history starts with an increase of the overall load for a very short time period. This leads to a higher initial over consolidation in the near field of the surface area than in deeper areas. Afterwards, the foundation load is continuously increasing while the load in the surrounding area is being reduced.

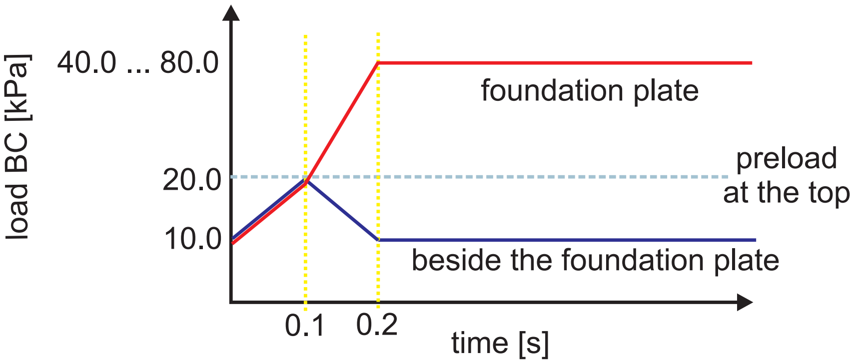

Figure 6.8: Load boundary condition at the top.

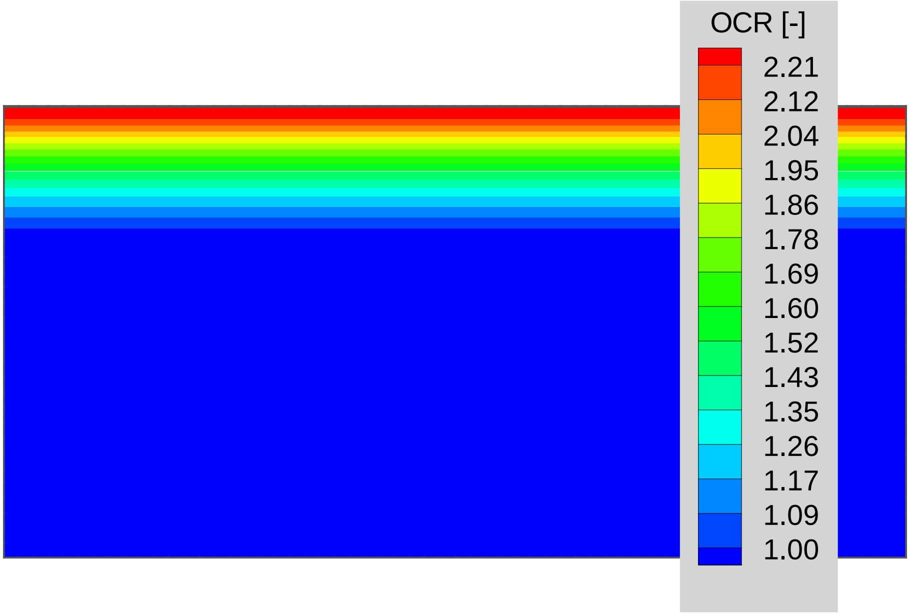

Figure 6.9: Over consolidation ratio (OCR) after 0.1 s.

6.3.2 Results

The over consolidation ratio (OCR) is given for the 100% load after the first load step (t=0.1 s) in figure 6.9. The over consolidation ratio represents the current over consolidation of the soil. It results from the proportion of the maximal to the current pressure distribution. The presented example incorporates an initial over consolidation at the top, which results directly from the temporary increase of the load at the whole top (see figure 6.8). Consequently, the OCR in the near field of the top is significantly higher than in greater depths. This is the common situation found in many geotechnical applications.

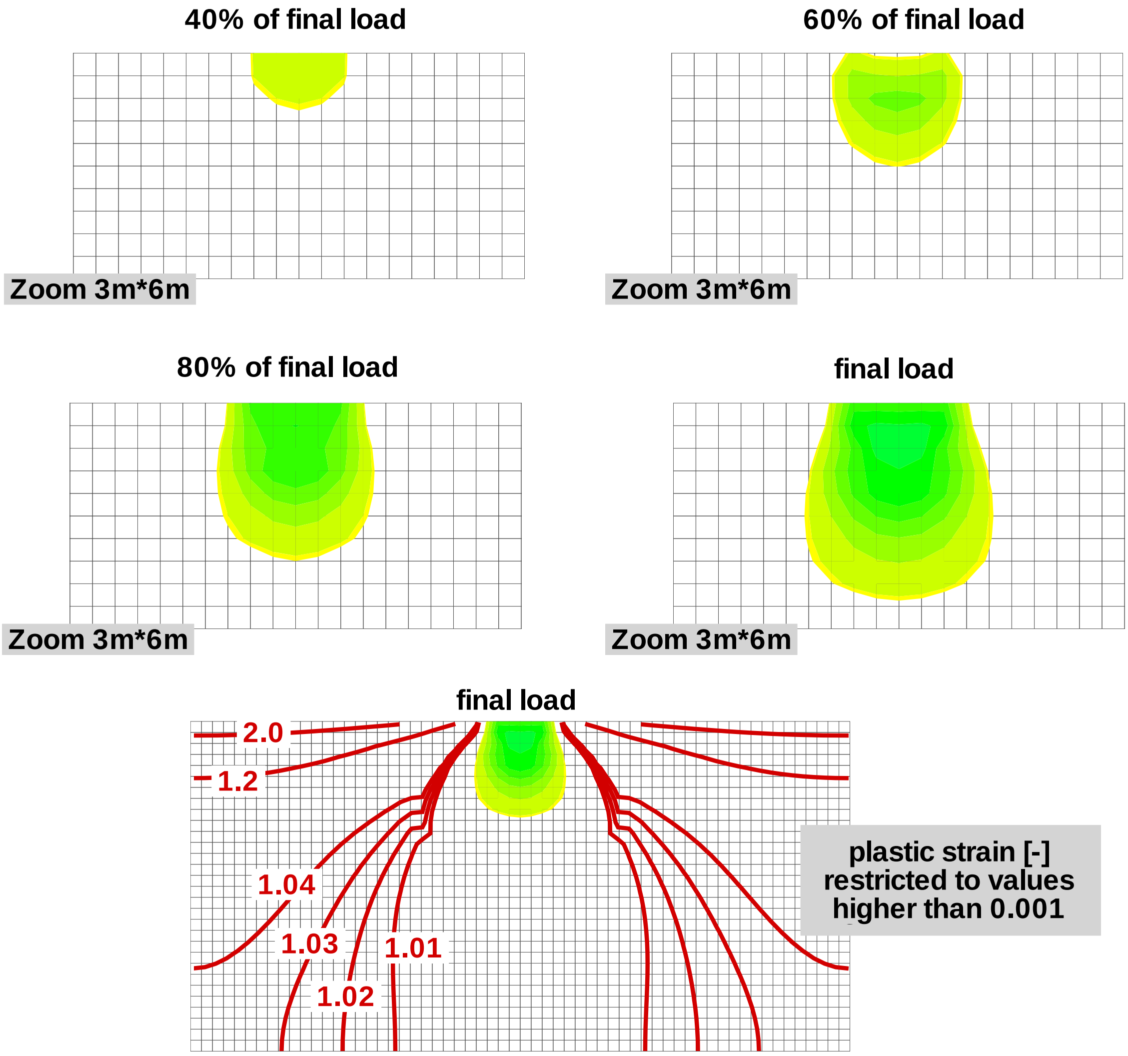

Figure 6.10: Zone of plastification corresponding to 40%, 60%, 80% and 100% of the full value of the applied load and distribution of the OCR for the 100% load.

The presented nonlinearly overconsolidated soil is loaded by an additional fundamental load.

The OCR due to that situation is pictured in figure 6.10 by the red lines presenting contour lines of the OCR. In the boundary areas, the initial situation has not changed significantly, but in the center the foundation load leads to higher pressures and consequently a decrease of the OCR.

Figure 6.10 additionally shows the volumetric plastic strains due to various load steps. It can be seen, that there exist plastic strains already at 40% of the final load. When the final load, which equals 95% of the failure load of this soil, is reached, a relatively large area contains plastic compression strains. As a consequence of the pressure sensitivity, the results differ significantly from the results obtained by plasticity models without this effect.

6.4 Hardening and softening behavior found in a triaxial test

As the triaxial test is one of the most common geotechnical experiments, there exist manifold data sets of the quantitative behavior of various materials in a triaxial test. Although, the presented example does not focus on a specific material and consequently there is no comparison with experimental data. In spite of that, the qualitative evolution of strains and stresses for various material properties is investigated. Depending on the material, plastic hardening and softening behavior can be shown.

6.4.1 Model setup

The triaxial test is simulated as a purely mechanical process in a 2-dimensional domain with a width and a height of 0.05 m. The proposed mesh contains 100 quadrilateral elements. It is mechanically fixed at the bottom and both sides. At the top, the displacement boundary condition is applied. This boundary condition provokes a z–displacement of -0.001 m at the top of the area. Additionally, an initial compression stress of 2.0 Pa is assumed in the whole domain. The material properties are summarized in table 6.4. The proposed Cam-Clay model uses the parameter M, which directly results from the friction angle ϕ of the material:

$$M = \frac{6 \sin \phi}{(3 - \sin \phi)} \tag{6.2}$$

Within the simulations the parameter M varies between 1.35 and 2.4, simulating various initial conditions of the material.

Parameter	Unit	Value
Young's modulus E	[Pa]	$1 \cdot 10^9$
Poisson's ratio ν	[-]	0.35
Acceleration due to gravity g	[m/s^2]	9.81
Dry density	[kg/m^3]	2000
Cam-Clay parameter M	[-]	1.35...2.4
Preconsolidation p_c	[Pa]	2.0
Virgin compression index λ_{VCI}	[-]	0.5
Recompression index κ_{RCI}	[-]	0.05

Table 6.4: Material properties for the simulation of the triaxial test.

6.4.2 Results

The resulting strains and stresses turn out to depend significantly on the condition of the material. High friction angles ϕ indicate a high Cam-Clay parameter M and are related to stable materials. These materials tend to be coarse with variable grain sizes potentially combined with an optimal water content and a compaction. Compression of this type of material leads to a hardening and relatively high maximum stresses. In contrast to that, materials with lower friction angles indicate softening behavior and lower maximum stresses.

Additionally it can be stated that the pure mechanical process is not time- but step-dependent and that the evolution remains the same for various loads. This will only lead to a change of the quantitative solution.

Softening material behavior

The results of a triaxial test with a material indicating softening behavior are presented in figure 6.11. The evolution of the deviatoric stresses is given at the top, the appropriate volumetric strains at the bottom. On the left hand side, the results derived by the finite element simulation with RockFlow are given. The simulations are carried out with a Cam-Clay parameter M lying in the range between 1.35 and 1.7, indicating softening.

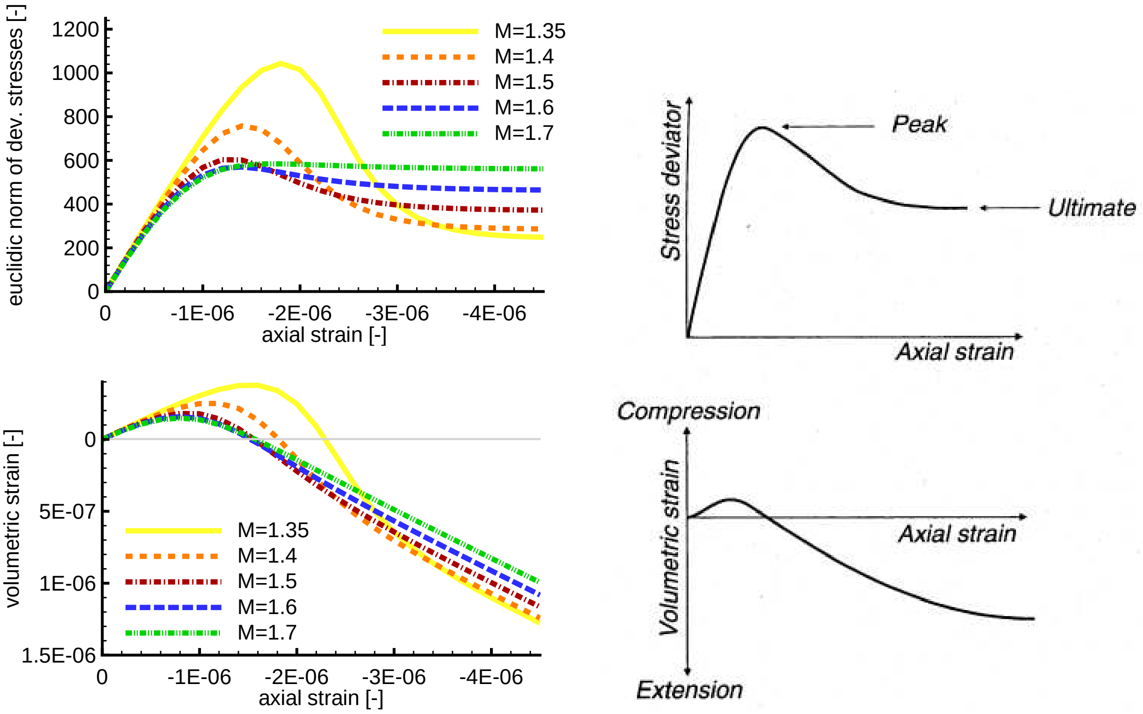

Figure 6.11: Euclidic norm of the deviatoric stresses (top) and the plastic strains over the axial strain (bottom) for different M indicating softening. Left: RockFlow results. Right: Typical evolution taken from (Davis & Selvadurai, 2002).

The derived stress- and strain-evolutions are classical results for a compression of a material in the context of a triaxial test. As a reference, the right side of figure 6.11 presents the characteristic evolution of strains and stresses for a triaxial test of a softening material taken from (Davis & Selvadurai, 2002).

Initially, the stresses increase and a compression takes place. Afterwards, a softening of the material takes place as a consequence of the plastic effects. This leads to a decrease of the stresses and a final ultimate stress, which is significantly lower than the peak stress. Due to this decrease of stresses, extension strains arise.

Hardening material behavior

Material with a higher Cam-Clay parameter M indicates a hardening material. Simulations of a triaxial test for values of M in the range between 1.8 and 2.4 are carried out with the finite element program. The resulting stress and strain evolutions are presented in figure 6.12 in the same way as before. It can be seen that there are significant differences in the final deviatoric stresses as well as in the volumetric strains. While the final ultimate stresses are significantly higher than before, the resulting extension strains are lower. Comparing both results with the softening behavior, the history dependency becomes clear, as both types of material show identical results in the first period of the test.

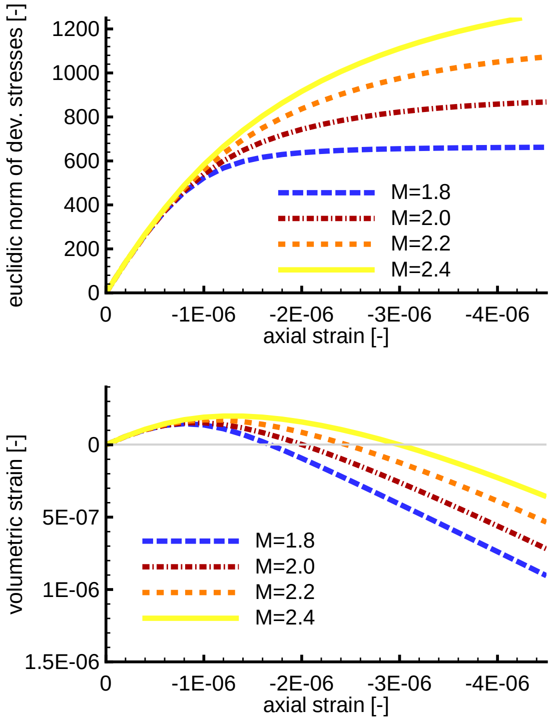

Figure 6.12: Euclidic norm of the deviatoric stresses and the plastic strains over the axial strain for different M indicating hardening.

6.5 Deformation induced strain dependent permeability

As explained in chapter 2, a strain dependent permeability is implemented in the finite element code RockFlow. Within this approach, the permeability depends on the current porosity, which directly depends on the arising volumetric strains. There exist various effects which affect the volumetric strains of a soil material. On the one side classical mechanical deformation processes are of special interest, on the other side hydraulic processes like swelling or shrinkage have to be mentioned in the case of unsaturated materials. Furthermore, the impact of plastic effects on the volumetric strains is incorporated in the model description.

This example presents the impact of mechanical deformation due to an elastic as well as an elasto-plastic simulation on the permeability of the material and on the hydraulic process.

6.5.1 Model setup

The impact of a mechanical load on the hydraulic process due to the classical couplings as well as the strain dependent permeability is investigated here. The fully saturated domain is assumed to have a width of 10.0 m and a height of 5.0 m and is presented in figure 6.13. The mechanical boundary conditions are stated by a fixed boundary on the bottom and horizontally fixed conditions at both sides. Initially, a load of 1.0 N/m is applied at the top and the initial compressive stresses as well as the initial water pressure in the whole domain are assumed to be 1.0 Pa. An additional load of 1000.0 N/m is brought up on a length of 2.0 m in the center of the top. Within a time interval of 10 sec it increases to the final value. The hydraulic boundary conditions are given by impermeable boundaries at the top and the bottom and a pressure gradient given by a pressure of 1000.0 Pa at the left side and a pressure of 1.0 Pa at the right side. The evaluation of the results is carried out after a time period of 20 sec when the equilibrium stage is reached.

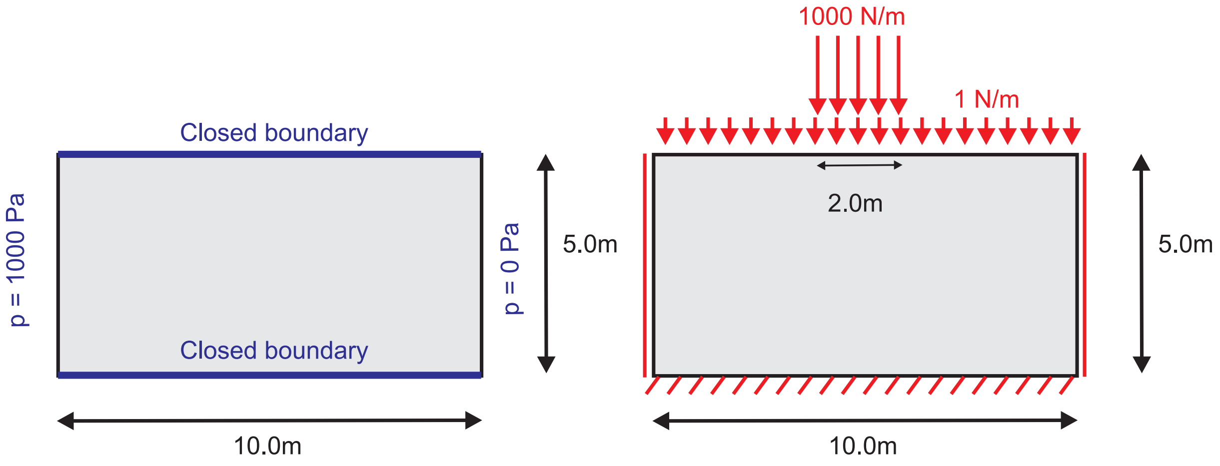

Figure 6.13: Model setup for the elastic and elasto-plastic deformation example. Left: Hydraulic subproblem. Right: Mechanical subproblem.

The material properties are summarized in table 6.5. The relation between the porosity and the relative permeability due to the porosity is assumed to be:

$$k_{\mathrm{rel,n}} = 97n + 0.1 \tag{6.3}$$

Parameter	Unit	Elastic simulation	Elasto-plastic simulation
Young‘s modulus E	[kPa]	30.0	30.0
Poisson‘s ratio ν	[-]	0.2	0.2
Density ρ	[kg/m^3]	2000.0	2000.0
Initial porosity n_{IC}	[-]	0.05	0.05
Intrinsic permeability k	[m^2]	1.0$\cdot$ 10^{-11}	1.0$\cdot$ 10^{-11}
Cam-Clay parameter M	[-]	-	1.5
Preconsolidation p_c	[Pa]	-	1.0
Virgin compression index λ_{VCI}	[-]	-	0.5
Recompression index κ_{RCI}	[-]	-	0.05
Relative permeability due to porosity	[-]	equ. (6.3)	equ. (6.3)

Table 6.5: Material properties for the investigation of the impact of mechanical deformations on the strain dependent permeability.

6.5.2 Results

The displacements, the water pressure, the fluxes and the compressive volumetric strains due to the elastic simulation of the proposed example are presented in figure 6.14 by the deformed mesh, the contour plots and the vector field. The classical deformation in the area of the load can be observed here. As these compression strains are higher and concentrated on a small area, their impact has a more significant influence on the fluid flow, than the expansion strains which arise due to the pressure field. As expected, the deformation becomes asymmetric due to the pressure field as the water pressure implies an extension of the material. The resulting volumetric expansion strains depend quantitatively on the value of the water pressure and are higher on the left than on the right side of the example. Furthermore, the gradient of water pressure leads to smaller compressive strains due to the foundation plate on the left side than on the right side. The resulting volumetric strains affect the porosity and consequently the permeability of the material. The initially homogeneous pressure field and horizontal fluxes are modified. The resulting fluxes are presented in figure 6.14 on the bottom and indicate only low fluxes in the near field of the load.

The results for the same problem, simulated with an elasto-plastic material model are given in figure 6.15. It can be stated that the additional plastic volumetric strains finally lead

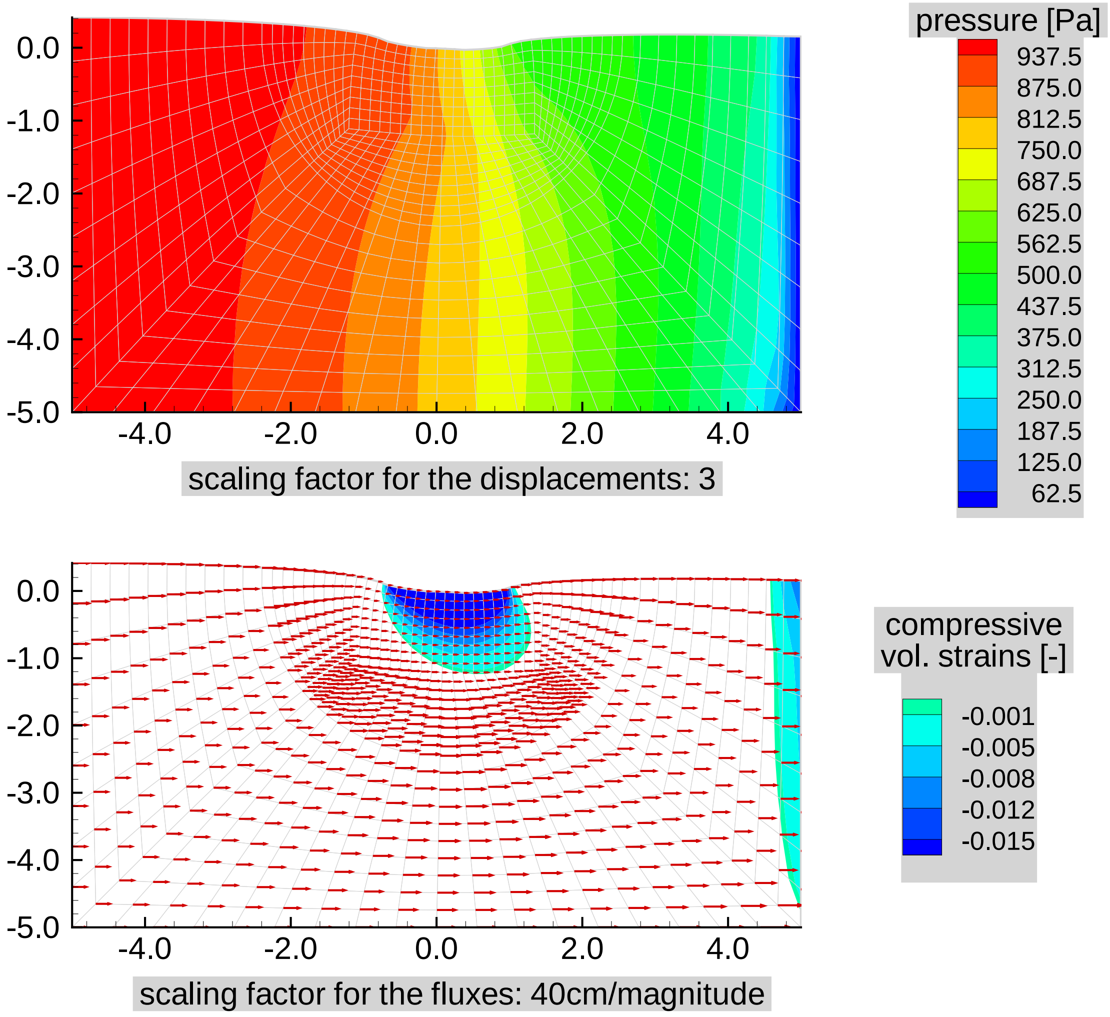

Figure 6.14: Displacements, water pressure, fluxes and compressive volumetric strains derived by the elastic simulation after 20 s.

to higher volumetric compression strains. The deformations in the near field of the load are higher than before and the area which is significantly influenced increases. Due to this area with volumetric compression strains the pressure gradient within this area increases and consequently decreases in the rest of the domain. As a consequence, the fluxes in great areas of the domain are lower than in the pure elastic case. In the area where the foundation plate directly leads to compression behavior, the steeper gradient and the lower permeability are nearly balanced and the fluxes are similar to the elastic example. Concerning this results, it has to be kept in mind, that the relation between porosity and relative permeability (given in equation 6.3) is assumed to be very steep for this example. But finally it can be stated that in the near field of the load the plastic effect has a significant impact on the mechanical as well as on the hydraulic process. The rest of the modeled domain is only influenced in a moderate way.

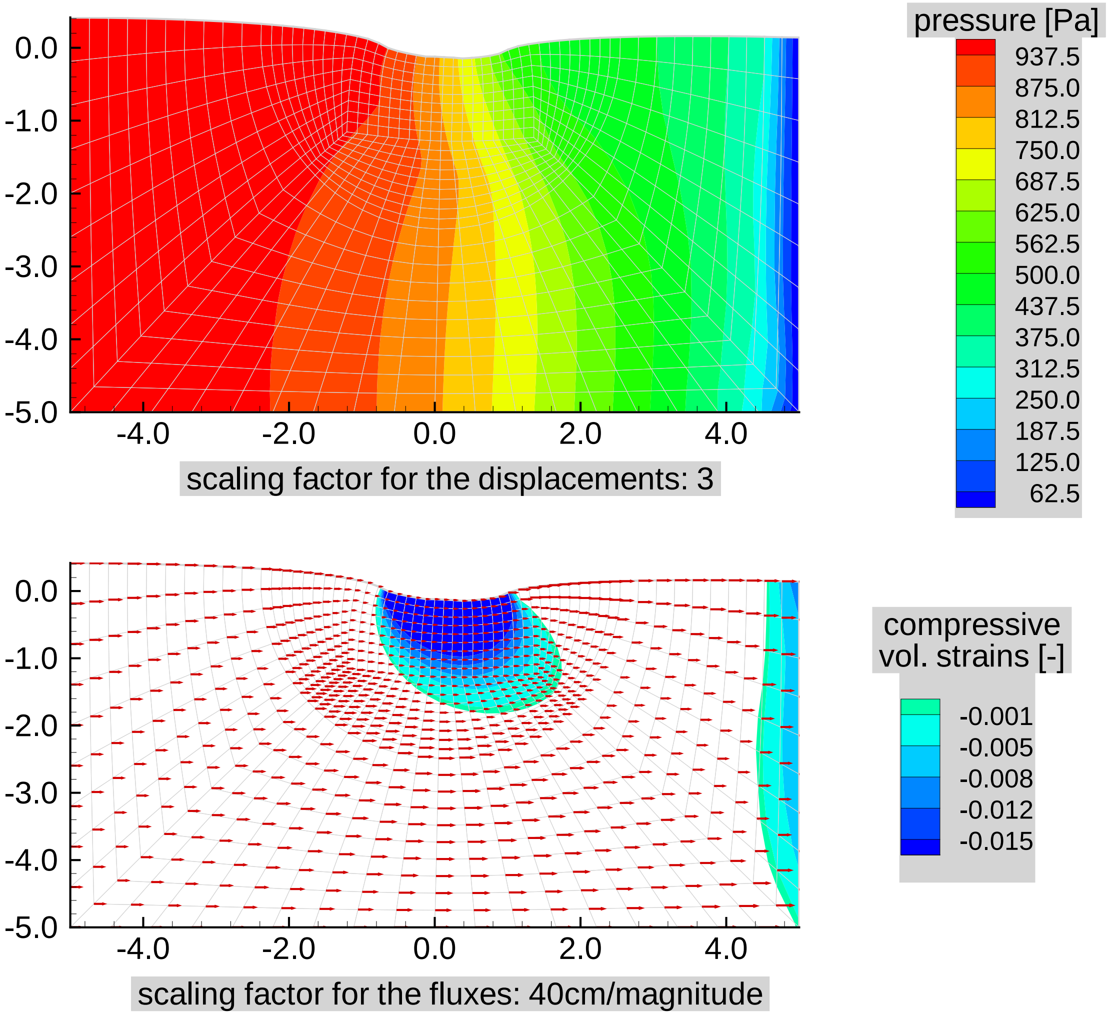

Figure 6.15: Displacements, water pressure, fluxes and compressive volumetric strains derived by the elasto-plastic simulation after 20 s.

As the permeability directly results from the volumetric strains and is the main variable concerning the hydraulic process, the relative permeabilities depending on the porosity for both cases are also presented in figure 6.16.

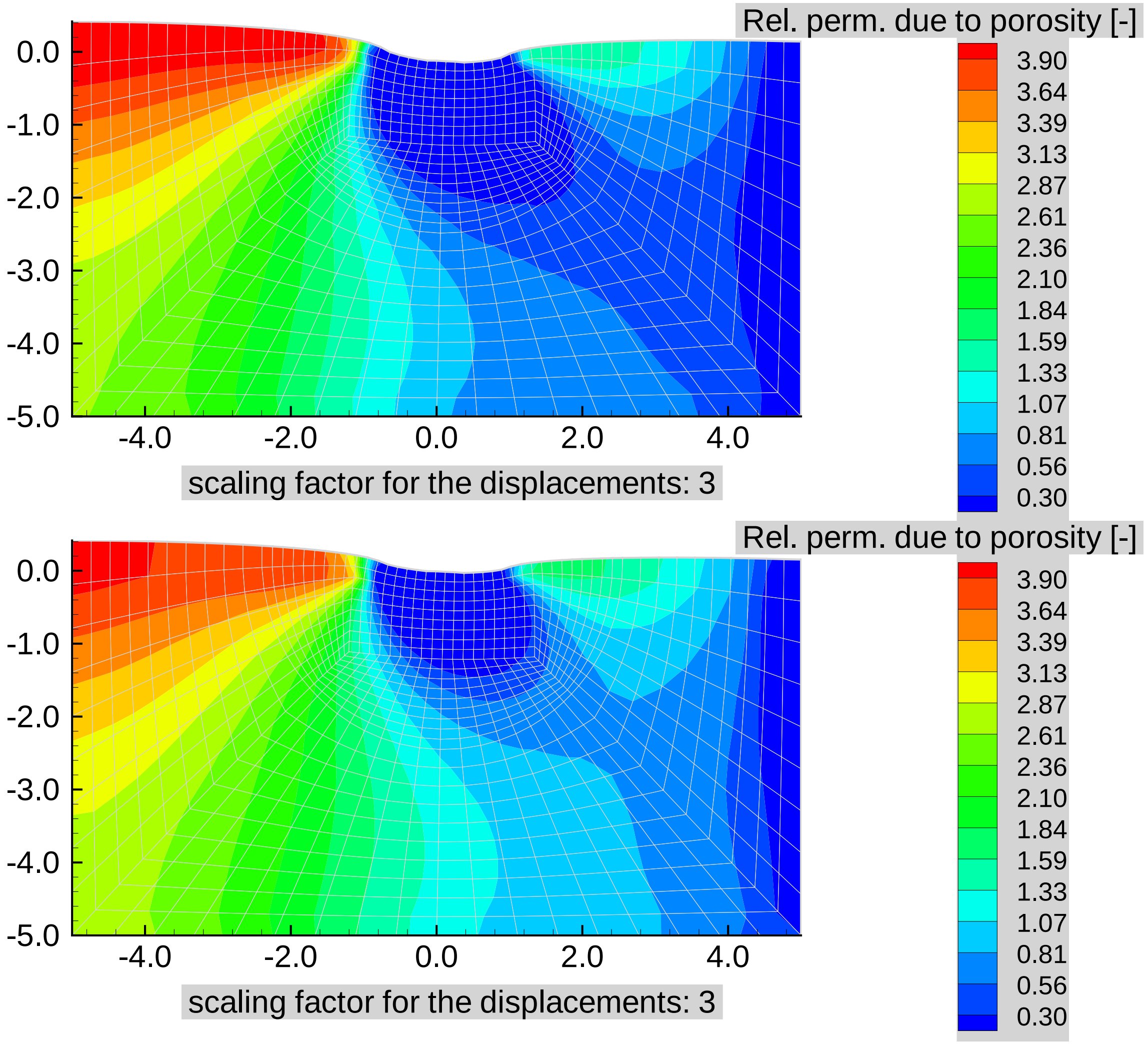

Figure 6.16: Relative permeability due to the porosity resulting from the elasto-plastic model (top) and the elastic simulation (bottom).

6.6 Strain dependent permeability due to swelling and shrinkage

The strain dependent permeability is affected by the mechanical deformation as well as by swelling and shrinkage effects of the clay material. While section 6.5 investigates the impact of mechanical deformations on the strain dependent permeability and the hydraulic process, this section focuses on a saturation dependent permeability.

6.6.1 Model setup

A variation of the saturation leads to volumetric swelling strains and consequently an impact on the hydraulic process in unsaturated media. This effect is investigated here. The model domain is assumed to have a width of 12.0 cm and a hight of 6 cm and is presented in figure 6.17 at the bottom. The domain is mechanically fixed at all sides. Furthermore, the initial saturation is given by 40% and an increase of the saturation up to 50% is applied at a width of 3.0 cm in the center of the top of the sample.

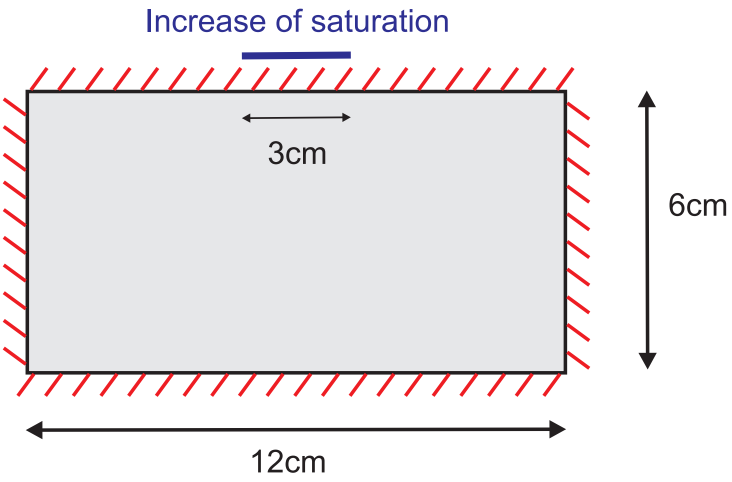

Figure 6.17: Model setup including the hydraulic (blue) and mechanical (red) subproblem.

The material properties are summarized in table 6.6 and the saturation boundary condition is given in figure 6.19. The capillary pressure depending on the saturation as well as the relative permeability depending on the saturation are given in figure 6.18. The relation between the porosity and the relative permeability due to the porosity are given by:

$$k_{\mathrm{rel,n}} = 10n \tag{6.4}$$

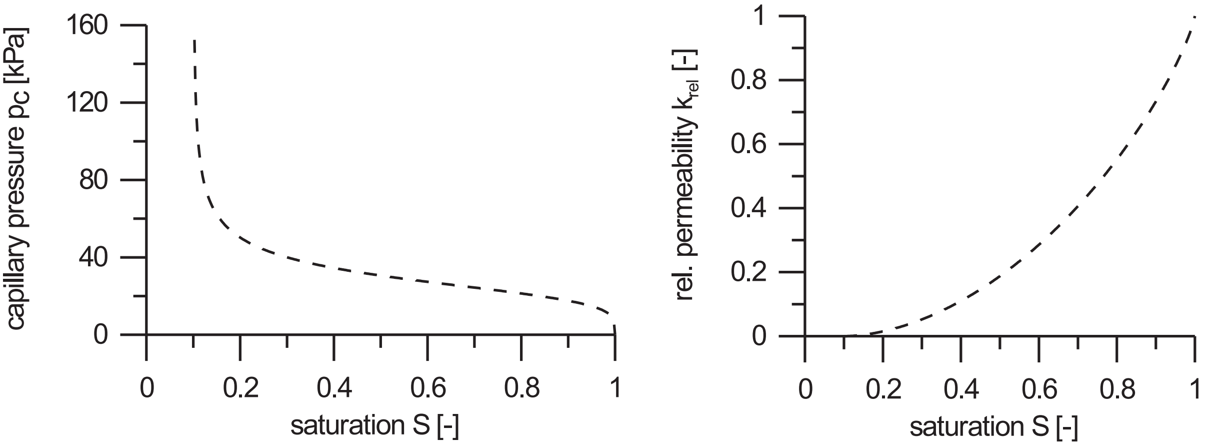

Figure 6.18: Capillary pressure (left) as well as the relative permeability (right) depending on the saturation.

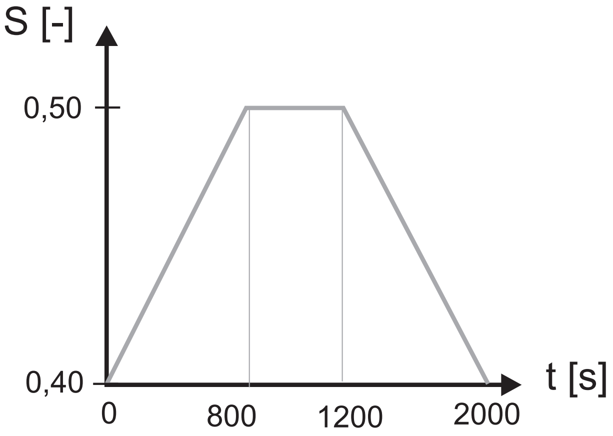

Figure 6.19: Saturation boundary condition at the center of the top of the sample.

6.6.2 Results

Within this example all boundaries are fixed. As the increase of the saturation at the top leads to some kind of swelling primarily in the near field of the fluid inflow, expansive volumetric strains arise in the whole domain. Consequently the material becomes less permeable especially in the center of the top. The swelling volumetric strains and the evoked volumetric strains are presented in figure 6.20 on a deformed mesh (scaling factor: 500). It can be seen, that the swelling strains are significantly higher than the volumetric strains arising due to the inhomogeneous stress field.

The updated porosity as well as the updated permeability are directly recalculated applying the volumetric strains. The resulting relative permeability due to the porosity (please refer to section 2.4.6) is presented in figure 6.21. The impact on the hydraulic process of a varying permeability due to swelling and shrinkage in an unsaturated material is already presented in

Parameter	Unit	Value
Young's modulus E	[kPa]	$7.0 \cdot 10^{6}$
Poisson's ratio ν	[-]	0.27
Density ρ	[kg/m^3]	2542.0
Initial porosity n_{IC}	[-]	0.11
Intrinsic permeability k	[m^2]	$1.0 \cdot 10^{-17}$
Capillary pressure related to saturation	[Pa]	fig. 6.18
Relative permeability due to saturation	[-]	fig. 6.18
Relative permeability due to porosity	[-]	equ. (6.4)
Volumetric swelling coefficient β^{sw}	[-]	0.175
Swelling model domain:		
Max. water saturation $S^{\mathrm{w}}_{\mathrm{max}}$	[-]	1.0
Min. water saturation $S^{\mathrm{w}}_{\mathrm{min}}$	[-]	0.1
Reference water saturation S^{w}_{0}	[-]	0.40
Volumetric reference strain $\varepsilon^{\mathrm{sw}}_{\mathrm{vol},0}$	[-]	0.0

Table 6.6: Material properties for the investigation of the impact of swelling and shrinkage on the strain dependent permeability.

section 6.7.5, especially in figure 6.27.

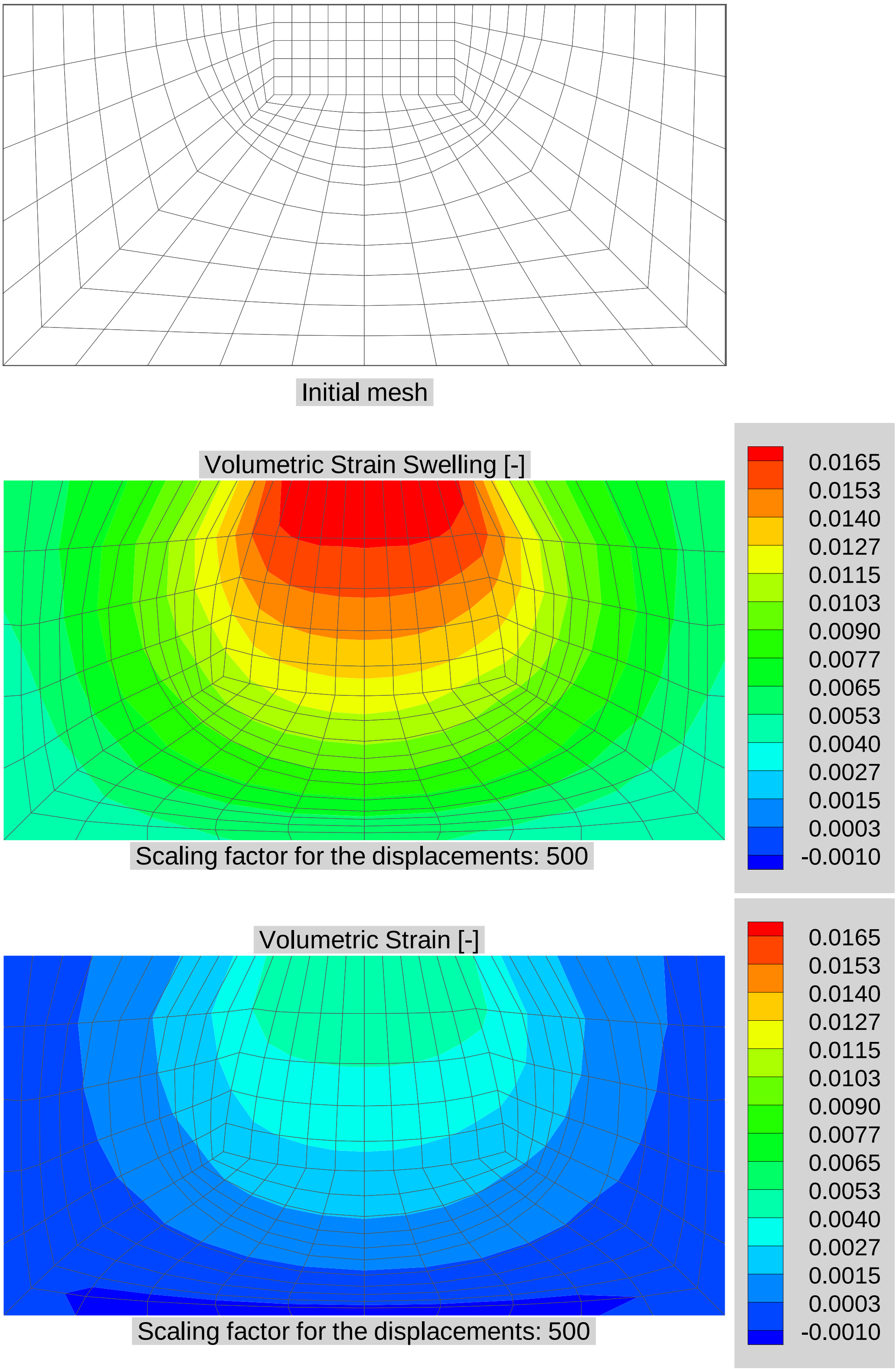

Figure 6.20: Initial mesh (top). Swelling volumetric strains (middle) and volumetric strains (bottom) shown on the deformed mesh.

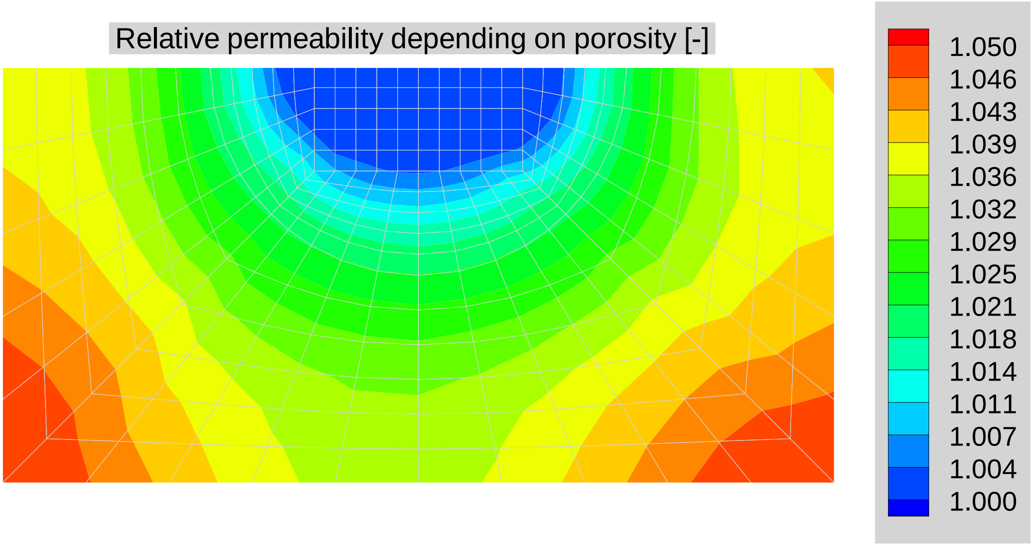

Figure 6.21: Resulting relative permeability due to the porosity for the saturation controlled example.

6.7 Migration test in a bentonite-sand-mixture („TDR experiment“)

It is planned to dispose high-level radioactive waste in underground repositories to be erected in very low permeable bedrock. Salt, clay and granite rock formations are of potential interest as the form a natural barrier due to their low conductivity. Besides this, an engineered barrier system (EBS) is planned. The investigation of the permeability of such a system is the aim of the gas migration test (GMT). This test is accomplished in the Felslabor Grimsel in Switzerland and comprises several experiments. One of the laboratory experiments is the TDR test which covers a long-term saturation process in a bentonite-sand mixture which is measured by several pressure cells and a TDR tube (time domain reflectometry), which causes the name TDR-test. Originally, this experiment was aimed to validate the TDR-measurements at high water contents. The measurements (TDR-signal, pressure, water volume and stress) are registrated since February 2002. Due to the well defined set–up including all boundary conditions and a comprehensive measuring instrumentation, the results of this experiment can be used to improve and validate the numerical model. This section presents the application of the finite element code RockFlow (Version 5) for the simulation of the TDR test. Starting with an introduction concerning the experimental design, the material properties and the model setup, the section gives an insight in the impact of various processes and the numerical simulation of the TDR-test. It finishes with the investigation of potentially higher permeabilities in the upper part and a summary.

6.7.1 Experimental design

Within the TDR test a cylindrical column of a bentonite-sand-mixture with the percentage of 20:80 is investigated (see figure 6.22). This soil column is surrounded by an impermeable and mechanically fixed metallic cylinder and has a height of 88 cm and a diameter of 20 cm. At the bottom of the bentonite-sand-mixture a layer of gravel is constructed, whereas the top is bordered by a metal plate with a small tube. The column contains different pressure cells, which are situated in three different heights. Measured from the top of the gravel they are located at 13.0 cm, 45.0 cm and 75.0 cm. Another measuring probe, called TDR, is adjusted in the central axis of the cylinder. The water injection takes place at the bottom of the column and is increased step-wise over a time period of about 4.5 years.

6.7.2 Model setup

Geometry

Caused by the one-dimensionality of the processes, the cylinder will be simplified to a mesh with a height of 0.88 m and a width of 0.02 m. It is divided in 176 quadratic elements with side-lengths of 0.01 m.

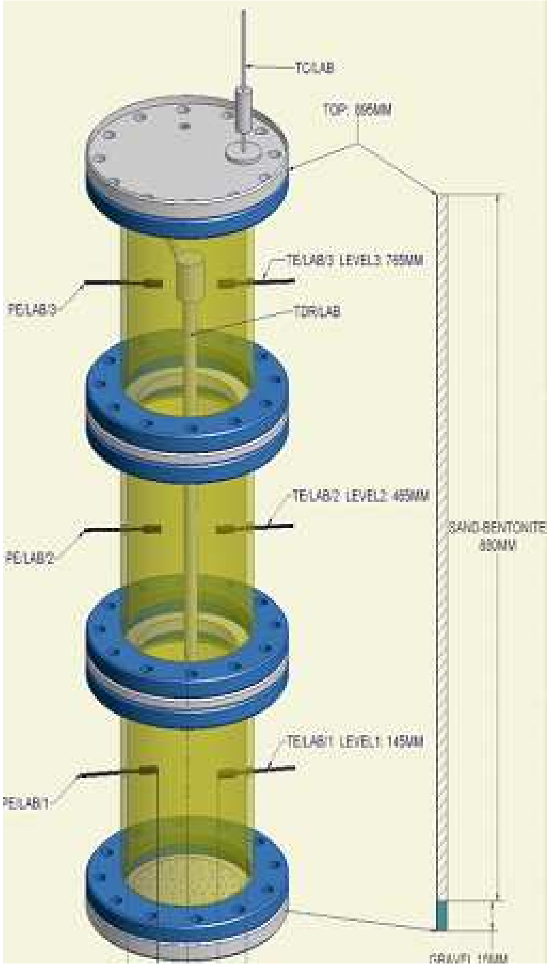

Figure 6.22: Experimental setup of the TDR test given in (QLR-Labtest, 2005).

Initial conditions

The simulation starts with a uniform saturation of 69% in the whole area. There are no initial stresses and the gravity constant g is assumed to be negligible.

Boundary conditions

All boundaries are mechanically fixed. The hydraulic boundary conditions are given by impermeable boundaries at the left and at the right. The bottom is build by a time-dependent pressure that initiates a saturation process (see figure 6.23). Special attention has to be paid to the hydraulic boundary condition at the top. In the experiment, the top of the bentonite-sand-mixture is covered by a metal plate. This plate contains a small tube, where water can flow out. Consequently, the numerical model features a closed boundary condition for the first phase of the experiment, which covers the saturation process and the evolution of a pressure field. When the pressure at the top comes to a positive range, the boundary condition at the top is set to zero. As a matter of fact, the water can flow out.

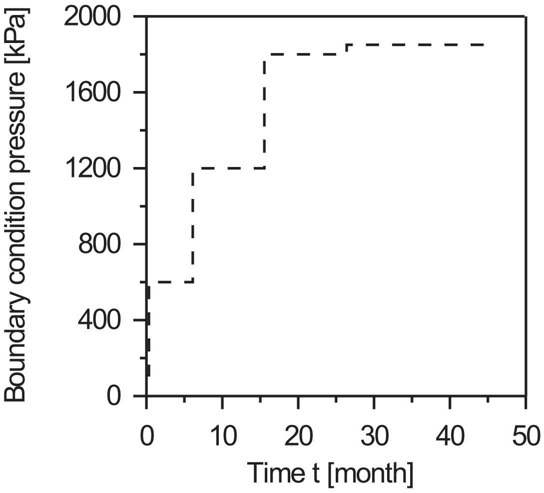

Figure 6.23: Pressure boundary condition at the bottom of the cylinder.

Hydraulic-mechanical coupling

The coupling from the hydraulic process to the mechanical problem is driven by some aspects, prescribed in chapter 2. For unsaturated material there exist high negative pressures especially at a low saturation level. For this situation the effect represented by Terzaghi‘ s approach vanishes. A modification of the effective stress law given in 2.4.2 is presented in (Lu & Likos, 2004). It incorporates an additional parameter, the effecive stress coefficient χ as a function of current and residual degree of water saturation S^{w} and S_r^{w} and the constant exponent κ

$$\chi = \left(\frac{S^{\mathrm{w}} - S_r^{\mathrm{w}}}{1 - S_r^{\mathrm{w}}} \right)^{\kappa} . \tag{6.5}$$

Equation (6.5) modifies to:

$$\boldsymbol{\sigma}_{\mathrm{tot}} = \boldsymbol{\sigma}_{\mathrm{eff}} - \alpha \chi p^{\mathrm{w}} \mathbf{1} \tag{6.6}$$

Various applications presented in (Massmann et al., 2007) indicate that this approach give reasonable results. The simulations are done with an exponent of κ=2.0.

6.7.3 Material properties

Within the GMT test, many in situ and laboratory tests have been carried out. As most of the material properties depend on the test conditions like water content, dry density, origin of the bentonite material and others, the results of these tests are directly related to the given experiment. Although the interpretation of these data have to be done carefully, some material properties of the bentonite-sand-mixture are relatively well known. Other values or dependencies which are needed for the numerical simulation like the coupling parameters have to be calibrated. The experiments leading to the material properties used here are published in various project reports (see for example (Marschall, Fukaya, Croise, Yamamoto, & Mayer, 2001), (Romero, Castellanos, & Alonso, 2003), (Romero, Garcia, & Alonso, 2003), (nagra04-01, 2004) and (Romero & Castellanos, 2004)).

Hydraulic conductivity and permeability

Various measurements of the hydraulic conductivity for a bentonite-sand mixture with a ratio of 20:80 are given in the various reports published by nagra. Depending on the experiment, the results are related to the flow direction, the dry density, the water content, the drainage and the pressure situation. Due to the summary of the experimental data given in (Marschall et al., 2001) a hydraulic conductivity of $5.0{\cdot}10^{-12}$ [m/s] is chosen for the simulations. This conforms to a permeability of $5.0{\cdot}10^{-19}$ [m^2].

Capillary pressure versus saturation

The relationship between capillary pressure and saturation has a significant influence on the saturation process. Relating results are generated within the „Kodoka Project: Suction Test on unsaturated Bentonite/Sand mixture“, which is referred to in (Marschall et al., 2001). Within this reference there are four measured saturations for given suctions [kgf/cm^2]. These are fittet to a van Genuchten model with van Genuchten α α_{vG}=0.209 [1/kPa], van Genuchten n n_{vG}=1.094 [-], a residual saturation S_{res}=0.0 and a maximum saturation S_{max}=1.0. The resulting relationship has a very steep gradient and consequently generates very steep saturation fronts. It is shown in 6.24. Mathematically this relationship is given in (SSSAJ1980, 1980) with

$$p_c\,[Pa] = -\frac{1}{\alpha} \cdot 1000 \cdot \left(S_{\mathrm{eff}}^{-\frac{1}{m}} - 1\right)^{\frac{1}{n}} \tag{6.7}$$

and

$$m = 1 - \frac{1}{n}. \tag{6.8}$$

The effective saturations result from

$$S_{\mathrm{eff}} = \frac{S^w - S_{\mathrm{res}}}{S_{\mathrm{max}} - S_{\mathrm{res}}}. \tag{6.9}$$

According to this results the report clearly points out that:

‚It should be noted that the fit was made only on the basis of the capillary pressure data and that no permeability data was available to validate it. Also the values of n given are close to the limit of validity of the van Genuchten model n>1. These values result in very large changes of liquid permeability at small values of gas saturation, which is not well supported by other relative permeability data.‘

Relative permeability versus saturation

Caused by the lack of data, there are no values given for the relative permeability curve in (Marschall et al., 2001). Although the difference of the gas permeability in contrast to the water permeability should be presented by a factor of 1000.

Consequently we assume a relationship given by

$$k_{rel} = S^3 \tag{6.10}$$

which is shown in figure 6.24.

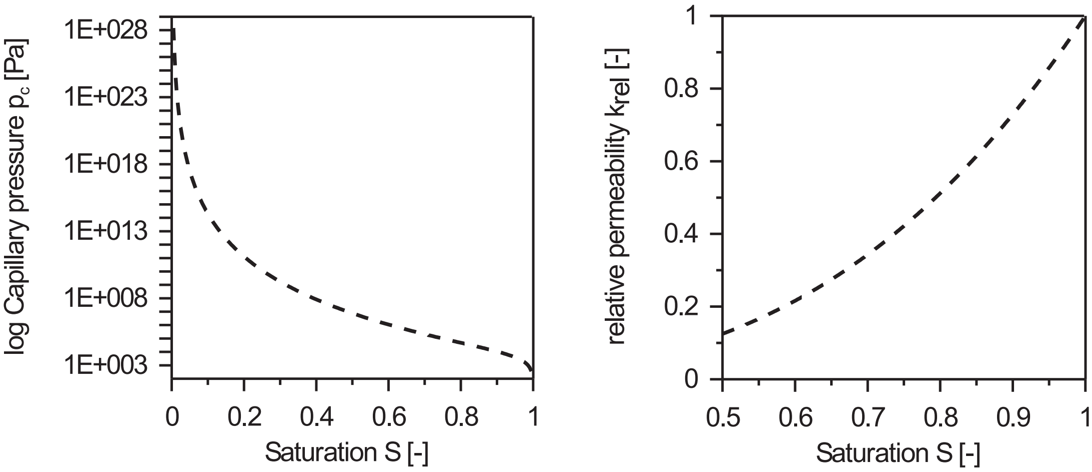

Figure 6.24: Capillary pressure versus saturation given in (left) and relative permeability versus saturation (right).

Swelling Model

The linear swelling model which is already presented in chapter 2 is used. The input parameters are taken from (Marschall et al., 2001) and presented in table 6.7. The swelling coefficient for the unsaturated case remains 0.016, while the coefficient for the saturated case is given by 0.029. The TDR-experiment starts with unsaturated conditions and a saturation process. However, the main part of the experiment is driven in saturated conditions. Consequently we chose a volumetric swelling coefficient of 0.029.

Summary of material properties for the numerical model

The presented properties are summarized in table 6.7.

Parameter	Unit	Value
Dry density assuming 0.11 Wc	[g/cm^3]	1.869
Initial porosity from dry density	[-]	0.296
Hydraulic conductivity	[m/s]	$9.2\cdot 10^{-13}$ up to $1.2\cdot 10^{-11}$
Intrinsic Permeability k	[m^2]	$5\cdot 10^{-19}$
Capillary pressure versus saturation		
van Genuchten α_{vG}	[1/kPa]	0.209
van Genuchten n$_{\mathrm{vG}}$	-	1.094
Residual saturation S$_{\mathrm{res}}$	-	0.0
Maximal saturation S$_{\mathrm{max}}$	-	1.0
Relative Permeability versus Saturation	[-]	$\frac{k_{\mathrm{rel,w}}}{k_{\mathrm{rel,g}}}$=1000
Linear swelling model		
volumetric swelling coefficient β^{sw}	-	0.029
max. water saturation $S^{\mathrm{w}}_{\mathrm{max}}$	-	1.0
min. water saturation $S^{\mathrm{w}}_{\mathrm{min}}$	-	0.5
reference water saturation S^{w}_{0}	-	0.69
volumetric reference strain $\varepsilon^{\mathrm{sw}}_{\mathrm{vol,0}}$	-	0.0
Young's modulus E	[Pa]	$50\cdot 10^6$
Poissons ratio ν	[-]	0.33

Table 6.7: Material properties for the TDR-test.

6.7.4 Investigating the impact of various processes

The prescribed saturation process is basically initiated by two different processes. On the one hand a typical saturation process, driven by the capillarity of the material takes place. On the other hand, the pore water pressure at the bottom of the cylinder has been increased step-wise, which also initiates a saturation process. Additionally, the influence of swelling and the strain dependent permeability have to be considered and will be introduced in the following.

Influence of the pressure boundary condition

A comparison of the saturation process in the bentonite-sand-mixture with and without a pressure boundary condition is given in figure 6.25. Here the pressure evolution over the height is given for every 3rd month. Due to the steep relation between capillary pressure and saturation, the saturation front is very steep. Comparing the velocity of the saturation process, it can be seen, that without any pressure boundary condition defined at the top, the saturation process is predicted to last more than four years. In contrast to that, the pressure prescription at the bottom leads to a speed up, which causes a fully saturation of the column after less than 2 years. As the pressure evolution also has a significant influence on the effective stresses in the column, a comparison of the stresses with and without the boundary condition are given in figure 6.25 at the bottom.

Influence of swelling

The swelling of the material is driven by the saturation and leads to an increase of strains and stresses in the cylinder. The hydraulic process and consequently the saturation of the column is not directly affected. A comparison of the stress- and strain-field with and without swelling are given in figure 6.26, where the total strains, resulting from the elastic strains and the swelling strains are pictured. On the left hand side, the results without the influence of swelling are given. The saturation leads to an increase of mass and consequently to an increase of stresses. During the saturation process, the effect follows up in a non-uniform strain and stress field, till the equilibrium condition is reached and a linear distribution of strains and stresses is reached.

The results due to the incorporation of swelling are presented on the right hand side. Qualitatively a similar evolution can be seen. Due to the swelling, which results in constant swelling strains over the height of the column, the process ends up with a stress field with higher compression and lower tensile stresses.

Influence of the strain dependent permeability

The investigation presented above consider the process of rising water content in a medium of unchanging pore structure while the hydraulic–mechanical coupling caused by the strain dependent permeability has not been incorporated yet. Thus, a permeability that depends on the strains in the column should be assumed as it is introduced in 2. Figure 6.27 shows the temporal evolutions of the pressure over the height compared with the results without this effect. It can be seen, that the change of permeability affects the part of the column that is already saturated. In this area, the permeability decreases and consequently the pressure increases. The major influence can be seen in the equilibrium case. In the bottom half positive strains occur (see figure 6.27). This leads to higher permeabilites and consequently a steeper pressure gradient. In the upper half the process takes place vice versa.

6.7.5 Simulation of the TDR-test

Incorporating all mentioned effects, the resulting pressure evolution is compared with the experimental data in in figure 6.29. The process at each point starts with a saturation of the material. Then, the pressure rises and the saturation front climbs the column. Finally, at a time of 58838400.0 sec or after 22.33 months, the saturation front reaches the top and the column is fully saturated. At this time, the pressure boundary condition at the top is changed to an open boundary. The water can flow out and the equilibrium state occurs.

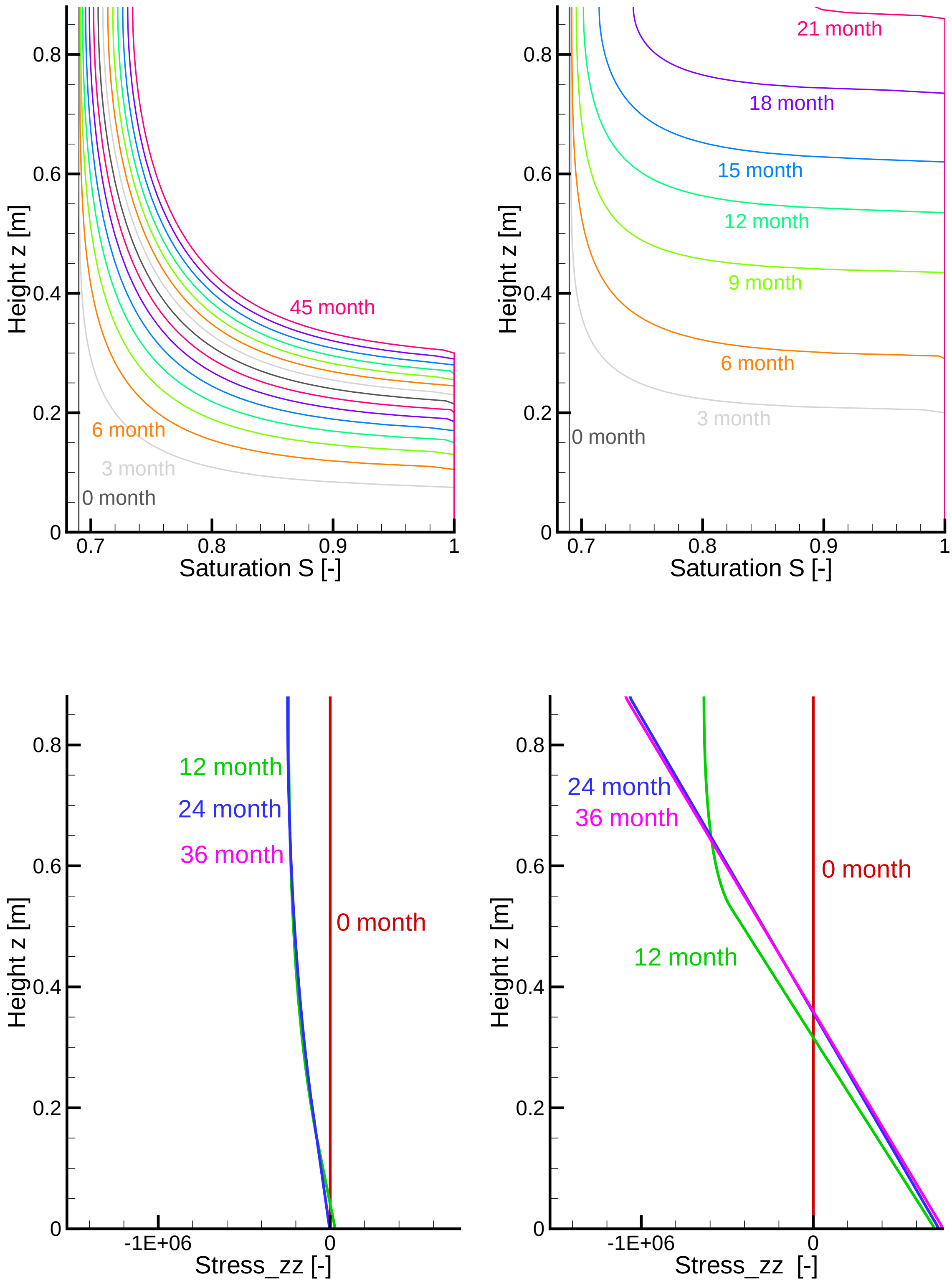

Figure 6.25: Temporal evolution of the saturation field (every 3rd month) on the top and the effective stress field on the bottom. Left: Results without a pressure boundary condition; right: Results with a pressure boundary condition.

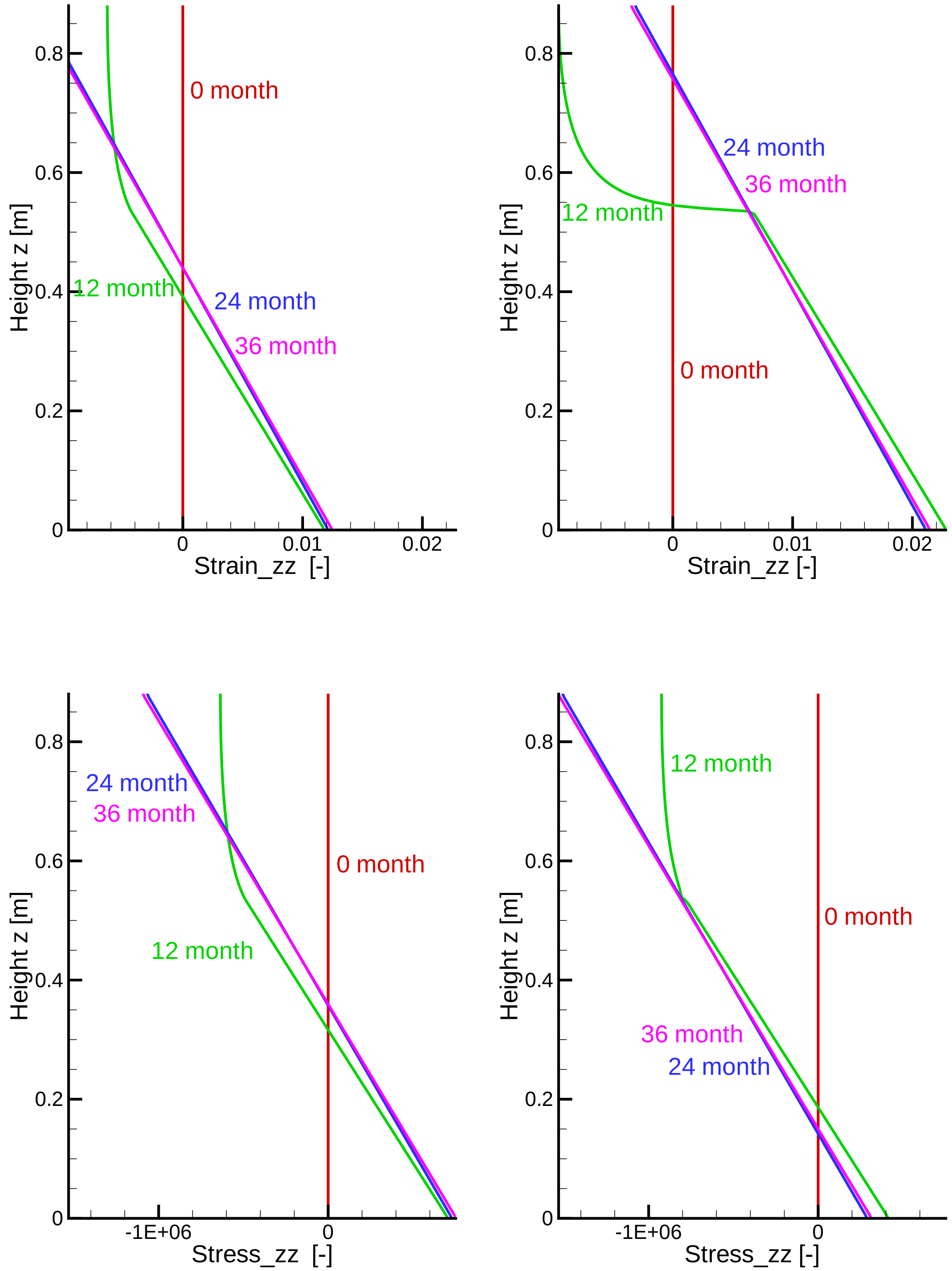

Figure 6.26: Temporal evolution of the stress and strain field with and without swelling of the material.

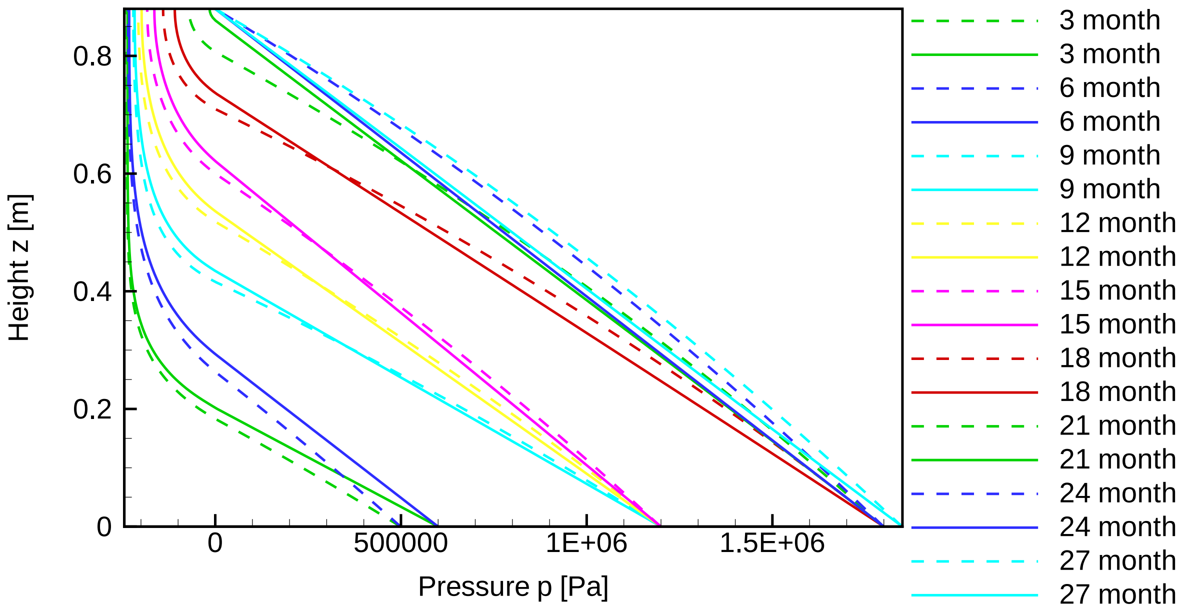

Figure 6.27: Temporal evolution of the pressure over the height (every 3rd month) with (dashed line) and without (solid line) the impact of the strain dependent permeability.

As can be seen, the simulation fits the measurements in the lower measuring point very well (red line). The pressures in the upper part of the column are overestimated by the numerical model. This might be the consequence of effects, which result from the high effective stresses in the upper part of of the column (see figure 6.26). These might lead to some kind of damage of the material which is not yet incorporated in the simulation (e.g. visco-elasto-plastic behavior, fracturing). Other effects like a saturation dependent Young's modulus or some kind of fingering are proven and show no significant change of the pressure evolution.

To validate the numerical model, the fluxes at the bottom derived by the measurements are compared to those of the numerical model. Figure 6.28 shows that the inflow rate is in the right range, whereas the temporal evolution can not be verified. Furthermore, the measured fluxes indicate the existence of an equilibrium condition primarily after the last increase of the pressure boundary condition. In contrast to that, the pressure measurements indicate equilibrium conditions after a relatively short time period after each step of pressure increase.

Finally, most of the effects, assumed to have an additional impact on the pressure evolution, result in a change of the pressure field in the whole column. But the simulation results fit the pressure in the lower part of the model very well. Consequently there might be other reasons, leading to the overestimation of the pressures in the upper part. Considering the effective stress field given in figure 6.26, one can assume that the existence of high compressive stresses might lead to some kind of damage and consequently higher permeabilities in the material. As the effective stresses in the upper part are higher than in the lower part, this would affect the upper parts primarily. Additionally, the upper part contains the TDR tube, which might include some kind of flow paths at the surface of the TDR tube. This kind of flow paths

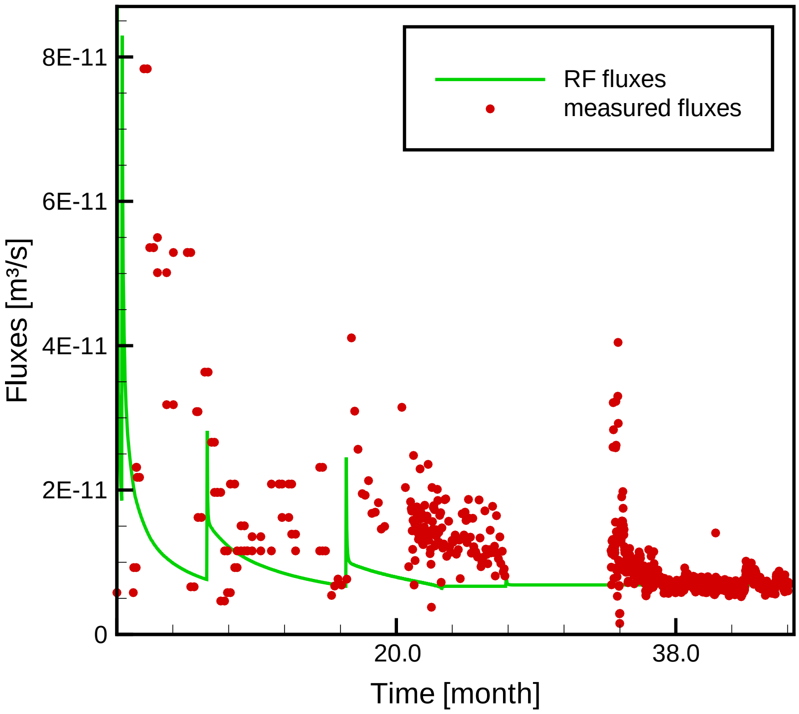

Figure 6.28: Comparison of the fluxes derived from the numerical simulation and the measurements.

lead to a higher permeability in these areas, resulting in lower pressures. This effect might also involve the pressure evolution. Additionally, the upper measurements (green and blue line) indicate the existence of nearly equilibrium conditions after the stepwise increase of the boundary condition. In contrast to that, the numerical model as well as the measured fluxes indicate a time-dependent behavior for a longer period after the increase of the pressure boundary condition. Assuming damage in the upper part or flow at the TDR surface would give an explanation of this difference.

6.7.6 Additional effect due to higher permeabilities in the upper part

As we assume some kind of damage (resulting in higher permeabilities in the upper part of the column) or a flow path at the surface of the TDR tube, another simulation, giving an insight of the influence of such an effect, is given here. As a first approach, we incorporate two material groups over the height. The area, which is covered with the TDR tube is assumed to be more permeable than the rest. Consequently, the first material group reaches from the bottom to the tip of the tube and indicates a permeability of $5{\cdot}10^{-19}\,\mathrm{m}^2$. The second material group covers the rest of the column and has a permeability of $1{\cdot}10^{-18}\,\mathrm{m}^2$. All other conditions

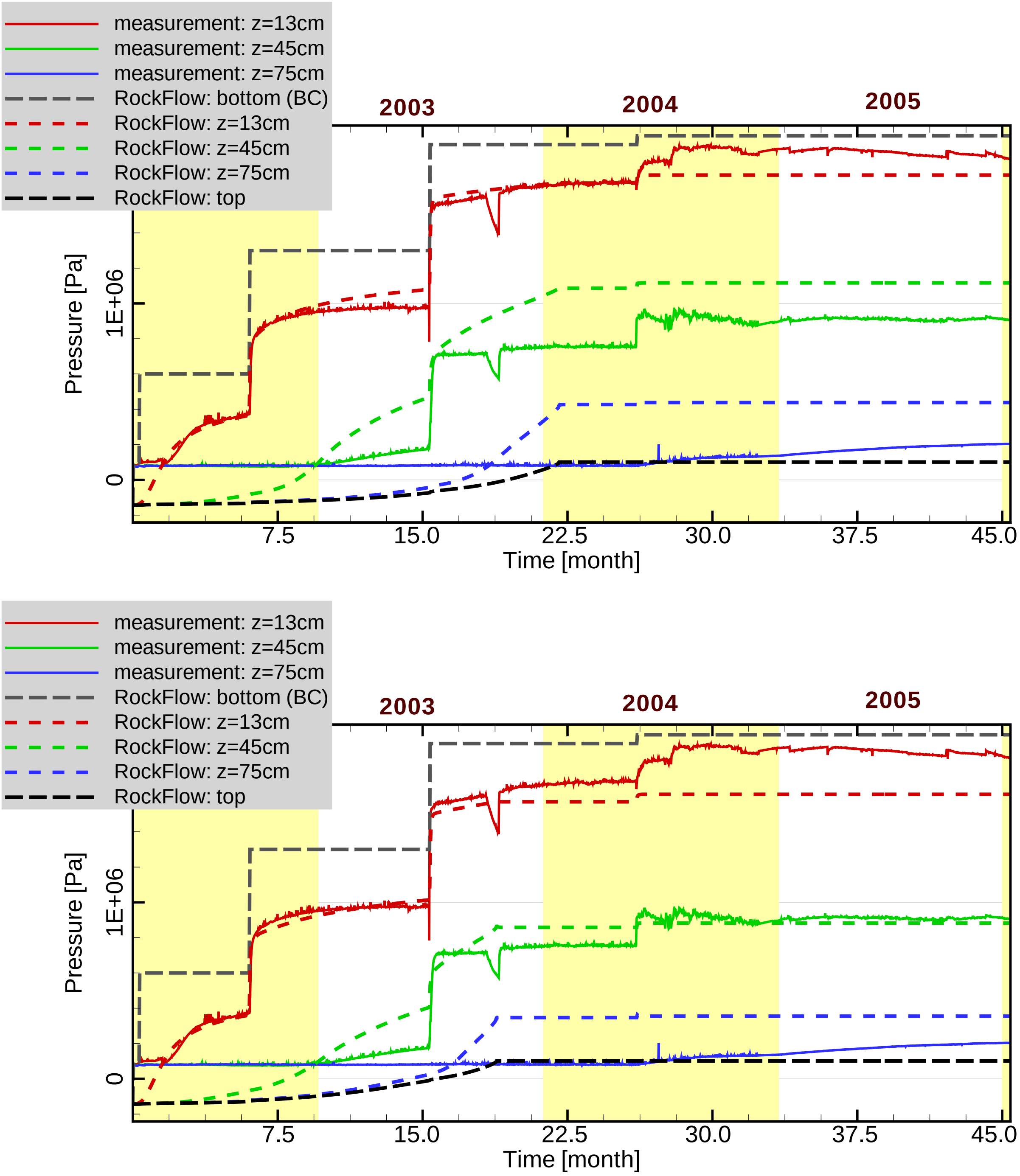

Figure 6.29: Temporal evolution of the pressure within the TDR-test compared with the measurements.
Top: Classical simulation as it is explained in section 6.7.5.
Bottom: Assuming a change of the permeability due to the TDR tube as it explained in section 6.7.6.

resemble the classical simulation of the TDR-test as it is presented in section 6.7.5.

The evolution of the pressure over the time is given in figure 6.29 at the bottom. Comparing the results with the previous ones, the equilibrium pressures in the upper points (green line and blue line) fit the measurements better than before, while the pressure in the lower part of the column is marginally lower than before and underestimates the measured data. Besides that the saturation time is shorter than in the previous simulation. Considering the approach, all these effects are comprehensive. The lower permeability in the upper part affects the lower measuring point since the saturation front has reached the area with lower permeabilities. It leads to a decrease of pressures and faster saturation times. However, assuming the existence of higher permeabilities in the upper part of the column might explain the existing equilibrium pressure field. The development of a numerical model which incorporates effects like damage of the material or some kind of micro-fractures could represent the pressure evolution in a more detailed way. A problem of a more complicated model like this are the unknown material properties like permeability of a material with plastic deformations, dimension of arising fractures, permeability of the fractures and others.

6.7.7 Discussion of the results

Due to the relation of capillary pressure and saturation the saturation front in the bentonite-sand mixture is relatively steep. Comparing a saturation process caused by capillarity with a process which additionally incorporates a pressure boundary condition, one can see the significant influence of the pressure at the bottom to the saturation time and the effective stresses. The investigation of the influence of swelling indicates, that the swelling leads to higher compressive and lower tensile stresses for the equilibrium stage. A non linear equilibrium pressure evolution is caused by the incorporation of a stress-dependent permeability.

The resulting pressure evolution fits the measured data quite well. There is a significant difference of the quality of the numerical results in the three different heights of the column. While the pressure in the lower measuring point fits the data very well, the results in the upper part of the column show some differences to the measured data. In contrast to the pressure measurements, the numerical simulation as well as the measured fluxes indicate a time-dependent effect after every increase of the pressure boundary condition till the equilibrium stage is reached. Finally, the simulated pressures overestimate the measured data.

These differences in the quality of the results indicate some additional effects in the upper part of the column. These might be induced by some kind of material damage due to high compressive stresses or an influence of the TDR tube, which might lead to some horizontal inhomogeneities. Further developments on the model setup might be a detailed model of the column, incorporating the TDR tube and possible flow path at their surface. Additionally, some more aspects of material modeling might be implemented. However, the impact of permeability changes as well as coupling parameters or a rough model to incorporate some kind of fingering due to the pressure boundary condition indicate only moderate influence. First investigations concerning a saturation dependent Young‘s modulus indicate only minor influence. Further developments incorporating the (saturation dependent) elasto-plastic material behavior, the effect of micro-fracturing or a non linear swelling model might be interesting.

Chapter 7

Conclusion

Within this work hydraulic–mechanical processes in clay materials are investigated numerically. Focusing on effects in compacted low permeable materials, the physical as well as the mathematical background and an algorithmic formulation are presented. The implemented processes are applied to various examples, analyzing the impact of the single processes on the mechanical and the hydraulic subproblem.

The investigation of coupled hydraulic-mechanical processes is part of current research in various fields of engineering applications. An important field is the modeling of high-level radioactive waste disposal, where the behavior of materials with low permeabilities is of special interest. In the near field of the radioactive waste an engineered barrier system (EBS) is build, which often contains clay materials like bentonite-sand-mixtures. Concerning the far field, various host rocks are supposable. Beside granite and salt, claystone is in the focus of current research. As a consequence the work at hand focuses on processes related to clay materials. The aim of the presented work is the investigation of specific effects within this kind of materials and their appraisement in consideration of the presented problem.

Starting point for this work was the existing coupled finite element code RockFlow which incorporates classical coupling phenomena. The classical coupling of the hydraulic-mechanical processes takes place in the incorporation of stress-induced strains in the mass balance of the fluid as well as in the application of Terzaghi's effective stresses and the saturation dependent parameters in the non linear material formulation.

The code is enhanced by algorithmic formulations to simulate effects related to the presented application field. More precisely the program is extended by additional mechanical effects and some coupling phenomena, which are of special interest for the simulation of migration problems in clay materials. The extensions of the finite element program RockFlow are tested within various applications. As expected, the investigations indicate that the extensions of the code significantly influence the mechanical behavior. Additionally they have an impact on the hydraulic process, whereas the significance strongly depends on the specific problem. In the following, the extensions as well as the related conclusions are shortly summarized.

As presented in chapter 2, clay material incorporates swelling and shrinkage, which is simulated by a linear swelling model that relates the saturation to some kind of volumetric swelling strain. The swelling and shrinkage as well as deformations affect the porosity of the material. Combining these effects with a strain dependent permeability, the impact on the hydraulic process can be modeled. Relating applications are presented in sections 6.5 and 6.6. The introduced strain dependent permeability turned out to be an effective tool to give an insight into the mechanical impact on the flow process. As it is formulated concise and without any need of inconvenient material parameters, it is already used in manifold applications.

Assuming the solid grains to be incompressible, the compression of the material is limited due to the existence of a compression point. As clay materials indicate very low porosities, already small deformations in the sense of the geometric linear theory lead to non linear elastic material behavior. The work at hand presents a purely mechanical approach to handle this nonlinearity in chapter 3. The coupling to the hydraulic process is done by the mentioned classical coupling phenomena. Typically, the proposed kind of problems contains a preconsolidated initial state, which significantly influences the constitutive behavior. As a consequence, the definition of a stress free porosity in contrast to the initial porosity is introduced in the compressibility model. The difference between stress free and initial porosity as well as the strength of the material have a significant influence on the evolution of stresses. Comparing the developed approach with experimental data indicates good agreements for various materials. The range of validity starts at low compression stresses and goes up to the compression point. The simulation of a step-wise compression test demonstrates the applicability. Investigations of the difference to the linear model and the impact of the initial state are presented in sections 6.1 and 6.2. It can be seen, that the non linear elastic compressibility model significantly influences the mechanical and the hydraulic process if the material is compressed and converges to the compression point. Additionally, it can be stated that materials with low permeabilities indicate high pressure gradients. As a consequence, the impact of the non linear compressibility model on the hydraulic process decreases for low permeable materials in relation to the impact of the permeabilities.

As it is already mentioned, high compression states arise in the proposed field of applications. Consequently, a pressure sensitive elasto–plastic material model is of special interest and is discussed in this work in chapter 4. It is incorporated into the numerical model by implementing a model of the Cam-Clay type, which is able to represent hardening and softening effects as well as plastic behavior due to a compression of the material. This kind of elasto–plastic material model needs only few material parameters which can be directly obtained from conventional laboratory experiments. Various modifications of this model are used in many scientific publications. Because of the presented strain dependence of the permeability, the arising plastic strains directly affect the hydraulic process. Various applications of this model are presented in sections 6.3, 6.4 and 6.5 and point out the hardening and softening behavior as well as the evolution of plastic strains and their impact onto the hydraulic process. But finally, the simulation of a coupled hydraulic-mechanical problem including elasto–plastic material behavior leads to an increase of the complexity of the model. Consequently, the impact on the results has to be thoroughly weighted. Further developments concerning the influence of the saturation and the pore space on the yield function might be of special interest within this field of application.

Other topics of future research arise directly from the processes presented in chapter 1, figure

1.1. They appear in the field of fracture mechanics as well as visco-elasto-plastic material behavior. Besides that, further developments focusing on geometrically non linear behavior, chemical effects including phase changes (non-isothermal multiphase flow) or reactive transport processes might be topics of future research.

Appendix A

Basic notations and definitions

A.1 Voigt Notation

The *Voigt notation* is a way to represent a symmetric tensor by reducing its order. The original presentation of e.g. the strains for the three dimensional case remains:

$$\boldsymbol{\varepsilon} = \begin{pmatrix} \varepsilon_{xx} & \varepsilon_{xy} & \varepsilon_{xz} \\ \varepsilon_{yx} & \varepsilon_{yy} & \varepsilon_{yz} \\ \varepsilon_{zx} & \varepsilon_{zy} & \varepsilon_{zz} \end{pmatrix}. \tag{A.1}$$

Reducing this in the sense of the Voigt notation leads to the following depiction:

$$\boldsymbol{\varepsilon}^T = \begin{pmatrix} \varepsilon_{xx} & \varepsilon_{yy} & \varepsilon_{zz} & \varepsilon_{xy} & \varepsilon_{yz} & \varepsilon_{xz} \end{pmatrix}. \tag{A.2}$$

A.2 Definition of the fourth order identity tensor I

The identity tensor of the fourth order is denoted as **I** and given by

$$\mathbf{I} = \begin{pmatrix} 1 & 0 & 0 & 0 & 0 & 0 \\ 0 & 1 & 0 & 0 & 0 & 0 \\ 0 & 0 & 1 & 0 & 0 & 0 \\ 0 & 0 & 0 & 0.5 & 0 & 0 \\ 0 & 0 & 0 & 0 & 0.5 & 0 \\ 0 & 0 & 0 & 0 & 0 & 0.5 \end{pmatrix}. \tag{A.3}$$

A.3 Definition of the second order identity tensor $\mathbf{1}$

The second order identity tensor is referred to as $\mathbf{1}$ and yields

$$\begin{pmatrix} 1 & 0 & 0 \\ 0 & 1 & 0 \\ 0 & 0 & 1 \end{pmatrix}. \tag{A.4}$$

Applying the Voigt notation yields

$$\mathbf{1} = \begin{pmatrix} 1 & 1 & 1 & 0 & 0 & 0 \end{pmatrix}^T = \mathbf{m}^T. \tag{A.5}$$

Therefore, it follows:

$$\mathbf{1} \otimes \mathbf{1} = \begin{pmatrix} 1 \\ 1 \\ 1 \\ 0 \\ 0 \\ 0 \end{pmatrix} \otimes \begin{pmatrix} 1 \\ 1 \\ 1 \\ 0 \\ 0 \\ 0 \end{pmatrix} = \begin{pmatrix} 1 & 1 & 1 & 0 & 0 & 0 \\ 1 & 1 & 1 & 0 & 0 & 0 \\ 1 & 1 & 1 & 0 & 0 & 0 \\ 0 & 0 & 0 & 0 & 0 & 0 \\ 0 & 0 & 0 & 0 & 0 & 0 \\ 0 & 0 & 0 & 0 & 0 & 0 \end{pmatrix}. \tag{A.6}$$

A.4 Euclidic norm

Within chapter 2 the vector norm $\| \bullet \|$ is used. This norm is also called Euclidic norm or L2-norm. It is applied for vectors and can be interpreted as a measure for the natural length of this vector. Concerning the vector $\mathbf{x}$ this norm yields:

$$\| \bullet \| = \sqrt{\sum_{i=1}^{n} |x_i|^2} \tag{A.7}$$

Other common norms are e.g. the L1-norm or the maximum norm.

A.5 Neumann number

Within section 5.1.3 the *Neumann number* is introduced as a measure to ensure the stability of a numerical solution procedure. Due to the Neumann number Ne, the algorithm is stable if

$$\mathsf{Ne} = \frac{D\Delta t}{\Delta x^2} \leq 0.5 \tag{A.8}$$

with the factor D.

A.6 Definition of the p-q-plane in the principal stress space

A common way to picture the yield function of a plastic material model is the presentation of the yield function in the p-q-plane. Within this description, p gives the hydrostatic axis where the mean stress occurs and q represents the axis of the deviatoric stresses. Figure A.1 gives a presentation of the p- and the q-axis in the principal stress space.

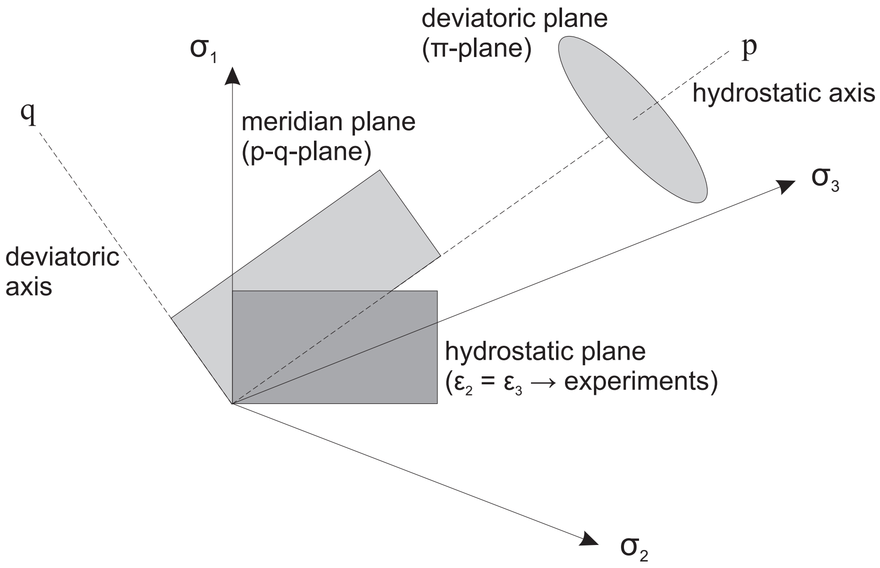

Figure A.1: Basic definitions of stress spaces.

Within this approach the radial distance from the space diagonal to an arbitrary stress point is given by $\sqrt{\frac{2}{3}}q$, as it is more precisely derivated in (Davis & Selvadurai, 2002).

A.7 The Euclidean space

Euclidean space *Around 300 before christ, the Greek mathematician Euclid laid down the rules of what has now come to be called „Euclidean geometry", which is the study of the relationships between angles and distances in space. Euclid first developed „plane geometry" which dealt with the geometry of two-dimensional objects on a flat surface. He then went on to develop „solid geometry" which analyzed the geometry of three-dimensional objects. All of the axioms of Euclid have been encoded into an abstract mathematical space known as a two- or three-dimensional Euclidean Space. These mathematical spaces may be extended to apply to any dimension, and such a space is called an n-dimensional Euclidean space or an n-space. (taken from Wikipedia.de)*

A.8 The Lebesgue integral

The Riemann integral is defined as the sum of the surface area of a series of step functions. In contrast to the Riemann integral, the Lebesgue integral is defined as the sum of a series of horizontal domains, converging to the integral of a function.

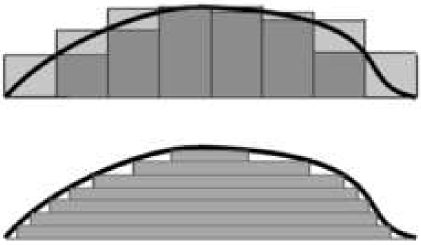

Figure A.2: Illustration of a Riemann integral (top) and a Lebesgue integral (bottom) (taken from Wikipedia.de)

Bibliography

Alonso, E., Gens, A., & Josa, A. (1990). A constitutive model for partially saturated soils *Geotechnique*(40), 405-430.

Alonso, E., Vaunat, J., & Gens, A. (1999). Modelling the mechanical behaviour of expansive clays *Eng. Geol.*(54), 173-183.

Barlag, C. (1997). Adaptive Methoden zur Modellierung von Stofftransport und Kluftgestein. Institut für Strömungsmechanik und Elektronisches Rechnen im Bauwesen, Universität Hannover. (PhD thesis)

Bathe, K.-J. (1996). Finite Element Procedures. Prentice Hall, Englewood Cliffs.

Bear, J. (1972). Dynamics of Fluids in Porous Media. Elsevier, New York.

Bear, J., & Verruijt, A. (1987). Modeling Groundwater Flow and Pollution. D.Reidel Publishing Company.

Belytschko, T., Liu, W., & Moran, B. (2003). Nonlinear Finite Elements for Continua and Structures. Wiley.

Borja, R., & Kavazanjian, J. E. (1985). A constitutive model for the stress-strain behavior of ‚wet‘ clays *Geotechnique*(35-3), 283-298.

Borja, R., Sama, K., & Sanz, P. (2003). On the numerical integration of three–invariant elastoplastic constitutive models *Computer methods in applied mechanics and engineering*(192), 1227-1258.

Borja, R. I., & Lee, S. R. (1990). Cam-Clay Plasticity, Part I: Implicit integration of elasto-plastic constitutive relations *Computer Methods in Applied Mechanics and Engineering*(78), 49-72.

Carter, J., Booker, J., & Small, J. (1979). The analysis of finite elasto-plastic consolidation *International Journal for Numerical and Analytical Methods in Geomechanics*(3), 107-129.

Carter, J., Booker, J., & Wroth, C. (1982). A Critical State Soil Model for Cyclic Loading Wiley and Sons Ltd. (Soil Mechanics - Transient and Cyclic Loads)

Chen, W., & Baladi, G. (1985). Soil Plasticity - Theory and Implementation. Elsevier.

Cramer, H., Findeiss, R., Steinl, G., & Wunderlich, W. (1999). An approach to the adaptive finite element analysis in associated and non-associated plasticity considering localization phenomena *Computer Methods in Applied Mechanics and Engineering*, *176*, 187-202(16).

Davis, R., & Selvadurai, A. (1996). Elasticity and Geomechanics. Cambridge University Press.

Davis, R., & Selvadurai, A. (2002). Plasticity and Geomechanics. Cambridge University Press.

de Boer, R. (2000). Theory of Porous Media - Highlights in Historical Development and Current State. Springer Verlag.

de Boer, R., & Ehlers, W. (1986). Theorie der Mehrkomponentenkontinua mit Anwendung auf bodenmechanische Probleme *Forschungsberichte aus dem Fachbereich Bauwesen*(40).

Desai, C., & Siriwardane, H. (1984). Constitutive laws for engineering materials with emphasis on geologic materials. Prentice-Hall.

Desai, C. S. (1989). Single surface yield and potential function plasticity models: A review. *Computers and Geotechnics*(7), 319-335.

Doll, S. (1998). Zur numerischen Behandlung grosser elasto-viskoplastischer Deformationen bei isochor-volumetrisch entkoppeltem Stoffverhalten. Institut für Mechanik der Universität Karlsruhe. (PhD thesis)

Drucker, D. C., & Prager, W. (1952). Soil mechanics and plastic analysis of limit design. *Appl. Math.*(10), 157-165.

Eekelen, H. v. (1980). Isotropic yield surfaces in three dimensions for use in soil mechanics *Int. Jnl. Num. Anal. Meth. Geomech.*(4), 89-101.

Ehlers, W. (1989). Poröse Medien: ein kontinuumsmechanisches Modell auf der Basis der Mischungstheorie *Forschungsberichte aus dem Fachbereich Bauwesen*(47).

Ehlers, W. (1991). Toward finite theories of liquid-saturated elasto-plastic porous media. *Int. J. Plasticity*(7), 433-475.

Ehlers, W. (1995). A single surface yield function for geomaterials *Archive of Applied Mechanics*(65), 246-259.

Ehlers, W., & Bluhm, J. (Eds.). (2002). Porous Media - Theory, Experiments and Numerical Applications. Springer Verlag.

Eipper, G. (1998). Theorie und Numerik finiter elastischer Deformationen in fluidgesättigten porösen Festkörpern. Institut für Mechanik der Universität Stuttgart. (PhD thesis)

Feldmann, D. (2001). Repetitorium der numerischen Mathematik. Binomi Verlag.

Findeiss, R. (2000). Ein orts- und zeitadaptives Finite-Element-Verfahren zur Traglastanalyse wassergesättigter Böden. Lehrstuhl für Statik der Technischen Universität München. (PhD thesis)

Gens, A., & Alonso, E. (1992). A framework for the behaviour of unsaturated expansive clays *Canadian Geotechnical Journal*(29), 1013-1032.

Gens, A., Jouanna, P., & Schrefler, B. (2002). Modern issues in non-saturated soils. Springer-Verlag.

Habbar, A. (2001). Direkte und Inverse Modellierung reaktiver Transportprozesse in klüftig-porösen Medien. Institut für Strömungsmechanik und Elektronisches Rechnen im Bauwesen, Universität Hannover. (PhD thesis)

Haupt, P. (2002). Continuum Mechanics and Theory of Materials. Springer.

Helmig, R. (1993). Theorie und Numerik der Mehrphasenströmungen in geklüftet-porösen Medien. Institut für Strömungsmechanik und Elektronisches Rechnen im Bauwesen, Universität Hannover. (PhD thesis)

Hughes, T. (2000). The Finite Element Method. Dover.

QLR Labtest 01/02/05. (2005).

Kaiser, R. (2001). Gitteradaption für die Finite-Elemente-Modellierung gekoppelter Prozesse in geklüftet-porösen Medien. Institut für Strömungsmechanik und Elektronisches Rechnen im Bauwesen, Universität Hannover. (PhD thesis)

Kim, M. K., & Lade, P. V. (1988). Single hardening constitutive model for frictional materials, I. Plastic potential function. Computers and Geotechnics*(5), 307-324.*

Knabner, P., & Angermann, L. (2003). Numerical Methods for Elliptic and Parabolic Partial Differential Equations. Springer.

Kohlmeier, M. (2006). Coupling of thermal, hydraulic and mechanical processes for geotechnical simulations of partially saturated porous media. Institut für Strömungsmechanik und Elektronisches Rechnen im Bauwesen, Universität Hannover. (PhD thesis)

Kolditz, O. (1996). Stoff- und Wärmetransport im Kluftgestein. Institut für Strömungsmechanik und Elektronisches Rechnen im Bauwesen, Universität Hannover. (Habilitation)

Kolditz, O. (2002). Computational Methods in Environmental Fluid Mechanics. Springer Berlin.

Kozeny, J. (1927). Über kapillare Leitung des Wassers im Boden (Aufstieg, Versickerung und Anwendung auf die Bewässerung) Sitzungsberichte der Akademie der Wissenschaften in Wien, mathematisch-naturwissenschaftliche Klasse*(136), 271-309. (Abteilung IIa)*

Kröhn, K.-P. (1991). Simulation von Transportvorgängen im klüftigen Gestein mit der Methode der Finiten Elemente. Institut für Strömungsmechanik und Elektronisches Rechnen im Bauwesen, Universität Hannover. (PhD thesis)

Lade, P., & Duncan, J. (1975). Elasto-plastic stress-strain theory for cohesionless soil ASCE, GT Div.*(101), 1037-1053.*

Lewis, R., & Schrefler, B. (2000). The finite element method in the static and dynamic deformation and consolidation of porous media. Second edition, John Wiley & Sons.

Liu, M., & Carter, J. (2002). A Structured Cam Clay Model Research Report, University of Sydney*(R814).*

Lu, N., & Likos, W. (2004). Unsaturated soil mechanics. Wiley.

Malcherek, A. (2001). Hydromechanik der Fliessgewässer. (Habilitation)

Marschall, P., Fukaya, M., Croise, J., Yamamoto, S., & Mayer, G. (2001). Project Report 00-20 GMT/IR 00-01: Laboratory data compilation report. National Cooperative for the Disposal of Radioactive Waste (nagra).

Massmann, J., Ziefle, G., Kohlmeier, M., & Zielke, W. (2007). Excavation Disturbed Zone (EDZ) in the Argillaceous Tournemire Site (France). Institute of Fluid Mechanics and Computer Applications in Civil Engineering, Leibniz Universität Hannover. (DECO-VALEX IV (THMC) - Task C - Report Part II)

Massmann, J., Ziefle, G., Kohlmeier, M., Zielke, W., & Shao, H. (2006). Coupled Hydro-mechanical Modeling of Seasonally Affected Unsaturated Claystone In GeoProc 2006 - 2nd International Conference on Coupld T-H-M-C Processes in Geo-systems: Fundamentals, Modeling, Experimens and Applications.

Matsuoka, H., & Nakai, T. (1974). Stress-deformation and strength characteristics of soil under three different principal stresses Proc. Jap. Soc. Civ. Eng*(232), 59-70.*

Mondol, N., Bjorlykke, K., Jahren, J., & Hoeg, K. (2007). Experimental mechanical compaction of clay mineral aggregates - changes in physical properties of mudstones during burial Marine and Petroleum Geology*. (doi:10.1016/j.marpetgeo.2007.03.006)*

Müllerschön, H. (2000). Spannungs- Verformungsverhalten granularer Materialien am Beispiel von Berliner Sand. Institut für Mechanik (Bauwesen), Universität Stuttgart. (PhD thesis)

Nackenhorst, U. (2003). Materialmodellierung. (Vorlesungsunterlagen)

Ortiz, M., & Pandolfib, A. (2004). A variational Cam-Clay theory of plasticity Computer Methods in Applied Mechanics and Engineering, 193*, 2645-2666. (Computational Failure Mechanics for Geomaterials)*

Panesso, J. (1998). Lokalisierung und Stabilität der Deformation wassergesättigter bindiger und granularer Böden. Institut für Baumechanik und Numerische Mechanik (IBNM), Universität Hannover. (PhD thesis)

Potts, D., & Gens, A. (1984). The effect of the plastic potential in boundary value problems involving plane strain deformation Int. Jnl. Num. Anal. Meth. Geomech.*(8), 259-286.*

Potts, D., & Zdravkovic, L. (2000). Some Pitfalls when using Modified Cam Clay. Imperial College, London, UK.

Project Opalinus Clay. (2002). National Cooperative for the Disposal of Radioactive Waste (nagra).

Project Report 04-01 GMT/SR 03-01: Summary report of the Fiscal Year 2003 activities. (2004). National Cooperative for the Disposal of Radioactive Waste (nagra).

Pusch, R., & Yong, R. N. (2006). Microstructure of Smectite Clays and Engineering Performance. Taylor and Francis.

Romero, E., & Castellanos, E. (2004). Project Report 04-07 GMT/IR 03-03: Complementary tests on compacted sand/bentonite/lead nitrate buffer material for the GMT Emplacement Project. National Cooperative for the Disposal of Radioactive Waste (nagra).

Romero, E., Castellanos, E., & Alonso, E. (2003). Project Report 02-24 GMT/IR 02-01: Laboratory tests on compacted sand/bentonite/lead nitrate buffer material for the GMT emplacement project. National Cooperative for the Disposal of Radioactive Waste (nagra).

Romero, E., Garcia, I., & Alonso, E. (2003). Project Report 03-03 GMT/IR 02-02: Laboratory gas tests on compacted sand-bentonite buffer material used in the GMT in-situ emplacement. National Cooperative for the Disposal of Radioactive Waste (nagra).

Roscoe, K., & Burland, J. (1968). On the generalized stress-strain behaviour of ‚wet ‘clay Engineering Plasticity, *535-609.*

Roscoe, K., Schofield, A., & Wroth, C. (1958). On the Yielding of Soils Geotechnique*(8), 22-53.*

Samingan, A. (2005). An Experimental Study on Hydro-Mechanical Characteristics of Compacted Bentonite-Sand Mixtures. Faculty of Civil Engineering, Bauhaus-University Weimar. (PhD thesis)

Schofield, A. (1993). Original Cam-clay Keynote lecture fot the International Conference on Soft Soil Engineering, Guangzhou.

Schofield, A., & Wroth, P. (1968). Critical State Soil Mechanics. McGraw-Hill, New York.

Shao, H. (1994). Simulation von Strömungs- und Transportvorgängen in geklüfteten porösen Medien mit gekoppelten Finite-Element- und Rand-Element-Methoden. Institut für Strömungsmechanik und Elektronisches Rechnen im Bauwesen, Universität Hannover. (PhD thesis)

Simo, J., & Hughes, T. (1998). Computational inelasticity Interdisciplinary Applied Mathematics, 7.

Simo, J., & Taylor, R. (1985). Consistent tangent operators for rate-independent plasticity Computer Methods in Applied Mechanics and Engineering, 48*(1), 101-118.*

Smith, I., & Griffiths, D. (2004). Programming the finite element method. Wiley. (4th edition)

Soil Science Society of America Journal (SSSAJ). (1980). (vol.44, page 894)

Starke, G. (2003). Numerik partieller Differentialgleichungen. (Vorlesungsunterlagen)

Starke, G. (2004). Methoden der numerischen Simulation. (Vorlesungsunterlagen)

Stein, E., & Barthold, F.-J. (1996). Elastizitätstheorie Der Ingenieurbau*(ISBN 3-433-01570-8), 165-428.*

Steinl, G. (2000). Ein adaptives Finite-Elemente-Verfahren zur Behandlung von Lokalisierungseffekten im Rahmen der Cosserat-Theorie. Technische Universität München, Lehrstuhl für Statik. (PhD thesis)

Stephansson, O., Jing, L., & Tsang, C.-F. (1996). Coupled Thermo-Hydro-Mechanical Processes of Fractured Media - Mathematical and Experimental Studies. Elsevier. (Recent Developments of Decovalex Project for Radioactive Waste Repositories)

Stührenberg, D. (2004). Compaction and Permeability Behaviour of Crushed Salt and Mixtures of Crushed Salt and Bentonite In DisTec 2004, International Conference on Radioactive Waste Disposal, Berlin.

Terzaghi, K. (1943). Theoretical soil mechanics. Wiley and Sons.

Terzaghi, K., & Fröhlich, O. (1936). Theorie der Setzung von Tonschichten - Eine Einführung in die analytische Tonmechanik. Franz Deuticke.

Thorenz, C. (2001). Model Adaptive Simulation of Multiphase and Density Driven Flow in Fractured and Porous Media. Institut für Strömungsmechanik und Elektronisches Rechnen im Bauwesen, Universität Hannover. (PhD thesis)

Truesdell, C., & Toupin, R. (1960). The classical field theories Handbuch der Physik, III/1, *226-793.*

Villar, M. (1995). First results of suction controlled oedometer test in highly expansive montmorillonite Proc. 1st Int. Conf. on Unsaturated Soils, Paris*(1), 207-213.*

Wollrath, J. (1990). Ein Strömungs- und Transportmodell für klüftiges Gestein und Untersuchungen zu homogenen Ersatzsystemen. Institut für Strömungsmechanik und Elektronisches Rechnen im Bauwesen, Universität Hannover. (PhD thesis)

Wriggers, P. (1986). Konsistente Linearisierungen in der Kontinuumsmechanik und ihre Anwendung auf die Finite-Elemente-Methode. Institut für Baumechanik und Numerische Mechanik, Leibniz Universität Hannover. (Habilitationsschrift)

Wriggers, P. (2001). Nichtlineare Finite-Elemente-Methoden. Springer.

Wulkau, M. (2005). Entwicklung einer Struktur- und Datenverwaltung zur objektorientierten Umsetzung eines flexiblen Konzepts der Dateneingabe im FE-Programm RockFlow. Institut für Strömungsmechanik und Elektronisches Rechnen im Bauwesen, Universität Hannover. (Studienarbeit)

Ziefle, G., Kohlmeier, M., Massmann, J., & Zielke, W. (2005). Excavation Disturbed Zone (EDZ) in the Argillaceous Tournemire Site (France). Institute of Fluid Mechanics and Computer Applications in Civil Engineering, Leibniz Universität Hannover. (DECOVALEX IV (THMC) - Task C - Report Part I)

Ziefle, G., Kohlmeier, M., & Zielke, W. (2004). Einbeziehung gekoppelter HM-Modellierung in die Materialbeschreibung teilgesättigter Medien. (5. Workshop ‚Porous Media', Blaubeuren)

Ziefle, G., Massmann, J., Kohlmeier, M., & Zielke, W. (2006). Modelling the interaction of stress-field and hydrodynamic properties in porous media. (6. Workshop ‚Porous Media', Blaubeuren)

Zienkiewicz, O., & Taylor, R. (2005). The Finite Element Method for Solid and Structural Mechanics. 6th edition, Elsevier.

List of Figures

1.1 Hydraulic and mechanical processes in clay materials. 3

1.1 RockFlow: State of the art 4

2.1 Porous medium simplified to a homogenized model. 8

2.2 Initial and current configuration and relating definitions. 10

2.3 Forces acting on the body. 16

2.4 Terzaghi's approach of effective stresses according to (Terzaghi, 1943) 20

2.5 Linear swelling model. 22

2.6 Modification of the initial porosity (left) due to deformation (center) and swelling (right). 23

2.7 Relationship of permeabiliy and porosity (left) and of permeability and saturation (right). 24

2.1 The linear boundary value problem (LBVP). 29

2.2 The common variational problem. 29

2.3 *Lax-Milgram-Lemma.* 29

3.1 Motivation for the development of the non linear elastic compressibility model for the geometric linear case. 35

3.2 Physical model for the compression of porous media without preconsolidation. 37

3.3 Physical model for the compression of porous media with preconsolidation. . . 37

3.4 Nonlinear elastic compressible material model. 39

3.5 Multiplication factor of the volumetric term related to $\operatorname{tr} \varepsilon^{\mathrm{vol}}$. 41

3.6 Relationship of stress and void ratio resulting from oedometer tests carried out on salt grit of the Asse mine. 44

3.7 Depth versa porosity found in the experiments compared with empirical relations (please refer to (Mondol, Bjorlykke, J., & K., 2007)). 46

3.8 Relation of compression stress and porosity of the non linear elastic compressibility model for various strength and stress free porosities. 46

3.9 Influence of the suction on the void ratio of highly compacted bentonite-sand mixtures given in (Samingan, 2005). 47

4.1 Von Mises plasticity (taken from (Davis & Selvadurai, 2002)). 50

4.2 Mohr-Coulomb (left) and Drucker-Prager plasticity in the principal stress space (taken from (Davis & Selvadurai, 2002)). 51

4.3 Comparison of the Mohr-Coulomb and the Drucker-Prager plasticity in the deviatoric plane. 51

4.4 Original Cam–Clay–Model (left) and modified Cam–Clay–Model (right) in the p-q-plane (taken from (Desai & Siriwardane, 1984)). 52

4.5 Plasticity model of the Cam-Clay type in the principal space (taken from (Desai & Siriwardane, 1984)). 52

4.6 Models with a single yield function proposed by (Ehlers, 1995) and (Findeiß, 2000) presented in the principal space. 53

4.7 Perfect plasticity. 54

4.8 Hardening plasticity with isotropic (left) and kinematic hardening (right). . . . 54

4.9 Porosity dependent yield function presented by (nagra-Opalinus, 2002). The yield surface is given in dependency on the void ratio e, the deviatoric stresses q‘ and the medial effective normal stresses p‘. 55

4.10 Saturation dependent plastic model presented by (Gens, Jouanna, & Schrefler, 2002). The yield surface is given in dependency on the suction s, the deviatoric stresses q and the medial effective normal stresses p. 55

4.11 Hardening behavior due to virgo- and reconsolidation. 60

5.1 Discretization of a geometry. 69

5.2 Procedure of the Newton iteration. 77

5.3 Procedure of the Picard iteration. 78

6.1 Geometry and load factor of the consolidation problem. 82

6.2 Pressure evolution [kPa] and resulting fluxes in the soil column between step 50 and 101. 84

6.3 Temporal evolution of the volumetric strains. Left: Linear model. Right: Non linear model. Top: Higher permeability leads to a low time-dependent impact. Bottom: Lower permeability leads to a high time-dependency. 85

6.4 Impact of the material model on the pressure evolution at different time steps for the simulation with the higher permeability. Left: Linear elastic model. Right: Non linear elastic model. Top: Steps 50 to 101. Middle: Steps 150 to 201. Bottom: Steps 450 to 501. 86

6.5 Pressure evolution over the column height resulting from a higher (left) and a lower (right) permeability. The pressure field is given for the steps 50 to 101. . 87

6.6 Resulting strains for the purely mechanical (left) and coupled hydraulic-mechanical (right) case. 89

6.7 Evolution of the pore space due to the compression of the preloaded sample. . 89

6.8 Load boundary condition at the top. 91

6.9 Over consolidation ratio (OCR) after 0.1 s. 91

6.10 Zone of plastification corresponding to 40%, 60%, 80% and 100% of the full value of the applied load and distribution of the OCR for the 100% load. . . . 92

6.11 Euclidic norm of the deviatoric stresses (top) and the plastic strains over the axial strain (bottom) for different M indicating softening. Left: RockFlow results. Right: Typical evolution taken from (Davis & Selvadurai, 2002). . . . 95

6.12 Euclidic norm of the deviatoric stresses and the plastic strains over the axial strain for different M indicating hardening. 96

6.13 Model setup for the elastic and elasto-plastic deformation example. Left: Hydraulic subproblem. Right: Mechanical subproblem. 97

6.14 Displacements, water pressure, fluxes and compressive volumetric strains derived by the elastic simulation after 20 s. 99

6.15 Displacements, water pressure, fluxes and compressive volumetric strains derived by the elasto-plastic simulation after 20 s. 100

6.16 Relative permeability due to the porosity resulting from the elasto-plastic model (top) and the elastic simulation (bottom). 101

6.17 Model setup including the hydraulic (blue) and mechanical (red) subproblem. . 102

6.18 Capillary pressure (left) as well as the relative permeability (right) depending on the saturation. 103

6.19 Saturation boundary condition at the center of the top of the sample. 103

6.20 Initial mesh (top). Swelling volumetric strains (middle) and volumetric strains (bottom) shown on the deformed mesh. 105

6.21 Resulting relative permeability due to the porosity for the saturation controlled example. 106

6.22 Experimental setup of the TDR test given in (QLR-Labtest, 2005). 108

6.23 Pressure boundary condition at the bottom of the cylinder. 109

6.24 Capillary pressure versus saturation given in (left) and relative permeability versus saturation (right). 111

6.25 Temporal evolution of the saturation field (every 3rd month) on the top and the effective stress field on the bottom. Left: Results without a pressure boundary condition; right: Results with a pressure boundary condition. 114

6.26 Temporal evolution of the stress and strain field with and without swelling of the material. 115
6.27 Temporal evolution of the pressure over the height (every 3rd month) with (dashed line) and without (solid line) the impact of the strain dependent permeability. 116
6.28 Comparison of the fluxes derived from the numerical simulation and the measurements. 117
6.29 Temporal evolution of the pressure within the TDR-test compared with the measurements.
Top: Classical simulation as it is explained in section 6.7.5.
Bottom: Assuming a change of the permeability due to the TDR tube as it explained in section 6.7.6. 118

A.1 Basic definitions of stress spaces. 127
A.2 Illustration of a Riemann integral (top) and a Lebesgue integral (bottom) (taken from Wikipedia.de) 128

List of Tables

6.1 Material properties for the step-wise compression test. 82
6.2 Material properties for the compression test on a preloaded sample. 88
6.3 Material properties for the simulation of the foundation problem. 90
6.4 Material properties for the simulation of the triaxial test. 94
6.5 Material properties for the investigation of the impact of mechanical deformations on the strain dependent permeability. 98
6.6 Material properties for the investigation of the impact of swelling and shrinkage on the strain dependent permeability. 104
6.7 Material properties for the TDR-test. 112

Liste der bisher erschienenen Institutsberichte

(* = bereits vergriffen)

01/1970 * **Holz, K.-P.** *Ergänzung des Verfahrens finiter Elemente durch Ecksingularitäten zur verbesserten Berechnung schiefwinkliger Platten.* Dissertation, Techn. Univ. Hannover, 1970

02/1971 * **Ehlers, K.-D.** *Berechnung instationärer Grund- und Sickerwasserströmungen mit freier Oberfläche nach der Methode finiter Elemente.* Dissertation, Techn. Univ. Hannover, 1971

03/1971 * **Meissner, U.** *Berechnung von Schalen unter großen Verschiebungen und Verdrehungen bei kleinen Verzerrungen mit Hilfe finiter Dreieckselemente.* Dissertation, Techn. Univ. Hannover, 1971

04/1972 * **Grotkop, G.** *Die Berechnung von Flachwasserwellen nach der Methode der finiten Elemente.* Dissertation, Techn. Univ. Hannover, Sonderdruck aus dem Jahresbericht 1971 d. SFB 79, H. 2, 1972

05/1973 * **Schulze, K.-W.** *Eine problemorientierte Sprache für die Dynamik offener Gerinne.* Dissertation, Techn. Univ. Hannover, Mitteil. d. SFB 79, Heft 1, 1973

06/1977 * **Beyer, A.** *Die Berechnung großräumiger Grundwasserströmungen mit Vertikalstruktur mit Hilfe der Finite–Element–Methode.* Dissertation, Fortschrittberichte der VDI–Zeitschriften, Reihe 4, Nr. 34, 1977

07/1977 * **Ebeling, H.** *Berechnung der Vertikalstruktur wind- und gezeitenerzeugter Strömungen nach der Methode der finiten Elemente.* Dissertation, Fortschrittberichte der VDI–Zeitschriften, Reihe 4, Nr. 32, 1977

08/1977 * **Gärtner, S.** *Zur Berechnung von Flachwasserwellen und instationren Transportprozessen mit der Methode der finiten Elemente.* Dissertation, Fortschrittberichte der VDI–Zeitschriften, Reihe 4, Nr. 30, 1977

09/1977 * **Herrling, B.** *Eine hybride Formulierung in Wasserständen zur Berechnung von Flachwasserwellen mit der Methode finiter Elemente.* Dissertation, Fortschrittberichte der VDI–Zeitschriften, Reihe 4, Nr. 37, 1977

10/1979 * **Hennlich, H.-H.** *Aeroelastische Stabilitätsuntersuchung von Linientragwerken.* Dissertation, Fortschrittberichte der VDI–Zeitschriften, Reihe 4, Nr. 49, 1979

11/1979 * **Kalocay, E.** *Zur numerischen Behandlung der Konvektions–Diffusions–Gleichung im Hinblick auf das inverse Problem.* Dissertation, Univ. Hannover, 1979

12/1980 * **Januszewski, U.** *Automatische Eichung für ein- und zweidimensionale, hydrodynamisch-numerische Flachwassermodelle.* Dissertation, Univ. Hannover, Fortschrittberichte der VDI–Zeitschriften, Reihe 4, Nr. 58, 1980

13/1982 * **Carbonel Huamán, C.A.A.** *Numerisches Modell der Zirkulation in Auftriebsgebieten mit Anwendung auf die nordperuanische Küste.* Dissertation, Univ. Hannover, 1982

14/1985 **Tuchs, M.** *Messungen und Modellierung am Deep Shaft.* Dissertation, Univ. Hannover, 1984

15/1985 **Theunert, F.** *Zum lokalen Windstau in Ästuarien bei Sturmfluten – Numerische Untersuchungen am Beispiel der Unterelbe.* Dissertation, Univ. Hannover, 1984

16/1985 **Perko, H.-D.** *Gasausscheidung in instationärer Rohrströmung.* Dissertation, Univ. Hannover, 1984

17/1985 **Crotogino, A.** *Ein Beitrag zur numerischen Modellierung des Sedimenttransports in Verbindung mit vertikal integrierten Strömungsmodellen.* Dissertation, Univ. Hannover, 1984

18/1985 **Rottmann–Söde, W.** *Ein halbanalytisches FE–Modell für harmonische Wellen zur Berechnung von Wellenunruhen in Häfen und im Küstenvorfeld.* Dissertation, Univ. Hannover, 1985

19/1985 **Nitsche, G.** *Explizite Finite–Element–Modelle und ihre Naturanwendungen auf Strömungsprobleme in Tidegebieten.* Dissertation, Univ. Hannover, 1985

20/1985 **Vera Muthre, C.** *Untersuchungen zur Salzausbreitung in Ästuarien mit Taylor'schen Dispersionsmodellen.* Dissertation, Univ. Hannover, 1985

21/1985 **Schaper, H.** *Ein Beitrag zur numerischen Berechnung von nichtlinearen kurzen Flachwasserwellen mit verbesserten Differenzenverfahren.* Dissertation, Univ. Hannover, 1985

22/1986 **Urban, C.** *Ein Finite–Element–Verfahren mit linearen Ansätzen für stationäre zweidimensionale Strömungen.* Dissertation, Univ. Hannover, 1986

23/1987 **Heyer, H.** *Die Beeinflussung der Tidedynamik in Ästuarien durch Steuerung – Ein Beitrag zur Anwendung von Optimierungsverfahren in der Wasserwirtschaft.* Dissertation, Univ. Hannover, 1987

24/1987 * **Gärtner, S.** *Zur diskreten Approximation kontinuumsmechanischer Bilanzgleichungen.* Institutsbericht, davon 4 Abschnitte als Habilitationsschrift angenommen, Univ. Hannover, 1987

25/1988 **Rogalla, B.U.** *Zur statischen und dynamischen Berechnung geometrisch nichtlinearer Linientragwerke unter Strömungs– und Wellenlasten.* Dissertation, Univ. Hannover, 1988

26/1990 * **Lang, G.** *Zur Schwebstoffdynamik von Trübungszonen in Ästuarien.* Dissertation, Univ. Hannover, 1990

27/1990 **Stittgen, M.** *Zur Fluid–Struktur–Wechselwirkung in flexiblen Offshore–Schlauchleitungen.* Dissertation, Univ. Hannover, 1990

28/1990 * **Wollrath, J.** *Ein Strömungs- und Transportmodell für klüftiges Gestein und Untersuchungen zu homogenen Ersatzsystemen.* Dissertation, Univ. Hannover, 1990

29/1991 **Kröhn, K.-P.** *Simulation von Transportvorgängen im klüftigen Gestein mit der Methode der Finiten Elemente.* Dissertation, Univ. Hannover, 1991

30/1991 **Lehfeldt, R.** *Ein algebraisches Turbulenzmodell für Ästuare.* Dissertation, Univ. Hannover, 1991

31/1991 * **Prüser, H.-H.** *Zur mathematischen Modellierung der Interaktion von Seegang und Strömung im flachen Wasser.* Dissertation, Univ. Hannover, 1991

dito * **Schröter, A.** *Das numerische Seegangsmodell BOWAM2 1990 – Grundlagen und Verifikationen – .* Univ. Hannover, 1991

32/1992 **Leister, K.** *Anwendung numerischer Flachwassermodelle zur Bestimmung von Wasserlinien.* Dissertation, Univ. Hannover, 1992

33/1993 **Ramthun, B.** *Zur Druckstoßsicherung von Fernwärmenetzen und zur Dynamik von Abnehmeranlagen.* Dissertation, Univ. Hannover, 1993

34/1993 * **Helmig, R.** *Theorie und Numerik der Mehrphasenströmungen in geklüftet–porösen Medien.* Dissertation, Univ. Hannover, 1993

35/1994 **Plüß, A.** *Netzbearbeitung und Verfahrensverbesserungen für Tidemodelle nach der Finiten Element Methode.* Dissertation, Univ. Hannover, 1994

36/1994 **Nöthel, H.** *Statistisch–numerische Beschreibung des Wellen- und Strömungsgeschehens in einem Buhnenfeld.* Dissertation, Univ. Hannover, 1994

37/1994 **Shao, H.** *Simulation von Strömungs- und Transportvorgängen in geklüfteten porösen Medien mit gekoppelten Finite–Element– und Rand–Element–Methoden.* Dissertation, Univ. Hannover, 1994

38/1994 **Stengel, T.** *Änderungen der Tidedynamik in der Deutschen Bucht und Auswirkungen eines Meeresspiegelanstiegs.* Dissertation, Univ. Hannover, 1994

39/1994 **Schubert, R.** *Ein Softwaresystem zur parallelen interaktiven Strömungssimulation und -visualisierung.* Dissertation, Univ. Hannover, 1994

40/1994 **Alm, W.** *Zur Gestaltung eines Informationssystems im Küsteningenieurwesen.* Dissertation, Univ. Hannover, 1994

41/1994 **Benali, H.** *Zur Kopplung von FEM– und CAD–Programmen im Bauwesen über neutrale Datenschnittstellen.* Dissertation, Univ. Hannover, 1994

42/1995 **Schröter, A.** *Nichtlineare zeitdiskrete Seegangssimulation im flachen und tieferen Wasser.* Dissertation, Univ. Hannover, 1995

43/1995 **Blase, Th.** *Ein systemtechnischer Ansatz zur Modellierung von Hydraulik, Stofftransport und reaktionskinetischen Prozessen in Kläranlagen.* Dissertation, Univ. Hannover, 1995

44/1995 **Malcherek, A.** *Mathematische Modellierung von Strömungen und Stofftransportprozessen in Ästuaren.* Dissertation, Univ. Hannover, 1995

45/1995 **Lege, T.** *Modellierung des Kluftgesteins als geologische Barriere für Deponien.* Dissertation, Univ. Hannover, 1995

46/1996 **Arnold, H.** *Simulation dammbruchinduzierter Flutwellen.* Dissertation, Univ. Hannover, 1996

47/1996 **Kolditz, O.** *Stoff- und Wärmetransport im Kluftgestein.* Habilitation, Univ. Hannover, 1996

48/1996 **Hunze, M.** *Numerische Modellierung reaktiver Strömungen in oberflächenbelüfteten Belebungsbecken.* Dissertation, Univ. Hannover, 1996

49/1996 **Wollschläger, A.** *Ein Random-Walk-Modell für Schwermetallpartikel in natürlichen Gewässern.* Dissertation, Univ. Hannover, 1996

50/1997 **Feist, M.** *Entwurf eines Modellierungssystems zur Simulation von Oberflächengewässern.* Dissertation, Univ. Hannover, 1997

51/1997 **Hinkelmann, R.** *Parallelisierung eines Lagrange–Euler–Verfahrens für Strömungs- und Stofftransportprozesse in Oberflächengewässern.* Dissertation, Univ. Hannover, 1997

52/1997 **Barlag, C.** *Adaptive Methoden zur Modellierung von Strofftransport im Kluftgestein.* Dissertation, Univ. Hannover, 1997

53/1997 **Saberi-Haghighi, K.** *Zur Ermittlung der verformungsabhängigen Windbelastung bei Hängedächern.* Dissertation, Univ. Hannover, 1997

54/1998 **Krüger, A.** *Physikalische Prozesse im Nachklärbecken – Modellbildung und Simulation.* Dissertation, Univ. Hannover, 1998

55/1998 **Wolters, A. H.** *Zur Modellierung des instationären thermohydraulischen Betriebsverhaltens von Fernwärmeanlagen.* Dissertation, Univ. Hannover, 1998

56/1999 **Jankowski, J. A.** *A non-hydrostatic model for free surface flows.* Dissertation, Univ. Hannover, 1999

57/1999 **Kopmann, R.** *Mehrdimensionale Effekte in dimensionsreduzierten Gewässergütemodellen.* Dissertation, Univ. Hannover, 1999

58/1999 * **Kahlfeld, A.** *Numerische Seegangsmodellierung als Bestandteil einer funktionellen Hafenplanung.* Dissertation, Univ. Hannover, 1999

59/1999 *Festschrift zum 60. Geburtstag von Prof. Dr.-Ing. Werner Zielke.* Univ. Hannover, 1999

60/2000 * **Kolditz, O., Zielke, W., Wriggers, P., Dürbaum, H.-J., Wallner, M.** *3. Workshop Kluft-Aquifere - Gekoppelte Prozesse in Geosystemen.* Univ. Hannover, 2000

61/2001 * **Malcherek, A.** *Hydromechanik der Fließgewässer.* Habilitation, Univ. Hannover, 2001

62/2001 **Thorenz, C.** *Model Adaptive Simulation of Multiphase and Density Driven Flow in Fractured and Porous Media.* Dissertation, Univ. Hannover, 2001

63/2001 **Kaiser, R.** *Gitteradaption für die Finite–Elemente–Modellierung gekoppelter Prozesse in geklüftet–porösen Medien.* Dissertation, Univ. Hannover, 2001

64/2001 **Rother, T.** *Geometric Modelling of Geo–Systems.* Dissertation, Univ. Hannover, 2001

65/2001 **Habbar, A.** *Direkte und inverse Modellierung reaktiver Transportprozesse in klüftig–porösen Medien.* Dissertation, Univ. Hannover, 2001

66/2002 * **Weilbeer, H.** *Strömung und Kolkung an Wasserbauwerken.* Dissertation, Univ. Hannover, 2002

67/2002 **Hoyme, H.** *Mesoskalige morphodynamische Modellierungen am Beispiel der Meldorfer Bucht.* Dissertation, Univ. Hannover, 2002

68/2004 **Moenickes, S.** *Grid generation for simulation of flow and transport processes in fractured porous media.* Dissertation, Univ. Hannover, 2004

69/2004 **Strybny, J.** *Ein phasenauflösendes Seegangsmodell zur Ermittlung von Bemessungsparametern für Küstenstrukturen.* Dissertation, Univ. Hannover, 2004

70/2004 **Weilbeer, J.** *Modellierung des Partikeltransports in Nachklärbecken als Mehrphasenströmung.* Dissertation, Univ. Hannover, 2004

71/2006 **Mittendorf, K.** *Hydromechanical Design Parameters and Design Loads for Offshore Wind Energy Converters.* Dissertation, Leibniz Universität Hannover, 2006

72/2006 **Kohlmeier, M.** *Coupling of thermal, hydraulic and mechanical processes for geotechnical simulations of partially saturated porous media.* Dissertation, Leibniz Universität Hannover, 2006

73/2006 **Schumacher, S.** *Leistungsbestimmende Prozesse in Nachklärbecken - Einflussgrößen, Modellbildung und Optimierung.* Dissertation, Leibniz Universität Hannover, 2006

74/2008 **Ziefle, G.** *Modeling aspects of coupled hydraulic–mechanical processes in clay material.* Dissertation, Leibniz Universität Hannover, 2008

75/2008 **Schimmels, S.** *Numerical Simulation of the Influence of Circular Cylinders on Mixing and Entrainment in Natural Density Currents.* Dissertation, Leibniz Universität Hannover, 2007